Laser-Induced Breakdown Spectroscopy in the Vacuum-Ultraviolet Wavelength Regime for the Application in Planetary Exploration

DISSERTATION

zur Erlangung des akademischen Grades
doctor rerum naturalium (Dr. rer. nat.)
im Fach Physik (Spezialisierung Experimentalphysik)

eingereicht an der
Mathematisch-Naturwissenschaftlichen Fakultät
der Humboldt-Universität zu Berlin
von

Simon Kubitza, M.Sc.

Präsidentin der Humboldt-Universität zu Berlin:
Prof. Dr.-Ing. Dr. Sabine Kunst

Dekan der Mathematisch-Naturwissenschaftlichen Fakultät:
Prof. Dr. Elmar Kulke

Gutachter:
1. Prof. Dr. habil. Heinz-Wilhelm Hübers
2. HDR Dr. Jeremie Lasue
3. Prof. Dr. Norbert Esser

Tag der mündlichen Prüfung: 12. Februar 2021

Kurzfassung

Diese Dissertation handelt von der Anwendbarkeit laserinduzierter Plasmaspektroskopie (englisch: laser-induced breakdown spectroscopy, LIBS) mit Detektion im vakuumultravioletten Spektralbereich (VUV), im Folgenden VUV-LIBS genannt, im Bereich der Planetenforschung. Für LIBS wird ein gepulster Laser auf die zu untersuchende Probe fokussiert. Aufgrund der hohen Spitzenleistungsdichten wird dabei Probenmaterial abgetragen, verdampft und teilweise ionisiert. Die im Plasma enthaltenen Atome und Ionen werden elektronisch angeregt und strahlen in der Folge Licht charakteristischer Wellenlängen ab, welches spektroskopisch analysiert werden kann. Diese Analyse erlaubt einen Rückschluss auf die im Plasma und damit auch in der Probe enthaltenen chemischen Elemente. Mit LIBS können im Prinzip alle Elemente detektiert werden. Allerdings sind insbesondere die Nichtmetalle schwerer zu detektieren, deren intensivste Emissionslinien im VUV-Bereich liegen, d.h. bei Wellenlängen kürzer als 200 nm, der oft nicht untersucht wird. Messungen in diesem Spektralbereich sind herausfordernd, da ein Großteil der Strahlung von der irdischen Atmosphäre absorbiert wird. Auf atmosphärelosen Himmelskörpern wie dem Mond besteht diese Schwierigkeit nicht, sodass für die Elemente C, Cl, H, N, O, P und S eine verbesserte Detektierbarkeit erwartet wird als mit konventionellem LIBS im typischerweise untersuchten Spektralbereich über 200 nm.

Inspiriert durch die ambitionierten Vorhaben der nationalen und internationalen Raumfahrtagenturen in naher Zukunft zum Mond zurückzukehren und dort nach Möglichkeit eine dauerhafte Mondbasis zu errichten habe ich das Potenzial von VUV-LIBS in der Anwendung auf dem Mond untersucht. Für dieses Projekt wurde am Institut für Optische Sensorsysteme am Deutschen Zentrum für Luft- und Raumfahrt in Berlin-Adlershof ein VUV-LIBS-Messplatz entworfen und aufgebaut. Nach einer Charakterisierung des neuen Laboraufbaus wurden zunächst durch Messungen an Proben, die nur wenige Elemente enthalten, Spektrallinien identifiziert, die mit dem Messaufbau typischerweise detektierbar sind. Dabei wurden Emissionslinien der Elemente Al, C, Ca, Cl, Cu, Fe, H, K, Mn, Na, Ni, O, P, S, Si, Ti und Zn im Bereich von 120 bis 195 nm identifiziert. Von Mg konnte in diesen Messungen keine Emission nachgewiesen werden. Darüber hinaus wurden mithilfe von Mondsimulant Studien zur quantitativen Analyse von S und Cl in Mondregolith durchgeführt. Dabei ergaben sich Nachweisgrenzen im Bereich von 0.5–1.0 at.-% für S und um 1.0 at.-% für Cl. Die auf dem Mond erwarteten Höchstkonzentrationen liegen dagegen im Bereich von 0.2 at.-% für S und 0.02 at.-% für Cl und können entsprechend bislang nicht detektiert werden. Der Zusammenhang zwischen LIBS-Signal und elementarer S- bzw. Cl-Konzentration war annähernd linear. Während der Messungen wurden starke Schwankungen der Signalintensitäten festgestellt, die einer mittels Ramanspektroskopie nachgewiesenen eingeschränkten Probenhomogenität zugeschrieben wurden.

Die in dieser Arbeit präsentierten Ergebnisse deuten darauf hin, dass VUV-LIBS in der Tat eine verbesserte Detektierbarkeit für S und Cl im Kontext einer Mondmission bewirken kann. Um das Potenzial der Methode für diese Anwendung umfassend beurteilen zu können und die Nachweisgrenzen zu senken, sind jedoch noch weitere Untersuchungen mit einem verbesserten Messaufbau notwendig. Es sei zudem darauf hingewiesen, dass VUV-LIBS, obwohl die am häufigsten in geologischen Proben anzutreffenden Elemente Al, Si und O zuverlässig nachgewiesen werden konnten, seinen größten Nutzen in Verbindung mit LIBS in anderen Spektralbereichen oder auch in Verbindung mit anderen analytischen Methoden finden mag, da wichtige gesteinsbildende Elemente wie Ca, Na und Mg im VUV-Bereich keine oder nur schwache Emission zeigen.

Abstract

This thesis investigates the application of laser-induced breakdown spectroscopy (LIBS) with detection in the vacuum ultraviolet (VUV) spectral range for in-situ space exploration. LIBS is a type of optical emission spectroscopy (OES). For LIBS, a pulsed laser is tightly focused onto the sample, thereby ablating material and exciting a luminous plasma. The atoms and ions contained in the plasma radiate light of characteristic wavelengths, which can be analysed with spectrometers like in other types of OES. The spectral analysis allows to identify the chemical elements in the plasma, which are assumed to be representative for the elements in the sample. With LIBS, in principle all elements can be detected. However, especially the non-metal elements are challenging to detect because their strongest lines are located in the VUV spectral range, i.e. below 200 nm, which is often not investigated. Detection in this range brings its own challenges, since large parts of the radiation spectrum are absorbed by the atmosphere surrounding the sample. On celestial bodies without an atmosphere, such as the Moon, the ambient conditions are well suited for VUV-LIBS analyses. In such a scenario, a better detectability for the otherwise challenging elements C, Cl, H, N, O, P and S is expected compared to LIBS in the usually employed detection range above 200 nm.

Motivated by the recent ambitions of the national space agencies to return to the Moon and to potentially set up a permanent moon base in the near future, I investigated the potential of VUV-LIBS in a lunar context. For this project, a dedicated set-up for VUV-LIBS was designed and built at Institut für Optische Sensorsysteme of Deutsches Zentrum für Luft- und Raumfahrt (DLR-OS) in Berlin-Adlershof. After an initial characterization including a relative spectral sensitivity estimate, chemically simple samples have been studied in order to identify emission lines that are typically detectable with this set-up. From these measurements, emission lines from Al, C, Ca, Cl, Cu, Fe, H, K, Mn, Na, Ni, O, P, S, Si, Ti and Zn could be identified in the spectral range from 120 to 195 nm. For Mg, no emission lines have been observed. Furthermore, two studies about the detection and quantification potential of the set-up for S and Cl in lunar analogue material have been conducted. I found detection limits in the order of 0.5–1.0 at% for S and of 1.0 at% for Cl, and an in general linear increase of the detected signal intensity with the analyte concentration for most of the investigated sample series. The expected maximum concentrations in lunar material of 0.2 at% for S and 0.02 at% for Cl can thus not yet be detected. Strong signal fluctuations observed in these studies have been attributed to a limited homogeneity of the samples, which has been deduced from Raman spectroscopy measurements.

The results shown in this thesis indicate that VUV-LIBS is promising for the improved detection of light elements such as S and Cl in a lunar context. However, more extensive studies with an optimized set-up are necessary to properly assess the true capabilities of the method and to further reduce the detection limits. Although emission from the most abundant chemical elements in geological samples, Al, Si and O, could be reliably detected in all samples containing them, the potential of VUV-LIBS might in the end be best used in combination with LIBS in the UV-VIS range or with other analytical techniques, because the major rock forming elements Ca, Na and Mg hardly show emission lines in the VUV spectral range.

Contents

List of Abbreviations

APXS	Alpha particle x-ray spectrometer
arb.u	Arbitrary units
at%	Per cent by atomic fraction
CCD	Charge coupled device
CMOS	Complementary metal-oxide semiconductor
cw	Continuous wave
DLR	Deutsches Zentrum für Luft- und Raumfahrt
DLR-OS	DLR-Institut für Optische Sensorsysteme
DN	Digital numbers
FWHM	Full width at half maximum
I, II, ...	With chemical element symbol, I=neutral, II=singly ionized, ...
ICP-OES	Inductively-coupled plasma optical emission spectroscopy
ISRU	In-situ resource utilization
IUPAC	International Union of Pure and Applied Chemistry
LHS-1	Lunar Highland simulant
LIBS	Laser-induced breakdown spectroscopy
LMS-1	Lunar Mare simulant
LOD	Limit of detection
LTE	Local thermodynamic equilibrium
NA	Numerical aperture
NASA	National Aeronautics and Space Administration (USA)
Nd:YAG	Neodymium-doped yttrium aluminium garnet
NIR	Near-infrared
NIST	National Institute of Standards and Technology (USA)
OAP	Off-axis parabolic mirror
OES	Optical emission spectroscopy
O I norm.	Internal standard normalization with O I
RMSEC	Root mean square error of calibration
SHG	Second harmonic generation
SNR	Signal-to-noise ratio
SOHO	Solar and Heliospheric Observatory
tot. int. norm.	Total intensity normalization
UV	Ultraviolet
VIS	Visible
VUV	Vacuum ultraviolet
wt%	Per cent by weight

List of Symbols

A_{ul}	Einstein coefficient for spontaneous emission
$B_{m,n}$	Einstein coefficient for absorption
c	Concentration
c_L	Speed of light in vacuum
E_{ion}	Ionization energy
$E_{ion,I}$	First ionization energy
$E_{ion,II}$	Second ionization energy
E_l	Energy of lower level
E_u	Energy of upper level
f	Focal length
g	Grating constant
g_l	Degeneracy of lower level
g_u	Degeneracy of upper level
G	Gain
h	Planck constant
k_B	Boltzmann constant
k	Confidence level multiplier in $k\sigma$
n_A	Particle area density
n_e	Electron density
m	Slope of the calibration curve
m_e	Electron mass
R^2	Coefficient of determination
T_e	Electron temperature
T_{init}	Initial electron temperature
α	Grating angle
γ	Lorentzian half-width
ΔE	Difference between energy levels
λ	Wavelength
ν	Frequency
σ	Standard deviation, both in statistics and as Gaussian line width

Chapter 1

Introduction

Since antiquity, humans have been observing the night sky and trying to understand the cosmic context in which their homeworld is situated. In the very beginning, the Earth was believed to be the centre of everything and the celestial bodies were assigned to gods of the mythology of the respective culture and time. However, already about 2300 years ago, Aristarchus of Samos postulated a heliocentric model of the universe and determined the Earth-Moon distance to within 7 % difference to the correct value [1] from observations with his bare eyes. Further observations by various astronomers and thorough logging of star positions over years and decades increased the understanding of the celestial mechanics.

With the invention of the telescope in the 17^{th} century and its subsequent optimization, the nature of extra-terrestrial objects could be investigated. Galileo Galilei discovered dark spots on the solar surface as well as the Jovian moons Io, Europa, Ganymede and Callisto, four objects neither orbiting the Earth nor the Sun. Furthermore, the surface of the Moon was studied, first maps of the lunar surface were drawn and the observed oceans (maria) and craters were named. Around the end of the 17^{th} century, Christian Huygens correctly noted the absence of water on the lunar surface, based on the lack of clouds and rivers. By observing stars disappear behind the lunar disk without prior attenuation of their light, he further deduced that the Moon does not have a significant atmosphere.

While ground-based observations led to further great discoveries, such as the Hubble-Lemaître law of the expansion of the universe in the 1920's, the next big technological advancement in astronomy was only about sixty years ago, when the first spacecrafts were launched and provided detailed photographs of the lunar surface and later geological samples from the Moon. To date, all planets in the Solar System as well as multiple asteroids and comets have been visited by a spacecraft at least in a flyby and provided valuable imagery of the bodies' surfaces. In addition, various landers and rovers on the Moon, Venus, Mars, Saturn's moon Titan and on different comets and asteroids took close-up photographs, performed in-situ chemical analyses of the local geology, measured the seismic activity or collected other data of interest for planetology with the aim to understand the formation and development of the Earth, its neighbours and the whole Solar System.

For the upcoming decades, ambitious plans of national and international space agencies and industrial companies foresee the creation of a Moon Village [2, 3] and the exploration of Mars with astronauts [4]. A logical step for the endeavour of building astronaut and research facilities on another celestial body is to use as much of the locally available resources as possible with a reasonable effort. This is called in-situ resource utilization (ISRU) and includes many concepts, most of which focus on the synthesis of some kind of spacecraft propellant and on the production of supplies such as drinking water, but also on the use of the local soil and rocks for construction, which has been tested in terrestrial laboratories. As is the case in industrial applications of natural raw materials on Earth, these processes require knowledge of the composition and condition of the source material harvested from the respective site. Concerning the second aim of sending humans to another world like Mars, with travel times of at least several months, one

will also want to characterize the environment beforehand in order to make sure that the risk of toxic material found at the landing site is negligibly low. Accordingly, a comprehensive analysis of the planetary surfaces is desired.

Early geochemical in-situ analyses by robotic probes on extra-terrestrial surfaces were conducted with alpha particle scattering and x-ray fluorescence spectroscopy [5]. Both methods are often combined in alpha particle x-ray spectrometers (APXS), which are still widely used as mission payload on planetary landers and rovers. APXS is based on the irradiation of the sample, in this case the planetary surface below the spacecraft, with alpha particles and x-ray photons from radioactive radiation sources. The alpha particles impinging on the surface are backscattered from the sample atoms after transferring a fraction of their kinetic energy. Measuring the energy of the backscattered alpha particles allows to deduce the mass of the sample atoms and thereby the involved chemical elements. At the same time, the sample atoms are electronically excited by the highly energetic x-ray photons and emit element-characteristic luminescence during the subsequent relaxation. In combination, these two techniques can identify and quantify many chemical elements over a wide range of concentrations. Due to its low power consumption and a lightweight architecture, multiple variations of APXS instruments have been employed on different space missions. One major drawback of APXS is, however, that the instrument needs to be placed close to the sample and that measurements typically take several hours, although a coarse chemical survey of the major and minor but not the trace elements may be achieved within tens of minutes with the newest instruments. In addition, APXS results represent the bulk composition of the sample due to a relatively large footprint in the order of several centimetres. This reduces the method's suitability for mineral identification.

An alternative method for the in-situ elemental analysis of planetary surfaces with much shorter sampling times of only seconds to minutes is Laser-Induced Breakdown Spectroscopy (LIBS), e.g. [6] or [7]. In LIBS, a pulsed laser is tightly focused onto the sample to achieve power densities in the order of several $\mathrm{GW/cm^2}$ on the nanosecond timescale. This causes the rapid ablation of sample material and the excitation of the same into a small luminous plasma. The plasma contains neutral atoms, ions, electrons, simple molecules and sometimes also small fragments of the sample material. Due to the very high deposition of energy in the small sample volume of less than $1\,\mathrm{mm^3}$, most of the plasma species are electronically excited. Hence, they radiate characteristic line emission upon relaxation to the ground state, which can be analysed and attributed to the chemical elements in the plasma and therefore in the sample. Furthermore, the intensities of the emission lines are related to the elemental abundances.

LIBS has the key advantage of only needing optical access to the sample, little to no required sample preparation and the aforementioned short sampling times, while it can in principle detect all chemical elements. Moreover, the plasma shock wave can remove dust layers, and the successive removal of sample material allows to obtain depth profiles at a scale of about $5\,\mu\mathrm{m}$ per laser pulse, depending on the sample hardness [8]. For these reasons, LIBS has received an increasing interest in the planetary science community in the last two decades.

The ChemCam (Chemistry and Camera) instrument aboard the Mars Science Laboratory, a robotic vehicle of the US-American National Aeronautics and Space Administration (NASA), is the first LIBS instrument that conducted measurements on a planetary body other than Earth [9, 10]. It started operation in 2012 and is since then collecting data on an almost daily basis. LIBS has also been investigated as a possible payload for missions to planetary bodies other than Mars, such as the Moon [11], Venus [12], the Jovian moon Europa [13], the Martian moon Phobos [14], or asteroids [15]. In 2019, the rover Pragyan, which was carrying a LIBS instrument, was sent to the Moon in the context of India's mission Chandrayaan-2, but unfortunately the descent stage did not accomplish a safe landing. In 2020, two more LIBS instruments started their journey to Mars, planning to arrive at the beginning of 2021: The Chinese Tianwen-1 mission carries a rover with the LIBS instrument MarsCoDe aboard [16], and NASA sends a new rover with the SuperCam instrument [17] as an extended follow-up for ChemCam.

While measurements with LIBS are very straightforward, the analysis of the obtained spectra

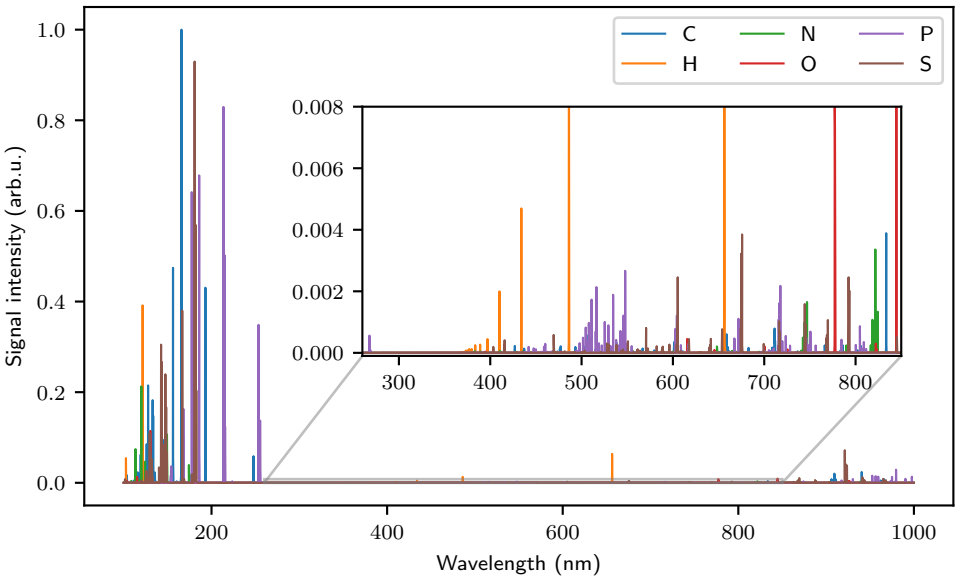

Figure 1.1: Simulated LIBS spectra of the biology related elements C, H, N, O, P, S. The most intense emission lines of these elements are located below 200 nm. The simulation is based on a uniform plasma in local thermodynamic equilibrium with a linearly decreasing temperature starting at 12 000 K and an electron density of 5×10^{22} /m^3. Details about the simulation are provided in section 2.1.3.

can be challenging due to the complexity of the investigated plasma plume and its sensitivity to influences from external factors [18]. Such external factors include, for instance, the absorption coefficient of the sample material for the laser wavelength, the sample hardness and the laser power density and pulse duration. These and further influences, all summarized with the term matrix effects, complicate a quantitative analysis and lead to the necessity of an extensive calibration for the respective study case. In the context of space exploration, one of the most important factors of influence is the surrounding atmosphere that controls the evolution of the plasma plume [19]. On Earth, the LIBS plasma is confined by the terrestrial atmosphere, resulting in a small but bright plasma. Due to the high density of plasma species, large parts of the emitted light can be re-absorbed before escaping the plasma plume, which causes a saturation of the emission line amplitudes for high analyte concentrations as well as a broadening of the lines. The spectra recorded with the ChemCam instrument on Mars benefit from the reduced ambient pressure in the range of 0.7–1.0 kPa [20], which is almost ideal for LIBS [11]. The lower confinement leads to a large and luminous plasma with a significantly lower degree of self-absorption compared to Earth. In vacuum, more precisely for pressures below approximately 1 Pa, confinement due to the thin residual atmosphere becomes negligible and the ablated material freely escapes from the sampling region [21]. The resulting plasma plume is characterized by a low emissivity and a short life time of only a few hundreds of nanoseconds, as compared to the ten-microsecond timescale for Earth and Mars, and therefore by a low signal intensity for analysis.

Furthermore, although LIBS can in principle detect all elements, some of them, especially from the non-metals in the groups 14 to 17 of the periodic table, are challenging to detect, because they have only electronic transitions of low probability in the UV to NIR spectral range, which is commonly observed in LIBS analyses [22]. In combination with experiments in vacuum conditions, the detection of these elements is even more challenging.

Figure 1.1 shows simulated LIBS spectra of the elements C, H, N, O, P and S, which are typical markers for habitability as well as for biological material and therefore of particular interest, e.g. for space missions in the context of the search for extra-terrestrial life. The inset shows the spectral range from 260–850 nm, which is often used for LIBS studies. In this range, many emission lines from the selected elements are evident. However, when extending the spectral range, one can see that the most intense emission lines of these six elements are located

at wavelengths below 200 nm, and that their intensities are two to three orders of magnitude higher than those of the UV-VIS-NIR emission lines.

The range from 100–200 nm is the so-called vacuum ultraviolet (VUV) range. As the name suggests, observations in this spectral range require vacuum because the radiation would otherwise be absorbed by O_2 and H_2O from the atmosphere. In laboratories, purge atmospheres of Ar, He or N_2 that are transparent in the VUV can also grant access to this wavelength range. The additional experimental effort of establishing a VUV-transparent atmosphere in combination with special VUV-compatible optics is a potential reason, why VUV-LIBS is not yet widely applied. Most of the studies concerning VUV-LIBS are related to applications in the steel industry, specifically focusing on the detection of C, S and P [23, 24], but also Cl detection in cement [25] and S detection in coal [26] have been reported. Only one article by Radziemski et al. [27] reports on the use of VUV-LIBS for a potential application in planetary exploration, specifically on Mars. In simulated Martian atmospheric conditions, they find strong signals of C, P and S, but also observe significant absorption for wavelengths below 160 nm due to the CO_2 atmosphere.

The requirement of vacuum makes VUV-LIBS particularly interesting for the Moon or various asteroids due to the absence of an atmosphere. As mentioned before, the plasma is characterized by a short life time and a low emissivity in vacuum conditions, thus leading to an already challenging situation for LIBS. Using the strong VUV emission lines could be greatly beneficial to in-situ LIBS analyses on the Moon and other bodies without an atmosphere, since the conditions on these planetary bodies are already well-suited for VUV-LIBS and there is a great potential for improving the detection capability of LIBS by accessing this spectral range. This is especially relevant for the elements that are otherwise challenging to detect.

This thesis focuses on the application of VUV-LIBS on celestial bodies without atmosphere, using the example of the Moon. In order to evaluate the detection capabilities of VUV-LIBS in the context of a mission to the Moon, a new laboratory set-up with experimental parameters such as the laser pulse energy and the sampling distance realistic for an in-situ space instrument is designed, built and characterized. The resulting set-up is then tested on different samples and first studies are conducted.

Chapter 2 will give an introduction to LIBS and to the theoretical background of the emission spectra. It further elaborates on the experimental challenges inherent in the VUV spectral range. In chapter 3, I will explain the sample preparation process and present an approach to characterize the samples.

In chapter 4, the established VUV-LIBS set-up is described and characterized. I will further present an approach to determine the spectral sensitivity of the set-up by comparison of simulated and measured line strengths, and identify the relevant spectral broadening mechanisms. Finally, the measurement routine and data processing procedure will be explained.

Due to the very different experimental parameters compared to most publications reporting on VUV-LIBS studies, a catalogue of emission lines identified with the present set-up is compiled in chapter 5. Different dependencies of the emission intensity on the laser pulse energy for neutral to triply ionized Si are investigated as well. The chapter ends with a list of identified emission lines with a subjectively assigned relative strength to assist future line identification problems and to reveal interference-free emission lines.

First scientific studies investigating the detection and quantification capability for S and Cl in lunar analogue material with the new VUV-LIBS set-up are presented in the chapters 6 and 7, respectively. These two have been selected because they are among the elements that are challenging to detect with conventional LIBS and for which the detection in the VUV spectral range is expected to be particularly promising. Both elements are relevant for planetary science, as their detection and quantification would allow to constrain the magmatic processes that occurred in the geological history of the Moon [28]. In addition, several ISRU-based applications have been identified for lunar S [29], which rely on the assessment of the local S abundance.

Chapter 2

Theory

This chapter gives an overview of the theoretical background relevant to this thesis. In the first section, I will present the fundamental processes involved in laser-induced breakdown spectroscopy (LIBS), which are the ablation of material and the evolution of the plasma, with a focus on LIBS plasmas induced in very-low-pressure atmospheres. Furthermore, I will describe the optical emission of laser-induced plasmas and present an approach to simulate this emission. The next section will provide the analytical procedures employed for quantitative analyses with LIBS, including common figures of merit, normalization methods and different definitions for the limit of detection (LOD). In the third section, I will give an overview of the vacuum ultraviolet (VUV) spectral range and summarize the experimental challenges inherent in VUV spectroscopy. Finally, I will briefly introduce Raman spectroscopy, which is used to characterize the spatial homogeneity of the samples.

2.1 Laser-induced breakdown spectroscopy

Laser-induced breakdown spectroscopy (LIBS) is a type of optical emission spectroscopy (OES). OES has been applied systematically for the first time by Kirchhoff and Bunsen [30] in the 1860's using flame spectroscopy. They found the relationship between elements and spectral lines and thereby discovered several formerly unknown elements. Since then, the technique was further developed and different variants of OES arose.

From the 1960's, the newly developed lasers were already used as ablation sources for subsequent spark discharge spectroscopy. The radiation emitted by the ablated material was, however, not analysed because the quality of the results could not compete with conventional spark discharge spectroscopy already established at this time [31, 32]. However, in the following decades it was discovered that the spectroscopy of laser-induced sparks has unique advantages in comparison to conventional spark discharge spectroscopy, thanks to its reliance on purely optical excitation and detection. One advantage is that the method does not require sample preparation in the same way as many other spectroscopic techniques do, including spark discharge spectroscopy. Another advantage is that it only requires optical access to the sample, which allows for stand-off analysis at several metres distance [33] as well as for analysis of otherwise inaccessible surfaces. Since LIBS measurements are also very quick and can be done within milliseconds, LIBS has been found to be a very interesting technique for various specific in-situ applications, e.g. in the fields archaeology [34], the steel industry [35] and space exploration [9, 10].

For LIBS, a pulsed laser is tightly focused onto the sample. When a sample-dependent threshold irradiance in the order of $1\,\mathrm{GW/cm^2}$ is exceeded, sample material is rapidly vaporized and excited into a plasma close to the sample surface [36]. The plasma consists of mainly electrons, ions and neutral atoms, but larger fragments ejected from the sample are also present. Furthermore, simple molecules can form in the plasma. The plasma species radiate continuum and line emission, from which the latter can be used for analysis. It is common in the LIBS community to use Roman numerals to specify the ionization state of the emitting species. For

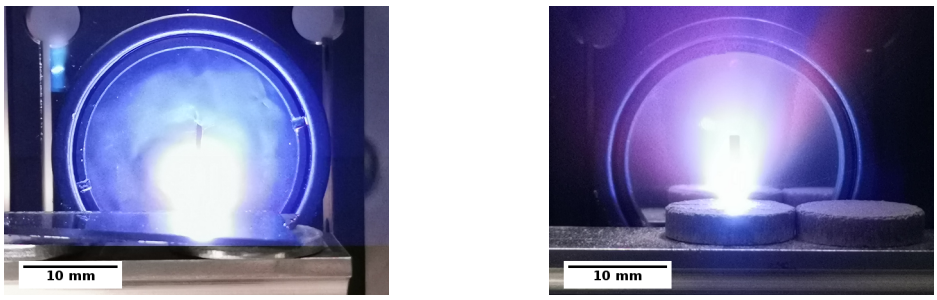

Figure 2.1: Photographs of a plasma excited at different ambient pressures of 1 kPa (*left*) and 1 mPa (*right*). The sample in these recordings was not the same, leading to the different colouring visible in the pictures. The left picture shows a plasma of a silicon wafer, while the right plasma is created from a lunar simulant pellet with intermixed NaCl. In general, the appearance of the two plasmas shown here is, however, representative for the different pressure regimes.

the example of aluminium, Al I means neutral species, Al II singly ionized, Al III doubly ionized, and so forth. The following three subsections will provide the relevant information about the ablation process and plasma evolution, the optical emission of the plasma, and the computational approach to simulate the plasma emission. More detailed information about these topics can be found in LIBS textbooks, e.g. Singh and Thakur [6], Cremers and Radziemski [7].

2.1.1 Laser ablation and plasma evolution

The physical processes involved in the ablation process strongly depend on the laser pulse energy and duration. For nanosecond pulses, such as emitted by the Nd:YAG laser used for this project, and irradiances close to the LIBS threshold, thermal processes dominate the ablation [37]: The incident light is absorbed by free electrons in the sample material, mainly due to inverse bremsstrahlung, which thereby gain energy. In the case of non-conducting samples, the very first photons generate free electrons in a multi-photon absorption process, which can then free further electrons from the lattice. Collisions of the energetic electrons with the lattice atoms heat the material. If energy is faster supplied by the laser through electrons than it dissipates due to thermal conductivity, the sample material will melt and eventually evaporate. The vapour is further heated to ionization by the still incoming light, hence forming a plasma. For higher irradiances, non-thermal processes such as phase explosion occur, in which the surface is vaporized within a very short time [38]. When the plasma reaches a critical density, it becomes opaque for the incident laser radiation and the last part of the laser pulse is absorbed by the plasma before reaching the sample surface, thus heating the already existing plasma [39]. This phenomenon, commonly referred to as plasma shielding, inhibits the further ablation of sample material and therefore limits the number of potentially emitting plasma species [40]. When reducing the ambient pressure towards approx. 1 Pa, the lower confinement of the excited plasma to the sample surface reduces the density of the plasma and therefore allows a longer part of the laser pulse to participate in the ablation process. This results in more emitting species and thus in a brighter plasma plume. A further reduction below 1 Pa was found to have a negligible influence on the ablation process and plasma evolution [21].

The ablated sample material is dense and will therefore expand into the surrounding. The details of this expansion depend very much on the ambient atmospheric conditions, but also on the initial plasma parameters. With surrounding atmosphere, such as air or a purge gas, the plasma plume has to expand against the atmosphere and expansion is therefore slowed down. The plasma is confined to a smaller volume and frequent collisions between the plasma species, mainly between electrons and atoms or ions, repeatedly cause electronic excitation of the species. This collisional re-excitation can increase the life time of the plasma to several tens of microseconds [41]. In vacuum, on the contrary, the plasma freely expands into the ambient without confinement. This can already be seen from the shape of the plasma plume in the photographs presented in Figure 2.1: For an ambient pressure in the order of 1 kPa (left), the

plume is almost spherical, while it appears elongated with a cone-like shape for pressures in the order of 1 mPa (right). The lack of confinement and therefore of significant collisions between the plasma species results in a shorter life time in the order of only hundreds of nanoseconds [42].

2.1.2 Optical emission of laser-induced plasmas

The plasma, consisting of atoms, ions and free electrons, radiates a continuum as well as characteristic line emission of the contained elements. The continuum is mainly due to bremsstrahlung emitted by the electrons upon collision with neutral atoms and ions as well as due to electron-ion recombination [7]. It does not contain information about the plasma species and is therefore not of analytical use.

Line emission, on the contrary, is emitted by the atoms, ions and sometimes even simple molecules that form in the plasma [43]. If these are electronically excited, they will relax to the ground state after a characteristic life time of the excited state and emit a photon of the corresponding energy level difference.

Precise prediction of the emission characteristics of the plasma from the experimental parameters and the inverse problem of exact deduction of, for example, the elemental abundances from a recorded spectrum require to 1) understand all involved processes and 2) simulate the plasma dynamics under consideration of these processes. Various aspects of the complex evolution of the plasma have been modelled by different groups [44–46], but this is related to a considerable computational effort. Therefore, in most cases a simplified model is used, making a few assumptions:

1. Stoichiometric ablation
   A key requirement for quantitative analysis is that the elemental composition of the plasma plume reflects that of the sample. Especially for long laser pulses in the microsecond regime and low power densities, the thermal properties of the sample material determine the ablation process and selective vaporization may occur [47]. For nanosecond pulses and power densities in the order of $1\,\mathrm{GW/cm^2}$, the plasma composition is expected to be close to the sample composition. The spatial distribution of the plasma species can, however, still be heterogeneous.

2. Local thermodynamic equilibrium (LTE)
   LTE means that the velocity (Maxwell-Boltzmann), excitation (Boltzmann) and ionization (Saha-Eggert) distribution can be described by their respective statistical equation, and, that their characteristic temperature is the same. For such an equilibrium to be established, the excitation and de-excitation processes in the plasma must be dominated by collisional processes rather than by radiative processes. Since collisional excitation is mainly due to collisions with electrons, McWhirter [48] formulated a criterion for the minimum electron density n_e that is required to establish an equilibrium for a system with a given maximum energy difference ΔE between neighbouring excited states:

   $$n_e > 1.6 \times 10^{18} \sqrt{T_e}\, \Delta E^3 \,. \tag{2.1}$$

   Here, the n_e is given in $\mathrm{m^{-3}}$, T_e is the electron temperature in K and ΔE is given in eV. As pointed out by Cristoforetti et al. [49], this criterion is, however, not sufficient to ensure the existence of LTE but merely tests if LTE *can* exist. Due to the transient and spatially inhomogeneous nature of the plasma, two more criteria must be fulfilled: Firstly, the relaxation time τ_{rel} needed to establish an equilibrium must be short compared to the timescale on which the electron temperature and density vary, and secondly, the diffusion length during the relaxation time must be smaller than the characteristic length of the spatial variation of the plasma parameters. Since the relaxation time increases with $\tau_{\mathrm{rel}} \sim \Delta E \exp(\Delta E / k_B T_e)$, where k_B is the Boltzmann constant, equilibrium conditions are more difficult to achieve for VUV transitions, which have a transition energy ΔE in the order of 10 eV. For the O I transition at 130 nm, for example, the relaxation time is in the order of $\tau_{\mathrm{rel}} \approx 100\,\mu\mathrm{s}$ [49]. In combination with the short life time of only hundreds of nanoseconds,

LTE conditions are likely not provided in vacuum LIBS plasmas. As a consequence, neither the ratio of ions to neutral atoms nor the population of the energy states of the ions and atoms may follow the distribution predicted by its thermodynamic statistics.

3. The plasma is optically thin
   Photons emitted during electronic transitions of the plasma species can be re-absorbed by another atom or ion of the same type and would then no longer be available for analysis. The phenomenon is called self-absorption and leads to a saturation of the emission line intensities for high analyte concentrations. The number of absorbed photons is higher if more photons of a particular energy are available. Thus, the central wavelengths of spectral line profiles are more affected by self-absorption than the wings, leading to an observed line broadening. Obviously, the main factor to consider for self-absorption is the number density of the emitting species. Therefore, the effect is generally decreased in vacuum, but can still be observed. Since absorption can only occur when the lower electronic state is occupied, it appears especially in colder regions of the plasma. In an optically thin plasma, self-absorption is negligible and the detected photon flux is a direct measure for the number of electronic transitions of the plasma species.

2.1.3 Simulation of LIBS emission spectra

For the sensitivity calibration of the instrument and the prediction of emission lines to assist line identification, a spectrum simulation tool developed by my colleague Peder Hansen will be used. An article describing the simulation process in more detail is in preparation [50].

The version of the program used in this thesis assumes a homogeneous and iso-thermal plasma with an electron density n_e and temperature T_e. The radiation intensity is calculated along a single line-of-sight of length z through the plasma with a particle number density n. As the following equations will show, neither z nor n itself is relevant but the product of these two. Therefore, the model takes the area density $n_A = n \cdot z$ for the integrated path as an input parameter. Furthermore, the chemical elements with their relative abundances need to be provided. Based on LTE, the distribution of the ionization states per chemical element is calculated with the Saha-Eggert-equation [51]

$$\frac{n_{i+1}}{n_i} = \frac{(2\pi m_e k_B T_e)^{3/2}}{n_e h^3} \frac{Z_{i+1}}{Z_i} \exp\left(-\frac{E_{\text{ion}} - \Delta E_{\text{ion}}}{k_B T_e}\right) . \tag{2.2}$$

Here, n_{i+1} and n_i are the number densities for the ionization states $i+1$ and i, m_e the electron mass, $Z_{\text{i+1}}$ and Z_i the partition functions for ionization states $i+1$ and i, E_{ion} the ionization energy, ΔE_{ion} a correction of the ionization energy for high density plasmas, and k_B and h the Boltzmann and Planck constant, respectively. Species up to five-fold ionization are considered in the simulation. Within the species of element and ionization state, the population of the energy levels is described by the Boltzmann-equation. For an excitation state $E_{i,m}$, the number density of species in this state is given by [51]

$$n_{i,m} = \frac{n_i \, g_{i,m}}{Z_i} \exp\left(-\frac{E_{i,m}}{k_B T_e}\right) , \tag{2.3}$$

with the degeneracy $g_{i,m}$ of the excitation state. After determining the number densities $n_{i,m}$ for elements in ionization state i and energy level m, the one-dimensional radiative transfer along the line-of-sight,

$$\frac{dI_\lambda}{dx} = \alpha_\lambda - \beta_\lambda \cdot I_\lambda , \tag{2.4}$$

where I_λ is the radiance at the wavelength λ, is evaluated. The model only considers spontaneous emission, stimulated emission and absorption, but no electron-ion recombination or

bremsstrahlung. The coefficients for spontaneous emission, α_λ, and for stimulated emission and absorption, β_λ, for a transition of wavelength λ are given by

$$\alpha_\lambda = A_{mn}\, n_{i,m}\, P_\lambda \, \frac{1}{4\pi c_L}\,, \tag{2.5}$$

$$\beta_\lambda = h\nu \, \frac{d\nu}{d\lambda} \cdot \left(B_{nm} n_{i,n} - B_{mn} n_{i,m}\right) P_\lambda \, \frac{1}{c_L}\,. \tag{2.6}$$

Here, A_{mn}, B_{mn} and B_{nm} denote the Einstein coefficients for spontaneous emission, stimulated emission and absorption, respectively, ν is the radiation frequency, and c_L the speed of light. P_λ describes a spectral line profile calculated from Doppler and Stark-broadening. α_λ and β_λ are calculated for various emission lines in the considered spectral range for which the relevant constants could be found in the NIST Atomic Spectra Database [52], and then summed for each wavelength. For some elements, additional data is taken from the Atomic spectral line database by Kurucz and Bell [53]. Finally, the solution to the radiative transfer equation and hence the radiance I_λ of the plasma at a given wavelength is

$$I_\lambda = \frac{\alpha_\lambda}{\beta_\lambda} \cdot \left[1 - \exp(-\beta_\lambda \cdot z)\right]. \tag{2.7}$$

Since β_λ is directly proportional to the particle number density n, which determines the density $n_{i,m}$ of particles in ionization state i and energy level m, n can be drawn out of β_λ and combined with z to form the area density $n_A = n \cdot z$ as an input parameter for the simulation. These simulations may provide inadequate results for temporally and spatially integrated spectra, as they will be recorded in this project. To partially account for the time-integrated detection scheme of the VUV set-up, multiple spectra are calculated for a set of linearly decreasing temperatures and then summed. The spatial integration could be reflected with multiple zones of different temperatures. However, since already the fundamental assumption of LTE does likely not hold true for vacuum LIBS plasmas, adding additional layers and thereby increasing the computation time was not considered beneficial. In summary, it should be kept in mind that while these simulations provide an estimate of emission line intensity ratios and can thereby assist line identification, discrepancies between the measured and the predicted spectra will likely occur.

2.2 LIBS analytical procedures

For a quantitative elemental analysis with LIBS, the instrument needs to be calibrated. Therefore, a set of calibration samples with well-known concentrations of the elements of interest is analysed. From the recorded spectra, the emission line intensities related to the particular elements are extracted and plotted as a function of the concentration. In the ideal case, which is usually applicable at low concentrations, the signal will increase approximately linearly with the elemental abundance [7]. Thus, a linear regression can be calculated, which allows to deduce unknown concentrations from measured signal intensities. For higher concentrations, a saturation due to self-absorption is often observed and the slope of the calibration data slowly decreases until it finally levels off. This saturation can be accounted for with non-linear calibration curves, if calibration standards for the concentration range are available. Naturally, deviations from the linear regression will occur over the whole range of concentrations. To evaluate the quality of an established calibration, different figures of merit can be calculated. The ones used in this project will be presented in section 2.2.1.

Besides self-absorption, various other factors due to the surrounding atmosphere but also due to properties inherent in the sample influence the emission intensity of the spectral lines. The influences related to the sample properties are summarized with the term *matrix effects* and can be subdivided into physical and chemical matrix effects. They include amongst other mechanisms differences in laser coupling, in ablation rates, in plasma plume electron densities and in electron temperature for different sample types, but also the interaction of the plasma

constituents such as quenching or the potential formation of simple molecules in the plasma for some species. Therefore, the set of calibration standards should be as similar as possible to the samples to be analysed, as should be the experimental conditions during the calibration and the intended application.

Fluctuations of the signal intensity between different spectra from the same sample may arise from statistical variations in the laser pulse energy and duration or from matrix effects, e.g. the differently sized grains in the field of view that affect the laser coupling. A common approach to reduce those fluctuations is normalization with some other information related to the measurement. Furthermore, normalization may in some cases release the necessity to calibrate the instrument on similar samples and can therefore enable a wider applicability of an established calibration [54]. More details about normalization and the methods tested in this study are given in section 2.2.2.

Finally, to judge the analytical capability of a given instrument in a prospected scenario, one will like to define a minimum concentration that can be reliably detected. This will depend on the signal intensity compared to the system noise as well as on the typical signal scatter of the method itself. Details about the LODs determined in this project are given in section 2.2.3.

2.2.1 Calibration figures of merit

For the low concentrations of analyte in the calibration samples used here, self-absorption has not been observed and is therefore not considered. Hence, the calibration curves will be linear regressions through the data of a particular sample series. Due to the spatial heterogeneity found for the samples, see section 3.3 for details, the calibration will be based on the mean intensity per sample.

As a first step, the coefficient of determination R^2 can be calculated for the linear regression. R^2 is a measure for quality of the regression in that it relates the explained variance in the data to the total variance. Although an R^2 close to unity does not necessarily mean that the data follows a linear trend, it still shows that a linear regression is a good approximation in the given range of concentrations.

A second measure that will be used is the root mean square error of calibration (RMSEC), i.e. the quadratically averaged deviation of the concentrations deduced from the calibration curves from the respective nominal concentrations. The RMSEC, sometimes also referred to as calibration error, thereby gives an estimate of how much a concentration deduced from the signal intensity of an unknown sample and the calibration curve may deviate from the unknown true concentration. For a robust estimate of the calibration error, one would randomly split the data in a calibration and a verification set, establish a calibration from the calibration set, and then calculate the RMSEC for the validation set. Repetitions with differently compiled calibration and verification sets allow to specify a typical value for the RMSEC. However, this requires a large enough data set that can be split in two, which is not the case here. For the data presented in chapters 6 and 7, the measured intensities from multiple locations per sample have been averaged to reduce the influence of variations in the local concentration. Furthermore, since the variation of the signal per sample, which is assumed to be mainly due to the mentioned sample heterogeneity, appeared to increase with the concentration, the deviations from the calibration curve have been scaled with the nominal concentrations, resulting in a relative RMSEC. The presented calibration errors are calculated as follows:

$$\mathrm{RMSEC} = \sqrt{\frac{1}{n}\sum_{i=1}^{n}\left(\frac{c_{p,i} - c_{r,i}}{c_{r,i}}\right)^2}, \tag{2.8}$$

where $c_{p,i}$ is the concentration predicted from the average signal of sample i, $c_{r,i}$ denotes the corresponding nominal bulk concentration and n is the number of samples.

2.2.2 Normalization

Normalization in LIBS means a scaling of the data on a per-spectrum basis with the aim to reduce intensity fluctuations due to varying experimental conditions and matrix effects. The scaling factor used therein is a quantity derived from the respective measurement. Throughout the LIBS community, many normalization methods are used. While most of them are related to the recorded spectrum itself, normalization with the plasma shock wave [55] or the ablated mass [56] has been reported as well.

In their recent review article on normalization methods across different fields of application for LIBS, ranging from terrestrial and extraterrestrial geology over liquid crystal display recycling to food analysis, Guezenoc et al. [57] conclude that the best applicable normalization is case-dependent, with non-normalized data sometimes even being preferred. Sometimes, the best approach might as well not only depend on the application but also on the element of interest [58, 59]. Finally, they recommend carefully evaluating the applied normalization by comparing different figures of merit like the R^2, calibration errors, or deduced limits of detection for normalized and non-normalized data.

Two of the most commonly used methods are normalization with the total intensity of the spectrum and normalization with an internal standard [57], which I will also apply to my data. For both of them, the intensities of certain spectral ranges are integrated in each spectrum and then the dark-corrected spectra are divided by these values. The limits of these spectral ranges are summarized in Table 2.1. More details about the two methods are given in the following.

Total intensity normalization For total intensity normalization, the sum of all spectral channels is used to scale the spectrum. Since this sum effectively represents the area between the base line and the spectrum, the method is also called total area normalization. This method compensates scaling effects that affect all spectral channels similarly, e.g. changes in the laser pulse properties that cause variations in the ablated mass. For narrow spectral ranges, the results of this generic approach can easily be distorted due to a bias by the few spectral lines in the range. If, for example, most emission lines in the spectral range are from ionized species while the line of interest is emitted by a neutral atom, changes in the plasma electron temperature might inversely affect the intensities of the total spectral range and of the line of interest. Furthermore, contaminating elements that express strong emission lines in the analysed spectral range already at trace concentrations can significantly contribute to the total intensity. An example for this would be the Na I line at 589 nm for spectra in the visible range [60].

In this study, the spectral range 128.0–190.0 nm is used for total intensity normalization, which is dominated by an O I triplet as well as multiple Al II and III lines.

Internal standard normalization is adopted from other methods, such as inductively-coupled plasma optical emission spectroscopy (ICP-OES). Traditionally, the internal standard was a manually added element that could later be detected and used as a reference. With respect to LIBS, the reference element is often naturally contained in the sample at a well-known concentration, or at least the concentration is expected to be constant throughout a set of samples. For normalization, a suitable emission line of the reference element is selected and its emission intensity in the respective spectrum is used to scale the data. Like the total intensity normalization, this accounts as well for changes in the ablated mass or the excitation state of the plasma but with a better-defined reference.

Method	**Spectral range (nm)**
Total intensity norm.	128.0–190.0
O I norm.	130.0–130.7
Si II norm.	2× Lorentzian fit at 126.0

Table 2.1: Evaluated spectral ranges for different normalization methods used in this study.

The internal standard method may be especially helpful if the sample cannot be further characterized in other ways, as, for example, in the case of space exploration. For LIBS data from Mars, normalization with carbon emission from the ubiquitous CO_2-dominated atmosphere or oxygen signal from both the sample and the atmosphere could be applied. This has been successfully done by Rapin et al. [61], while Schröder et al. [62] reported a limited suitability of C I and O I normalization.

Among the several requirements to an internal standard emission line identified by Barnett et al. [63], two of the most important ones are that the ionization energies of the elements and the population densities of the involved upper states and therefore the upper energy levels of the transitions should be comparable. However, Myers and Tracy [64] found for ICP-OES measurements that even if not all of the requirements stated by Barnett et al. [63] are met, internal standard normalization might still be applicable and beneficial.

For the sulfur-related studies in chapter 6 and the chlorine-related study in chapter 7, the O I triplet at 130 nm is used as the internal standard. Its intensity is assessed by summing over the spectral range 130.0–130.7 nm. This emission line triplet has been selected as the internal standard because it is the only neutral emission line of significant intensity in the observed spectral range, except for the analyte emission lines. Furthermore, the oxygen concentration is with 58–61 at% almost equal for all investigated samples. In chapter 7, normalization with the Si II doublet at 126 nm is tested as well, because the signal variations observed for Cl I emission (133–137 nm) appeared to be related to the spectral region of the emission lines rather than to the LIBS process itself. The line intensity of the Si II doublet is derived by fitting a model of two Lorentzian profiles and a linear background to the data.

2.2.3 Limit of detection

Different definitions for the LOD exist and are used by the LIBS community, resulting in a lack of comparability. Inspired by Lasue et al. [11], I will derive the LOD in three ways according to the following definitions.

LOD_1 The lowest concentration that has been reliably detected can serve as a first estimate for the LOD_1. For reliable detection, the signal at the spectral position of the analyte emission line should be well above the noise of a blank sample not containing the analyte. This *well above* commonly translates into higher than the mean plus three times the standard deviation of the blank sample signal. Thus, the signal-to-noise ratio (SNR) for the respective emission line should be larger than three. In the case of broadened lines, the sum over a small spectral range may be used instead of a single detector channel. While this confirms the reliable detection in a single measurement, confidence for the detection of a certain low concentration is only given when the majority of repeated measurements yields a signal higher than the threshold. For a confidence of, e.g., 90 %, nine out of ten spectra should yield a positive result. Depending on the available samples, LOD_1 may be similar, higher, or even lower than the other LODs defined in the next paragraphs. For a good estimate of LOD_1, samples above and below the actual detection limit should be analysed.

LOD_2 The second method is the one recommended by the International Union of Pure and Applied Chemistry [65]. Here, LOD_2 is defined as the concentration corresponding to the mean signal level plus k times the standard deviation σ of the blank sample. The factor k specifies the confidence level. I will use $k = 3$, which corresponds to a confidence of 90 % for normally distributed uncertainties [66, 67]. With the slope m of the calibration curve relating the measured signal intensity I to the concentration c, LOD_2 amounts to $LOD_2 = k\sigma/m$. When no blank samples are available or have been studied, the lowest concentration samples are often used as a replacement and the average of their standard deviations is used for σ [11, 27]. Accordingly, I will use the average of the lowest three concentrations' standard deviations to determine LOD_2.

LOD_3 This method suggested by Currie [67] aims to avoid both false positives and false negatives when testing for the presence of an element. It is described in detail by Massart et al. [68]. LOD_3 is based only on the linear regression and the variance deduced from the data. A key difference compared to the previous method is that it considers both uncertainties in the regression parameters of the established calibration, and sampling statistics for the measurements on the unknown sample. As a consequence, LOD_3 depends on the intended measurement protocol, meaning the number of measurements that will be conducted and averaged before applying the calibration to deduce an unknown concentration. I will in most cases assume the same number of spectra per sample as have been acquired for the calibration. Due to the many considered uncertainties that are otherwise often neglected, the resulting LOD_3 may in general be more conservative.

2.3 The vacuum ultraviolet range

Figure 2.2: Early version of a VUV spectrograph by Viktor Schumann, 1892. Image reprinted with permission ©Deutsches Museum, München, ID: 67787-21030220_010_SAMOA_ND_HD.

The VUV spectral range is the continuation of the deep-UV towards shorter wavelengths and is itself continued by x-ray radiation towards even higher photon energies. First observations in this spectral range were accomplished by Viktor Schumann in the late 19^{th} century, using the evacuated spectrometer based on a flint glass prism and shown in Figure 2.2. Later, in 1906, Theodore Lyman discovered the K_α transition ($n = 2 \rightarrow n = 1$) of the hydrogen atom in this spectral range at 121.6 nm, as predicted by Johannes Rydberg.

Regarding the exact spectral range of VUV radiation, different definitions exist: ISO 21348 specifies 10–200 nm while the German standardization institute defines it as the range of 100–200 nm in DIN 5031. In the LIBS community, it most often means the range of 100–200 nm. This corresponds to photon energies of 6–12 eV, which are considered as ionizing radiation and therefore require additional safety precautions when working with higher intensities than emitted by the LIBS plasma.

In this spectral range, the methods of geometrical and physical optics known from the visible spectral range are applicable without limitations and hence VUV radiation can, in principle, be dealt with as any other light. There are, however, some challenges to keep in mind.

Atmospheric absorption As the name already suggests, observations in this spectral range require vacuum. The reason for this is that some atmospheric molecules, such as O_2 and H_2O, but also, for example, CH_4 and CO_2 have strong absorption bands in this range. It is, however, possible to conduct the experiments in an Ar, He or N_2 atmosphere, which is transparent for VUV radiation.

Absorption in glasses The optics used for VUV experiments need to be considered as well. Englisch [69] investigated the transmission through different types of quartz glass, which are

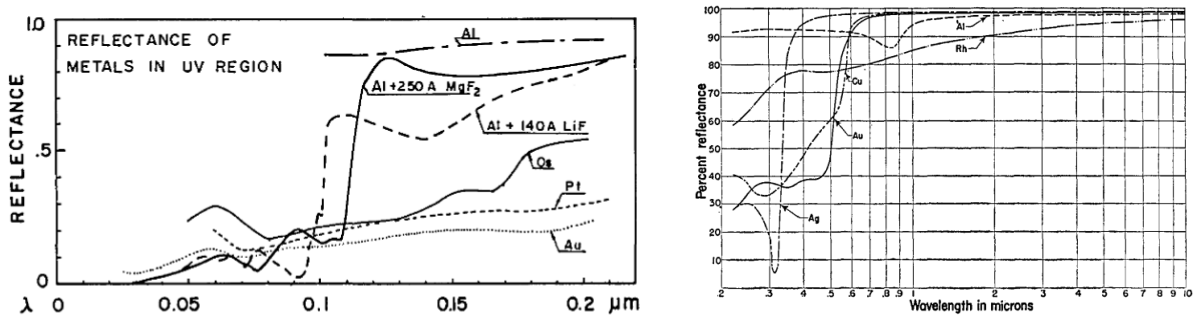

Figure 2.3: Reflectivity of different mirror coatings in the VUV (left) and UV-VIS-NIR (right) range. Bare Al has the best reflectivity in this spectral range but oxidizes quickly in atmosphere. Images reprinted with permission from Loewen and Neviere [71] (left) and Hass [72] (right) ©The Optical Society.

commonly used for lenses, and found that the lowest achievable wavelength for which radiation is transmitted is in the order of 170 nm. As an alternative, certain fluorides, mainly MgF_2 and CaF_2, can be used [70]. However, since they are also close to their absorption edges, the chromatic aberrations introduced by such fluoride lenses are strong.

Reflectivity of mirrors To avoid transmission losses and, at the same time, chromatic aberration, it is advisable to use reflective optics instead of lenses. Many metals like Ag, Au and Cu that are commonly used for mirror coatings, unfortunately show a decreased reflectivity towards short wavelengths [72]. Only Al was found to have a reflectivity above 90 % for 200 nm and below. However, unprotected Al tends to oxidize quickly, resulting in a low reflectivity aluminium oxide surface [73]. Therefore, it needs to be protected by a protective layer of VUV transparent material. In many cases, a thin layer of MgF_2 is deposited on the fresh aluminium layer.

Instrument response calibration Another aspect to consider is the calibration of the spectral response of the instrument. Most calibration lamps are packed in glass bulbs, so that even if VUV radiation is produced it cannot be used for calibration. Only few lamps with a MgF_2 window are available that can serve as a reference. For the VUV telescope of the Solar and Heliospheric Observatory (SOHO), a hollow cathode source that can be operated without a window has been used as a transfer standard [74]. The hollow cathode source itself had been referenced to a synchrotron source before, since thermal black body radiators do not reach into this spectral range.

2.4 Raman spectroscopy

Other than LIBS, Raman spectroscopy is a method sensitive to the vibrational modes of molecular functional groups and to the phononic properties of lattice structures [75]. This complementary nature can be useful for, e.g., sulfate analysis in a geological context, where the cation is easily identified with LIBS while the sulfur of the anion is rather challenging to detect [76]. The anionic sulfate group, on the other hand, can be well identified by its Raman spectrum, which is only little influenced by the choice of cation. Combining both methods has thus been proposed multiple times for different applications [77–79].

The Raman effect is an inelastic scattering process and was theoretically predicted by Smekal [80]. Experimental confirmation of the effect is attributed to the Indian physicist Raman and his colleagues who demonstrated it in 1928 [81]. Raman was awarded the 1930 Nobel prize in physics for his experimental proof. Landsberg [82] also observed the Raman effect at approximately the same time. This questions Raman's precedence and is the reason why in literature from the former Soviet Union the effect is often referred to as combination scattering. In the beginning of Raman spectroscopy, mercury lamps were used as narrow band excitation sources while detecting the signal with photographic plates. Due to the low intensity of scattered light, measurements

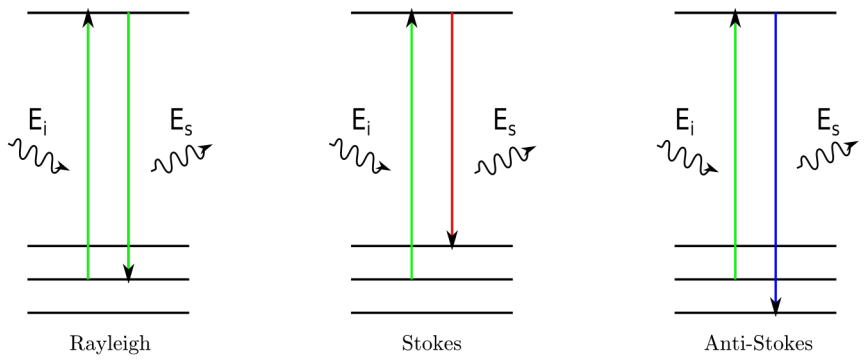

Figure 2.4: Rayleigh and Raman scattering. The left panel shows the elastic Rayleigh scattering, where the system is excited to a virtual state and then relaxes back to the initial state. The photon emitted upon relaxation has the same energy as the incident photon. In the inelastic Raman scattering process, the system ends in a vibrationally excited state (Stokes process) or in a lower vibrational state than it has been before excitation (anti-Stokes process), as shown in the middle and right panel, respectively. The photon emitted after scattering is then red- or blue shifted, respectively, according to the energy difference between the involved vibrational levels. E_i, E_s denote the energy of the incident and scattered photon, respectively. Figure adapted from Kubitza [83].

took several hours. With the invention of the laser, amplifiable photoelectric detection and improved spectral filters, Raman spectroscopy became handier and emerged to a widely used technique in mineralogy, biology and forensics.

In the Raman process, the sample system is excited to a virtual state, from which it quickly relaxes. In most cases, the system will be back in the initial state after relaxation and a photon of the same energy is emitted. This elastic scattering process is named Rayleigh scattering and is depicted in Figure 2.4 (left). In some cases, the photon may exchange energy with the sample system and excite a molecular vibration. In this inelastic Stokes process, depicted in the middle panel, the energy of the scattered photon is lowered by the quantized energy of the excited vibration. Inversely, if the system was in a vibrationally excited state before, a vibrational quantum can be annihilated in a so-called anti-Stokes Raman process, transferring the vibration energy to the scattered photon, see the right panel in Figure 2.4.

Each Raman mode can be assigned a wavelength-dependent scattering cross-section for a given configuration of scattering angle and polarization of the ingoing and outcoming light with respect to the molecular axis. Thus, for a fixed measurement geometry and polycrystalline samples with statistically distributed orientations of the molecule axes, the intensity of the detected Raman scattered light can be expected to be proportional to the number density of the respective molecule.

Chapter 3

Sample preparation and characterization

In this project, pure metal samples as well as pellets of pressed powders were used. The pressed samples have been prepared in our laboratory from reagent grade chemicals and lunar simulants. Their homogeneity has been investigated with Raman spectroscopy. In this chapter, I will first present the Raman spectroscopy set-up used to characterize the samples. Then, I will describe the sample preparation procedure for the pellet samples and finally characterize the samples.

3.1 Raman spectroscopy set-up

The Raman spectroscopy set-up used for this work was originally built to investigate the capabilities of a small, lightweight and as simple as possible instrument for in-situ space exploration [84, 85]. Figure 3.1 shows a schematic drawing. For excitation, a fibre-coupled frequency-doubled continuous wave (cw) Nd:YAG laser emitting at 532 nm is used. The optical power delivered to the sample is 15 mW. The laser radiation is collimated using a fibre collimator, passes a short-pass beam splitter with a cut-off wavelength of $\lambda_c = 535$ nm and is focused onto the sample with a cemented achromatic doublet of $f = 100$ mm focal length. Raman scattered light is collected through the same lens, diverted at the beam splitter, passes through a Rayleigh scattering suppressing long-pass filter and is then focused into an optical fibre ($d = 400$ µm, NA 0.22), using another achromatic doublet of $f = 60$ mm. The fibre guides the light to a commercial miniaturized spectrometer, which covers the spectral range 530–700 nm, where it is finally analysed.

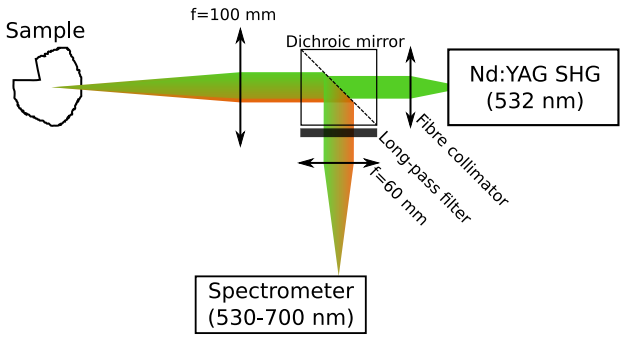

Figure 3.1: Sketch of the Raman spectroscopy set-up. The laser radiation is inserted using an optical fibre and a fibre collimator. After passing through a dichroic mirror, the laser light is focused onto the sample with an achromatic doublet of $f = 100$ mm. Backscattered light is collected with the same lens, diverted at the dichroic mirror, passes a Rayleigh suppressing long-pass filter and is inserted into an optical fibre (not shown here) transporting the radiation to a miniature spectrometer.

Element	LHS-1	LMS-1
O	60.4	59.4
Si	15.6	15.2
Al	10.9	5.9
Mg	5.9	10.0
Ca	4.4	2.3
Na	1.6	3.4
Fe	0.8	2.1
Ti	0.2	1.2
K	0.2	0.3
P	—	0.1

Table 3.1: Chemical compositions of LHS-1 and LMS-1 in at%. Only constituents with more than 0.1 at% are listed. Both simulants contain traces of Cr, Mn and S.

3.2 Sample preparation

For initial line identification, pure metal samples and salt pellets were used. The commercially available metal samples are sputtering targets of Al, Cu, Fe, Ni, Ti and Zn with a purity of 99.60–99.99 %, as well as a silicon wafer. The salt pellets have been prepared from reagent-grade chemicals and include different carbonates and sulfates, as well as sodium chloride (NaCl) and calcium phosphate ($Ca_3(PO_4)_2$). A pellet of sulfur powder has been analysed as well. For the studies in a lunar context, sulfur powder, sodium sulfate (Na_2SO_4), potassium sulfate (K_2SO_4) and NaCl have been mixed with lunar analogue materials. The analogue materials are a Lunar Highland simulant (LHS-1) and a Lunar Mare simulant (LMS-1). LHS-1 consists of mainly plagioclase and glass and thereby reflects the average geology of lunar highlands [86]. LMS-1, on the other hand, is a mix of pyroxene, glass, plagioclase, olivine, basalt and ilmenite. It resembles medium to high titanium basalts typical for the dark Mare areas [86]. The elemental compositions are listed in Table 3.1. Both simulants have been acquired from the Center for Lunar & Asteroid Surface Science Exolith Lab [87], an institution within the University of Central Florida. The mixing ratios have been calculated to prepare samples that are equidistant in molar fraction of the analyte, e.g. S. These calculations are based on the assumption of homogeneous, infinitely small grains of lunar analogue, which is naturally not the case.

For the mixed samples, the two components, matrix and admixture, have been weighed separately using precision scales with a display resolution of 1 mg. To avoid weighing amounts smaller than approximately 50 mg for the lowest intended concentrations, a larger amount of the mixture for the highest concentration in the series has been prepared and then diluted again with matrix material. The targeted total mass per sample was 1 g. After weighing, the components were carefully mixed using mortar and pestle. Care was taken to increase the sample homogeneity by crushing especially large ($\gtrsim 0.5$ mm) grains. The smaller grains were, however, not further crushed or ground on purpose in order to maintain the lunar simulant's grain size distribution as far as reasonable, as it intends to mimic the grain size distribution of real lunar regolith. The mixture was then filled into a pellet die of 13 mm in diameter and pressed for 10 min at 750 MPa ($\approx$10 t). For the pure salt and sulfur samples, 1 g of the respective material was weighed and in most cases directly filled into the pellet die and pressed to a pellet (10 min at 320 MPa). The higher pressure for the lunar simulant samples was used in order to make the samples less fragile after some samples broke while transferring them to the sample holder. However, a significant decrease of the sample fragility has not been observed for the higher pressure and some of the lunar simulant samples broke as well.

The total uncertainty expected per weighing is up to ± 5 mg due to the display resolution as well as linearity and reproducibility uncertainties as stated in the manual of the precision scales. This results in a maximum uncertainty for the bulk analyte concentration of the pressed pellet of ± 0.05 at% for all prepared samples. Due to reordering of the grains while pouring the

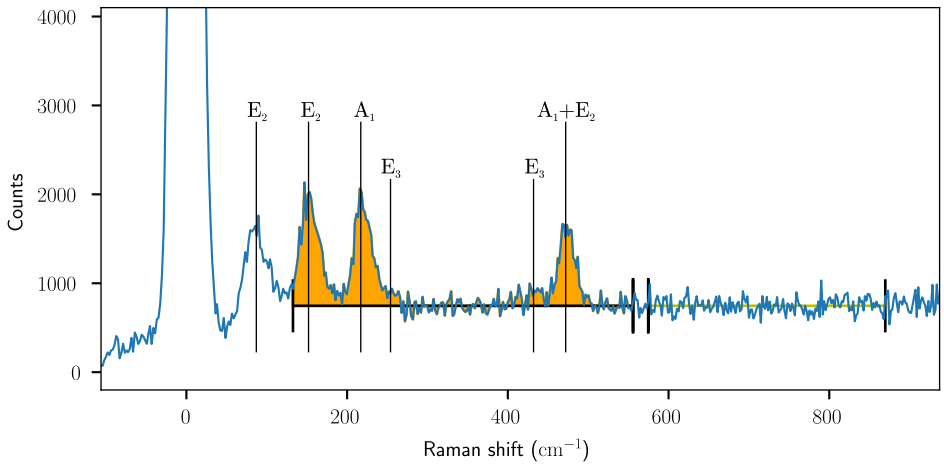

Figure 3.2: Example Raman spectrum of LHS-1 mixed with S powder at a concentration of 2.0 at% S. Five spectra with an exposure time of 5 s have been averaged. A constant background level is estimated from the range between 570 and 870 cm^{-1}. The sum over the range 130–550 cm^{-1} after background subtraction, shaded in orange, is used as Raman signal. The thin vertical lines indicate the positions of S_8 Raman modes [89].

mixed powder into the pellet die, the local concentration can, however, vary across the sample volume. Therefore, the sample homogeneity is characterized with Raman spectroscopy in the next section.

3.3 Sample characterization

Crystalline sulfur is a strong Raman scatterer and the Raman signal intensity is proportional to the concentration of the scatterer. Hence, Raman scattering can be used to detect the relative local surface concentration across the sample surface and thereby investigate the homogeneity of the sample with respect to the sulfur concentration. The SO_4^{2-} sulfate group is also known to be strongly Raman-active [88], but none of the SO_4^{2-}-related Raman modes could be detected in the sulfate-bearing samples, likely due to too low concentrations. Therefore, only samples containing pure sulfur have been investigated.

For the LHS-1 samples mixed with 2.0, 3.5 and 6.0 at% S, an area of $7 \times 0.25\,mm^2$ has been probed with the Raman spectrometer. The area has been scanned at a step size of 50 µm, which corresponds to the calculated spot size of the Raman laser. An example Raman spectrum taken from the sample with 2.0 at% S is presented in Figure 3.2. It shows multiple strong Raman modes around 85 (E_2), 150 (E_2), 215 (A_1) and 470 cm^{-1} (A_1+E_2) as well as two weak modes at 250 (E_3) and 430 cm^{-1} (E_3), all related to the S_8 molecular unit [89]. Raman modes of the minerals of the lunar highland analogue matrix or luminescence of the sample have not been observed in any of the spectra. Therefore, the average signal level in the feature-free range from 570 to 870 cm^{-1} can be taken as the background level and subtracted from the spectrum. The sum over the spectral range of 130–550 cm^{-1} is then used as a measure for the Raman signal intensity. The mode at 85 cm^{-1} is excluded from the sum, because it is already affected by the Rayleigh filter and the background signal is not constant in this range.

The spatial distributions of the Raman signal for the three investigated samples are shown in Figure 3.3. The signal has been normalized to the maximum value per sample. For a better visibility, the greyscale has been stretched and values above 0.8 are coloured black. The images show significant heterogeneities of the S signal for all three samples. Especially in the results for 2.0 at% S one can see spots that are strongly enriched in S compared to the rest of the sample, e.g. in the columns around 1.9 and 4.4 mm.

Despite the observed heterogeneity on the 50 µm scale, the samples might still be homogeneous on the scale of the LIBS spot size, i.e. ≈500 µm diameter, which is the relevant measure

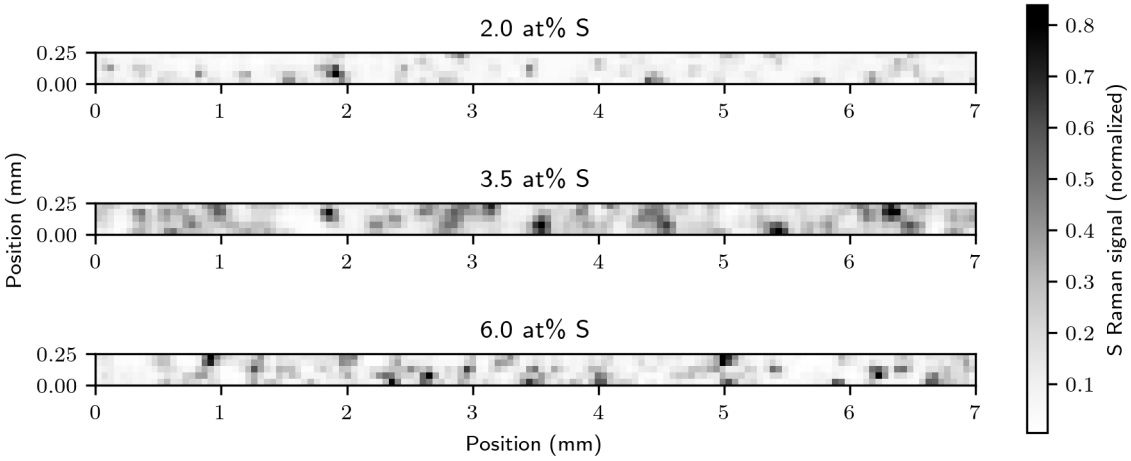

Figure 3.3: Spatial distribution of the integrated S Raman signal across the sampled area of the S-in-LHS samples with 2.0, 3.5 and 6.0 at% S. The signal is normalized to the maximum detected signal per sample. On this scale of a 50 µm raster, local enrichments and depletions are evident.

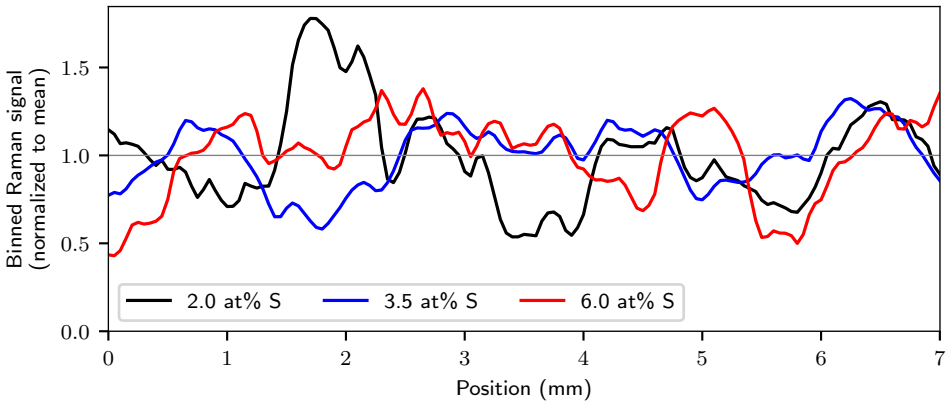

Figure 3.4: The Raman signals shown in Figure 3.3 have been summed column-wise before applying a boxcar average with a total width of 15 pixels. The results, averaged to the mean, give an estimate of the homogeneity of the local S concentration on the scale of the LIBS spot size for the three analysed samples. The relative standard deviations for the 2.0, 3.5 and 6.0 at% S samples are 28, 18 and 23 %, respectively.

for the VUV-LIBS studies. Therefore, the signals shown in Figure 3.3 are summed column-wise and then a 15 pixel wide boxcar average, corresponding to 0.75 mm in the x direction, is applied. The result is now comparable to a Raman spectroscopy measurement with a spot size as large as the LIBS sampling area. Signal fluctuations observed on this scale should indicate a variation in the actual local S concentration, although only close to the surface. The summed and averaged signals are shown in Figure 3.4. They are normalized to the respective mean per sample to emphasize the deviation from the bulk concentration. Even on this larger scale, strong fluctuations of the signal are evident, especially for the 2.0 at% S sample. The relative standard deviation of the displayed data, providing an estimate of how much the local concentration at a randomly LIBS-probed location might differ from the bulk concentration, amounts to 28 % for 2.0 at% S. For 3.5 and 6.0 at% S, the relative standard deviation amounts to 18 and 23 %, respectively.

These results show that the homogeneity of the LHS-based samples is limited and varies between different samples. This should be kept in mind when establishing LIBS calibration curves or estimating detection limits from the data. The area probed with the Raman spectrometer is, however, not the same as the area probed with the VUV-LIBS system, because the LIBS system does not allow precise targeting of particular locations in its current configuration, and for post-LIBS Raman spectroscopy measurements, the sample may have been altered by the LIBS pulse and produce unrepresentative results [79, 90, 91].

For the data recorded for chapter 6, where Na_2SO_4 is mixed in three different matrices, an analysis of location-to-location scattering of different LIBS emission line intensities suggests that the large grain size (94 µm on average) of LHS-1 is responsible for the heterogeneity. The analyte and matrix LIBS signals of samples based on the finer grained LMS-1 (63 µm on average) fluctuate in general less than in LHS-based samples. For $NaSO_4$ in a Na_2CO_3 matrix, the LIBS signal of S is even more stable for concentrations of 1.5 at% S and above. At lower concentrations for this sample series, the signal-to-noise ratio is in the order of 3–5 and the signal variance is thus dominated by detector noise.

Chapter 4

Design and characterization of the VUV-LIBS set-up

In this chapter, I will describe the VUV-LIBS set-up, which has been developed around a commercial grating spectrometer as part of this doctoral project. After describing this spectrometer as the central part of the set-up and presenting first results recorded with a temporary vacuum chamber, I will formulate requirements for the actual VUV-LIBS set-up that determined the development process, followed by a description of the resulting set-up. Then, different aspects of the set-up will be characterized, also pointing out limitations of the current configuration that should be improved in a next iteration of the set-up. The characterization includes the dark rate and noise behaviour of the detector, an estimate of the relative sensitivity across the spectral range of operation and an analysis of the relevant broadening mechanisms. Finally, the procedure of data processing is described, where the sensor images are converted into spectra.

4.1 Description of the spectrometer

For this project, the VUV spectrometer easyLight from Dr. Hörlein und Partner was used. It covers the spectral range of 100–300 nm at a nominal resolution of 0.1 nm. The major components of the spectrometer are described below, including a section (4.1.1) about the calibration of the entrance slit width. At the end of this part, in section 4.1.2, a preliminary conversion scheme from camera images to spectra will be provided.

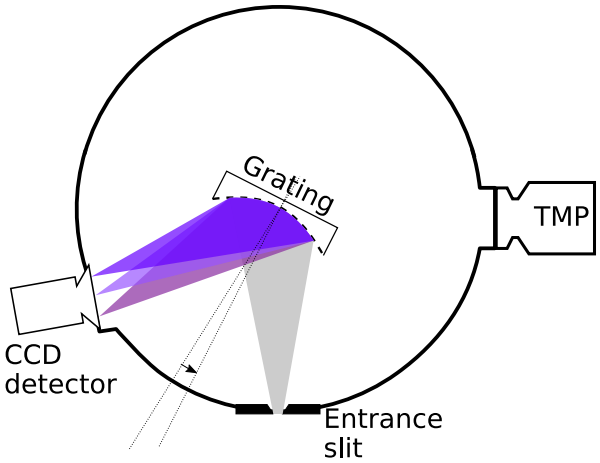

Figure 4.1: Schematic drawing of the spectrometer. The spectrometer uses a single concave grating for both dispersion and projection. The diversion angle between the ingoing and outgoing rays is 64°. The CCD detector is tilted by approx. 38° to be tangentially aligned on the Rowland circle. The grating is mounted on a rotational stage and can be turned towards the entrance slit for wavelength tuning. A turbomolecular pump (TMP) flanged directly to the spectrometer ensures an operating pressure of less than 10^{-2} Pa.

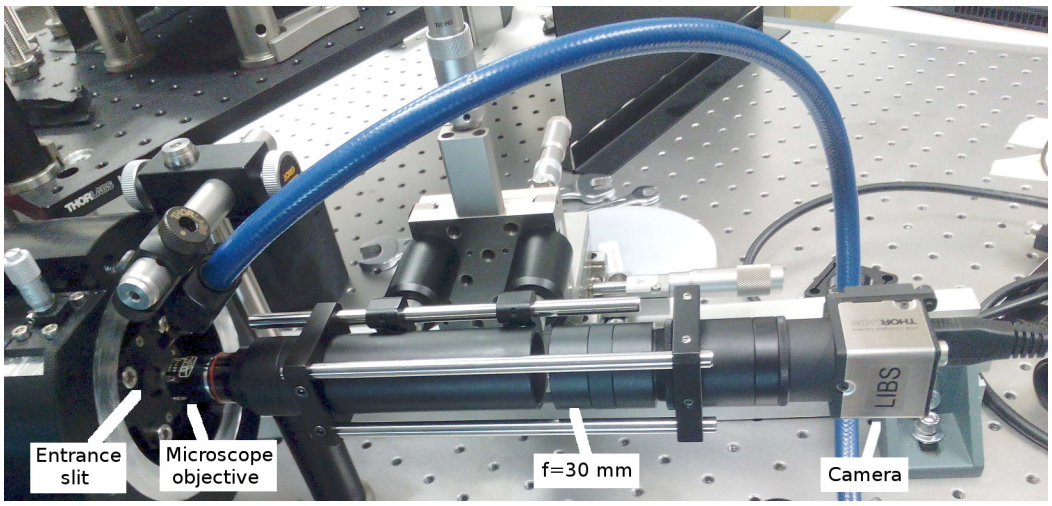

Figure 4.2: Microscope camera assembly used to measure the width of the spectrometer's entrance slit. It uses a 6.3× microscope objective, a 30 mm achromatic doublet and a monochromatic CMOS camera, resulting in a sampling scale of 1.04 px/µm. The working distance is 5 mm. For illumination, a fibre-coupled incandescence lamp is used.

The spectrometer adopts the Paschen-Runge geometry, where a single imaging grating is used to both image the entrance slit onto the detector and spectrally resolve the radiation. A schematic drawing is shown in Figure 4.1. The angle between the incident and the diffracted light at the centre wavelength is 64°. The distance from the entrance and exit ports to the grating is 20 cm. Compared to the commonly employed Czerny-Turner concept, this layout has the advantage of using only one mirror, thereby avoiding reflection losses, which can be significant in the VUV range. This advantage, however, comes with an in general lower optical performance in terms of image quality. The light is inserted through an entrance slit of variable width. The scale reading on the adjustment screw does, however, not coincide with the actual slit width and therefore needed calibration. The calibration of the entrance slit width will follow this description of the spectrometer, in section 4.1.1. The grating with 1200 lines/mm is made of a cylindrical glass substrate and coated with Al+MgF_2. The efficiency is stated with 40 % in the range 120–200 nm and higher than 20 % over the full operating range of 100–300 nm. The grating is mounted on a rotation stage to adjust the 80 nm wide range of observation. According to the manufacturer, it is a corrected concave grating, meaning its groove spacing is altered to correct for optical aberration. Such corrections can significantly improve the resolution and the sharpness of the spectral lines. Additionally, the size of concave gratings is typically limited to avoid aberrations due to oblique components of the incident light [92]. Despite the corrected grating, a large instrumental broadening has been observed, leading to a typical full width at half maximum (FWHM) in the order of 0.3 nm for the LIBS emission lines. This broadening is inspected in detail in section 4.3.4. The detector is an open front charge coupled device (CCD) developed mainly for soft x-ray applications. It is mounted with an angle of 38° between the optical axis and the detector normal. The quantum efficiency peaks between 125 and 140 nm with approximately 27 %. Towards 200 nm it decreases to 20 %. Below 125 nm the quantum efficiency drops quickly to 13 %. The CCD chip has 1024 × 255 pixels of 26 × 26 µm^2 size. It can be thermoelectrically cooled to −80 °C. To ensure a low pressure and thereby reduce the absorption of VUV radiation by oxygen and water vapour in the ambient air, a turbomolecular pump and a pressure gauge are connected to the spectrometer.

4.1.1 Calibration of the entrance slit width

The width of the spectrometer's entrance slit can be adjusted with a micrometre screw. To achieve the desired resolution of 0.1 nm, the slit width has to be in the order of the detector's pixel size, i.e. ∼26 µm. Selecting a slit width below 50 µm according to the reading on the micrometre

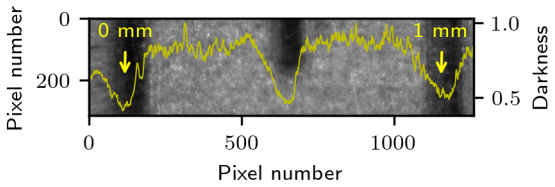

Figure 4.3: Image section of a metal ruler used to determine the magnification of the optical system. The dark parts are the scale markers of the ruler. The grey level or darkness of the upper image rows is overlaid in yellow. From this curve, a magnification or sampling scale of 1.04 px/µm has been deduced.

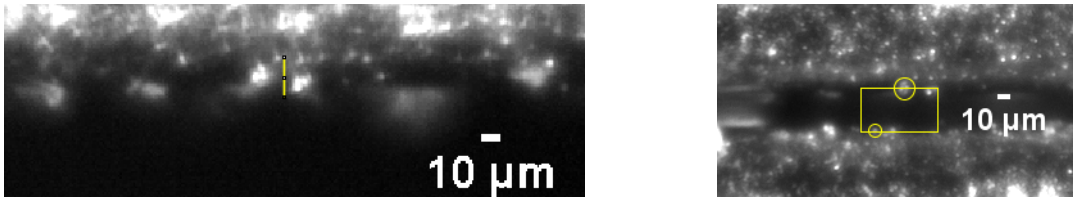

Figure 4.4: *Left:* Bright spots on the entrance slit due to roughness and potentially dust disguise the exact position of the edge. An uncertainty of 20 µm, indicated by the yellow bar, is assumed for each side. *Right:* Image of the slit taken for the setting "100 µm" on the micrometre screw. The width is determined as the vertical distance between the two reference bright spots indicated with circles. The measured slit width for this setting is 34 µm.

screw, however, leads to a complete vanishing of the detector signal, thereby suggesting that the screw reading does not directly indicate the slit width. To investigate the actual slit width and its relation to the screw reading, I assembled a microscope camera from a 6.3× microscope objective, a cemented achromatic doublet with a focal length of $f = 30$ mm and a monochromatic CMOS camera with a pixel size of 5.3 µm. The camera assembly with a working distance of approximately 5 mm was mounted on a translation stage and aimed at the spectrometer entrance slit. It is shown in Figure 4.2. The sampling scale of this camera assembly has been calibrated by recording an image of a metal ruler. A section of this image is shown in Figure 4.3. It shows two major ticks with a distance of 1 mm and an intermediate tick between them. A line plot of the pixel darkness for the upper rows of the image is shown in yellow. The pixel distance of the dips is 1039, resulting in a sampling scale of 1.04 px/µm.

A close-up image of one of the entrance slit edges is shown in the left panel of Figure 4.4. One can see various bright spots related to roughness of the razor blade and potentially dust, obscuring the exact position of the edge. From the image, I take an uncertainty of the edge position in the order of 20 µm on each side, as indicated with the yellow marker. For the width measurements, a bright spot on either side of the slit has been selected as the reference and the vertical distance between them has been measured as shown in the right panel of the figure. The bright spots used as references are marked with circles. By using a fixed reference, the uncertainty of the edge position only causes a potential constant offset in the derived slit width. Since the field of view was sufficiently large to image both edges at the same time for all investigated width settings, an uncertainty due to a translation of the camera system was not induced.

The width has been measured for settings decreasing from 1000 to 100 µm in steps of 50 µm. The results are summarized in Table 4.1 and visualized in Figure 4.5. From the figure, the

	Slit width (µm)									
set	1000	950	900	850	800	750	700	650	600	550
measured	654	604	569	540	499	453	399	352	303	254
set	500	450	400	350	300	250	200	150	100	
measured	215	179	162	145	122	101	81	56	34	

Table 4.1: Results of slit width measurements for different set values of the micrometre screw.

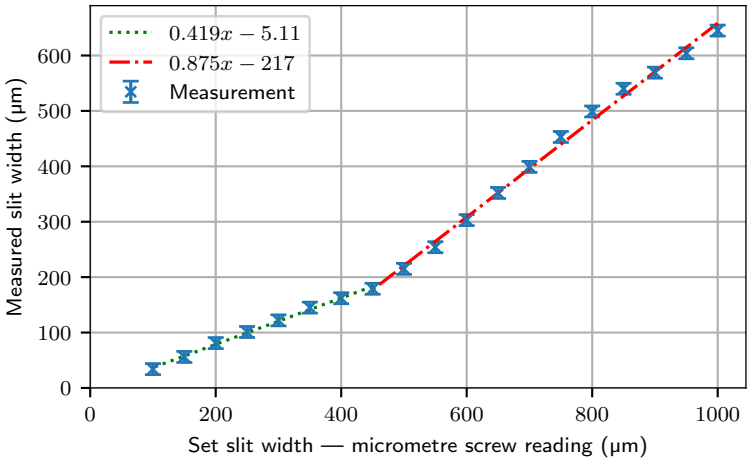

Figure 4.5: Comparison of the reading on the micrometre screw to the measured slit width. The data shows two linear sections with a sharp bend around the 450 µm setting.

relation of the screw adjustment to the slit opening is found to have two linear segments with different slopes. Above the 450 µm setting, the measured slit width increases twice as fast. A linear regression for either part shows a coefficient of determination (R^2) of >0.996.

For a typical measurement, a scale reading on the slit adjustment screw of 150 µm has been found to be a good compromise between resolution and signal throughput. According to the above analysis, this corresponds to an actual width of 56 µm, which is very close to the width of two detector pixels of the spectrometer (2×26 µm).

4.1.2 Extraction of spectra

The camera is controlled using the software provided with the instrument. The recorded images are saved in a proprietary format, which contains additional information about the detector parameters, such as the exposure time, detector temperature and horizontal and vertical binning. The rotational stage of the grating is not controlled with this software and hence the grating angle must be stored in the file name. With Python routines, which I developed myself, the image data and parts of the metadata are extracted from the binary container. Then, a user-defined range of detector rows is vertically binned to produce a one-dimensional spectrum with numbered spectral channels. For an initial calibration, the wavelength λ_i for the spectral channel i is calculated from the grating equation

$$n\lambda = [\sin(32^\circ + \alpha + \Delta\alpha_i) - \sin(32^\circ - \alpha)]/g\,, \tag{4.1}$$

the selected grating angle α, and the grating constant g. Due to the low efficiency of the system for wavelengths below 120 nm, only the first order ($n = 1$) is considered. The calculation is based on a total angle of 64° between the incident and outgoing light for the centre pixel. The deviation of the output angle for pixel column i is given by

$$\Delta\alpha_i = \arctan\left(\frac{(i - 512)\cdot 26\,\mu\text{m}\cdot\cos 38^\circ}{20\,\text{cm} - (i - 512)\cdot 26\,\mu\text{m}\cdot\sin 38^\circ}\right). \tag{4.2}$$

Here, $\cos 38^\circ$ in the numerator accounts for the apparent decrease of the pixel width induced by the angled detector mount. A corresponding correction of the grating-to-detector distance is incorporated in the denominator. Due to a mismatch of this initial wavelength calibration and optical aberrations observed during the characterization of the set-up, see sections 4.2 and 4.3.4 for details, a more sophisticated data processing procedure has been developed. It will be presented in section 4.4.

4.2 First measurements with a preliminary system

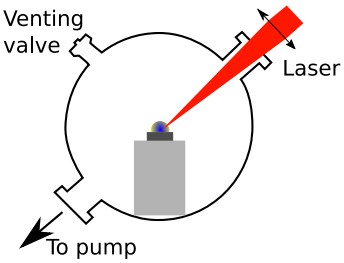

Figure 4.6: Sketch of the preliminary sample chamber used for initial testing and to define requirements for the final set-up. The sample is placed on an aluminium block and irradiated under an angle of 45°. The pump is connected via a vacuum hose. The optical axis of detection is directed into the drawing plane. Hence, from this perspective, the spectrometer entrance slit is located in the background behind the sample.

Initial tests with the new spectrometer were conducted with a preliminary vacuum chamber. The chamber comprised a DN 63 ISO-K instrument cross with three ports, as depicted in Figure 4.6, which was flanged directly to the spectrometer entrance port housing the slit. A 40 mm vacuum hose was connected to the first port, a venting valve to the second and a window to insert the laser radiation closed the third port. The other side of the cross, opposite to the spectrometer, was terminated with a window to observe the plasma and align the laser. The sample was placed on an aluminium block of a suitable height to have the sample surface centred in front of the entrance slit. In this preliminary set-up, the sample was irradiated under an angle of 45°.

An image recorded with the temporary set-up at a grating angle of 7° from a LIBS plasma of an aluminium disk is shown in Figure 4.7. Spectral line emission is clearly evident already in this early recording. However, the LIBS spectrum is projected only onto the upper part of the detector area and is limited by a funnel-shaped envelope, whose upper side is not visible in

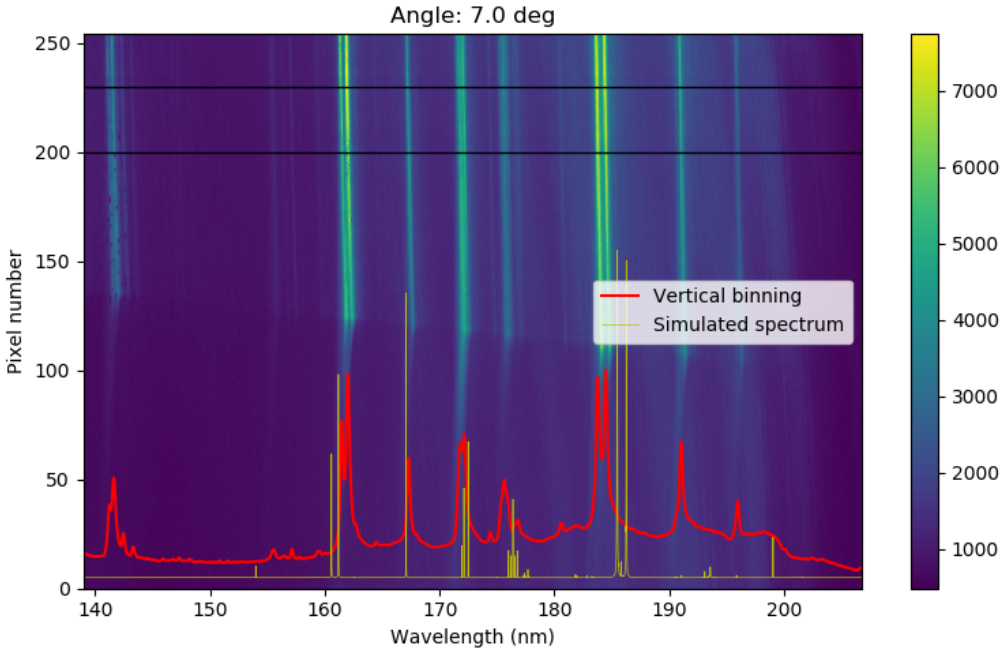

Figure 4.7: Recording of an Al plasma in the preliminary sample chamber. The spectral lines are offset to the top, tilted, and have some kind of reflected continuation towards the bottom. A line spectrum derived from the detector rows 200 to 230, as indicated by the black markers, is shown in red and compared to a simulated spectrum (yellow). A mismatch of the wavelength scale, which was geometrically calculated from the grating constant, the nominal focal length, the pixel size and the grating angle, can be seen.

this image but has been observed in other recordings. Elevating the sample with washer disks allowed to move the spectrum to the centre of the detector, with the lines now spanning the full height of the detector and, at the same time, eliminating the reflected continuation of the lines towards the bottom of the image. This suggests that the imaging grating in the spectrometer as adjusted by the manufacturer was not upright but leaning back with an angle of about 1°. During a re-alignment of the optical components at a later stage, the grating mount has been shimmed with aluminium foil on the back side in order to correct the angular displacement.

In the right part of the image, a broad and slightly tilted background structure spanning the whole height of the image is visible. This structure proved to be independent of the grating angle and was therefore found to be not a spectral signal from the plasma. It was attributed to stray light passing through venting holes positioned around the entrance slit of the spectrometer and was successfully suppressed by covering these venting holes with black aluminium foil.

Finally, another observation from Figure 4.7 is the mismatch of the wavelength scale. It has been calculated using the grating equation and the nominal specifications as explained in section 4.1.2. The spectrum overlaid in red is the vertically binned intensity of the image rows 200 to 230, as indicated with black horizontal lines in Figure 4.7. The second spectrum, shown in yellow, has been simulated as described in section 2.1.3 and maps the reference positions of Al emission lines onto the calculated wavelength scale. When aligning the wavelength scale in the middle of the observed spectral range, the outer parts are up to 5 nm off. This is due to incomplete knowledge about the exact effective grating constant, the exact distances between entrance slit, grating and detector, and the precise angle of deflection and of the camera mount. An attempt to constrain those parameters by fitting the derived wavelength equation to the simulated reference positions did not succeed. Therefore, the geometric calibration was later replaced by a calibration based on the positions of identified spectral lines, as will be shown in section 4.3.3.

4.3 VUV-LIBS set-up

In this section I will first describe the VUV-LIBS system that I designed around the grating spectrometer presented in section 4.1, before analysing different aspects of the assembled system, namely the dark current and noise behaviour of the detector, the spectral sensitivity of the set-up and relevant instrumental broadening mechanisms. This configuration of the VUV-LIBS set-up will then be used for the identification of VUV emission lines in chapter 5, as well as for the S- and Cl-related studies presented in chapters 6 and 7, respectively.

4.3.1 Design

Like conventional LIBS, the method in general requires a laser, a spectrometer and an optical system for focusing and light collection. One of the key differences for VUV-LIBS is that the optical path must be contained in a vacuum chamber and uses VUV-compatible optics, see also section 2.3. This section focuses on the layout of the vacuum system and the optical design. While details about the spectrometer have been provided in section 4.1, the laser used in the set-up will be described at the end of this section. For the design of the VUV-LIBS set-up, four major requirements have been identified and needed to be accounted for:

1. Pressure $< 10^{-2}$ Pa
   In order to investigate VUV-LIBS for the in-situ application on celestial bodies without atmosphere, near-vacuum conditions need to be simulated. Knight et al. [21] found that while the LIBS process is, in general, strongly influenced by the atmospheric conditions, no significant changes can be observed for pressures below approx. 1 Pa. Furthermore, absorption due to atmospheric oxygen becomes negligible at this pressure [93]. A more sensitive requirement is the protection of the detector from condensing water vapour, which might freeze on the cooled CCD chip and result

in permanent damage. In order to minimize this risk, the requirement was set to 10^{-2} Pa in accordance with the recommendations of the manufacturer.

2. Load lock capability
   Since an open connection between the sample containing vacuum chamber and the spectrometer is required during the measurement, it would be of advantage to be able to atmospherically decouple both parts of the system. This allows to change the samples without the need to flush the spectrometer and then evacuate it again, which would also require looping through a warming-cooling cycle to protect the CCD against condensation.

3. Sample translation in at least one direction
   In order to be able to analyse multiple locations per sample and potentially also multiple samples per pump cycle, it is necessary to move the sample in the chamber. In previous measurements with the temporary chamber, extensive "drilling" into the sample has been observed when probing the same location multiple times. This visually changed the plasma shape due to plasma confinement [94] and inhibited the comparison of subsequent measurements.

4. Relay optics
   To couple sufficient plasma radiation into the spectrometer, one can either excite the plasma in proximity to the entrance slit [27] or image the plasma onto the slit using relay optics. To mitigate the risk of ablated material depositing inside the spectrometer and to compensate for the inherent minimum distance between the sample and the spectrometer when installing a valve to satisfy requirement 2, I decided to use relay optics.

Finally, for this first instance of a VUV-LIBS system, another condition was to use commercial off-the-shelf components wherever possible. The resulting set-up is schematically shown in Figure 4.8. The central part of the vacuum chamber is a DN 100 ISO-K 6-way pipe cross. The bottom connector is closed with a blank flange. The resulting flat surface allows to place post mounts with additional optical components, such as the apertures described in section 4.3.4.

One of the four side ports, facing towards the user, is equipped with a door and facilitates sample exchange. A window in the door allows to observe the plasma. A manually operated one-axis manipulator is attached from the left. With this manipulator, the sample stage can be moved perpendicular to both the excitation and detection optical axis over a range of 25 mm, thus satisfying requirement 3. The sample stage has been machined from stainless steel by the institute's workshop. It is designed such that the probed spot on the sample surface is located near the centre of the 6-way cross.

To the right, a turbomolecular pump is flanged directly to the chamber. This allows for fast evacuation to a typical operating pressure of $\leq 5 \times 10^{-3}$ Pa, thus fulfilling requirement 1, and efficient removal of ablated sample material. In combination with the pump mounted at the spectrometer, pressure gradients across the spectrometer's entrance slit, which acts as a bottleneck in the vacuum piping, are avoided.

Towards the top, an instrument cross hosting a pressure gauge and a venting valve follows and is terminated with an uncoated borosilicate window through which the laser light is inserted. The instrument cross and the pressure gauge have been omitted in the figure.

The sixth port, opposite to the door, connects to a high-vacuum gate valve that allows to decouple the sample containing part from the remaining system, thereby fulfilling requirement 2. The other side of the gate valve is connected to a tee connector which follows the optical axis of detection.

To satisfy requirement 4, the radiation emitted by the plasma is focused onto the spectrometer entrance slit with a UV-enhanced $f = 152.4$ mm off-axis parabolic mirror (OAP), bending the light path by 90°. The mirror introduces significant geometric and spectral losses. The former are due to a mismatch between available off-the-shelf pipe lengths and mirror focal lengths. Furthermore, an ellipsoidal or at least toroidal mirror would be preferred to project the plasma plume onto the slit [95]. The aberrated picture of the plasma lies several centimetres behind the

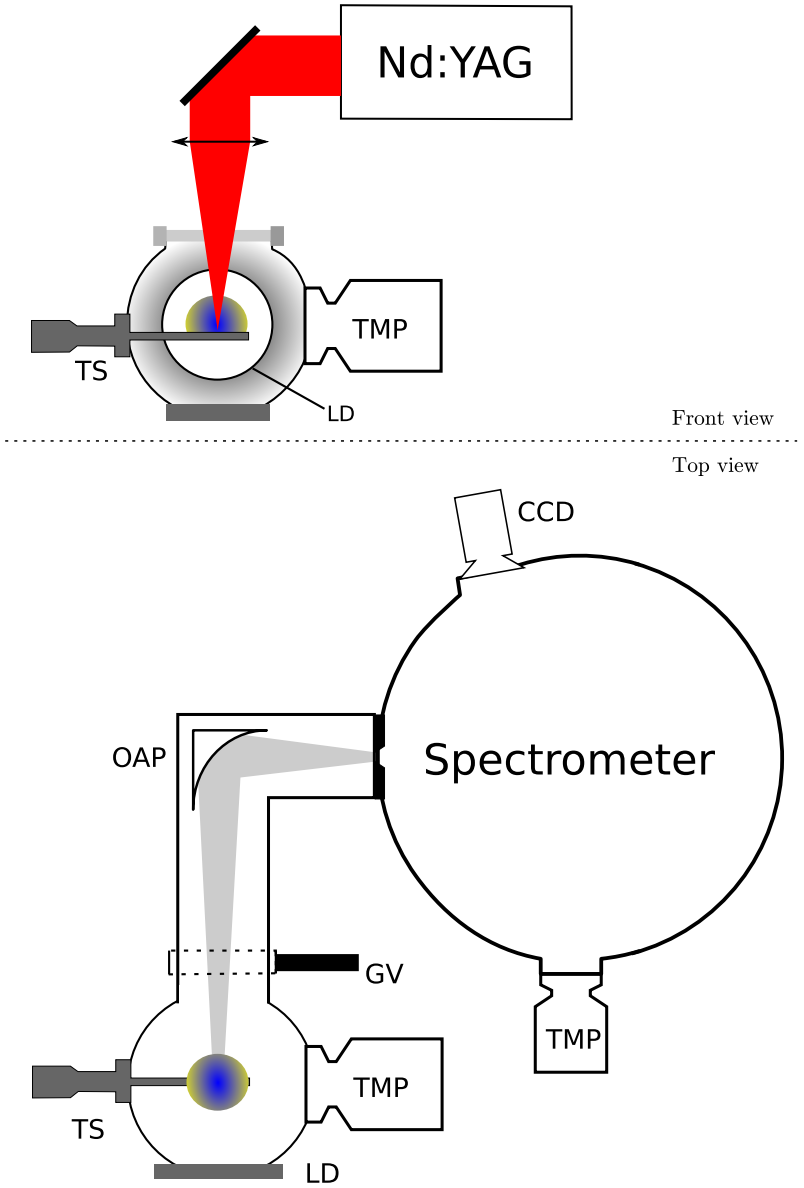

Figure 4.8: Schematic drawing of the VUV-LIBS set-up in a front (upper panel) and top view (lower panel). For clarity, not all components are shown in both perspectives. The laser radiation is inserted into the vacuum system through a borosilicate window and focused vertically onto the sample. Radiation emitted from the plasma is observed from the side and focused onto the spectrometer entrance slit with an off-axis parabolic mirror (OAP). The sample chamber can be atmospherically separated from the spectrometer by closing a high-vacuum gate valve (GV). Two turbomolecular pumps (TMP) ensure a pressure in the system of less than 10^{-2} Pa. LD: load door; TS: translation stage.

entrance slit. Having the picture behind the slit is preferred over the opposite case of having a too short focal length in order to avoid stray light due to light insertion outside the acceptance angle of the spectrometer. The latter, the spectral losses, refer to the wavelength dependent reflectivity of the mirror coating. The reflectivity is specified by the manufacturer only for the range down to 250 nm, where it is around 80 %. Therefore, it will be analysed for the VUV range in section 4.3.5. Both types of signal loss could be improved with a custom design mirror with a VUV-optimized coating for the next iteration of this set-up. Finally, the tee connector housing the OAP is flanged to the spectrometer entrance port.

For longer standby times, the system can be filled with nitrogen (N_2) through the spectrometer pump's venting valve to minimize the deposition of water vapour on the inner walls of the chambers and pipes.

Laser

The laser used in the set-up is an actively Q-switched neodymium doped yttrium aluminium garnet (Nd:YAG) laser. It emits pulses of 6 ns duration at the fundamental wavelength of 1064 nm. The pulse energy of 130 mJ can be internally attenuated to the desired value. The emitted laser light is focused into the vacuum chamber through a borosilicate window using a single antireflection coated lens of focal length $f = 250$ mm. The effective spot diameter, within which the LIBS threshold is exceeded, has been deduced from the widths of the ablation craters. It is approximately 500 µm.

4.3.2 Detector noise and dark current

The CCD chip is mounted on a thermo-electric cooler to allow for noise reduction by cooling and for temperature stabilization. The operating range reaches from −10 to −80 °C, when applying water cooling even down to −100 °C. For most of the line identification measurements in chapter 5 as well as for the sulfur-related measurements described in chapter 6, the CCD was operated at a temperature of −80 °C in order to obtain the lowest detector noise, as recommended by the sales engineer. After observing repetitive noise patterns that occurred suddenly and appeared to be connected to the cooling control circuit, the detector was sent to the manufacturer for maintenance. Since then, a new standard value of −60 °C was chosen and used for the remaining measurements in chapter 5 as well as for the chlorine-related measurements in chapter 7 in order to reduce the load of the thermo-electric cooler. The performance of the system did not seem to be noticeably reduced at this higher temperature.

The two major noise sources for scientific CCD detectors are a constant readout noise, which depends mainly on the readout rate, and the shot noise of the dark current. The dark current is the rate of thermal electron-hole pair generation and strongly depends on the temperature of the detector. To analyse the dark signal and noise behaviour of the system, the gate valve was closed, thus separating the sample chamber from the spectrometer part, to ensure complete darkness around the detector. As during normal measurements, the hot-filament ionization gauge installed in the spectrometer to measure the pressure was turned off, because the incandescence of the filament would saturate the detector within milliseconds. Then 30 images each were recorded for the exposure times 1, 3, 5, 8 and 10 s at the detector temperatures −10, −20, −30, −40, −50, −60, −70 and −80 °C. The first and last three rows and columns were cropped to avoid influences from border artefacts. The signal of the remaining pixels was used for analysis.

The mean signal levels averaged across the 30 images for the various temperatures and exposure times are shown in Figure 4.9a. They are given in digital numbers (DN) as returned by the camera software. The signals are composed of two components: a bias or baseline level and the accumulated dark counts. The bias, which is the reference level corresponding to zero accumulated counts, seems to increase for lower detector temperatures as can be seen from the shortest investigated exposure time. This could be due to a temperature-related drift in the reference voltage of the analogue-to-digital converter of the readout circuit or due to an inappropriate in-

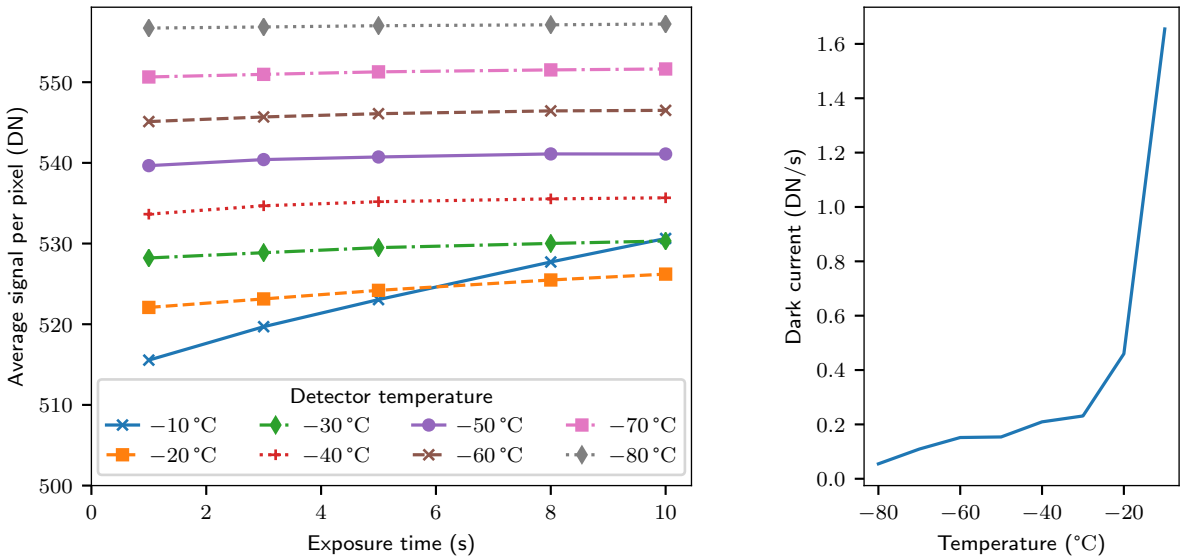

(a) Signal level. **(b)** Dark rate.

Figure 4.9: Dark signal averaged over all pixels of the 30 recorded images per setting. (a) Signal levels produced by the dark detector over different exposure times at different temperatures. The signal is given in digital numbers (DN) as returned by the camera. The baseline level appears to increase linearly with decreasing temperatures. The standard deviation of the data is treated separately and shown in Figure 4.10. (b) Dark current as the slope of the signal level determined by linear regression of the curves in (a). Below approx. −50 °C, the signal hardly changes over time.

ternal calibration to counteract such a drift. The accumulated dark counts are determined by the dark current and can be reduced by cooling. For moderate cooling of only −10 °C, a significant and mostly linear increase of the signal over time can be observed. A linear regression through the data yields a slope of 1.6 DN/s. The fitted dark currents for the different temperatures are shown in Figure 4.9b. For −20 °C, the dark current is already reduced to below 0.5 DN/s and for even lower temperatures the curve asymptotically approaches 0. The signal noise is measured

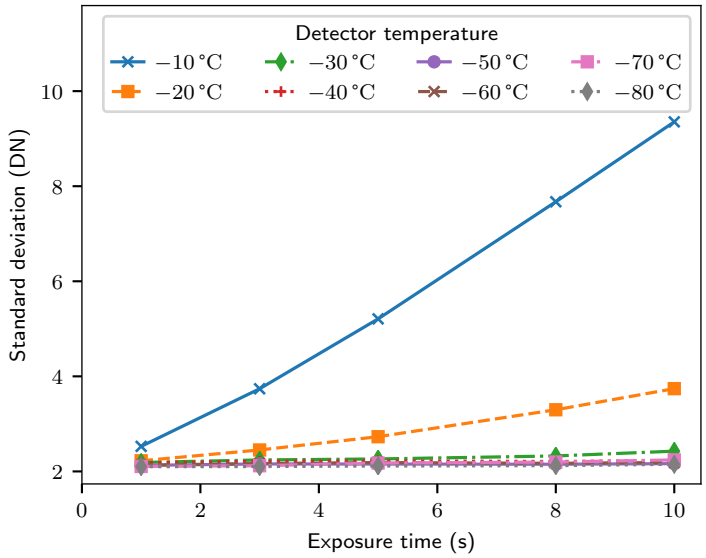

Figure 4.10: Standard deviation of the data shown in Figure 4.9a as a measure of dark noise. The noise appears to increase approximately linearly with the exposure time instead of an expected $\sqrt{t}$ shape. This evaluation does not differentiate between frame-to-frame fluctuations and calibratable signal level differences of neighbouring pixels.

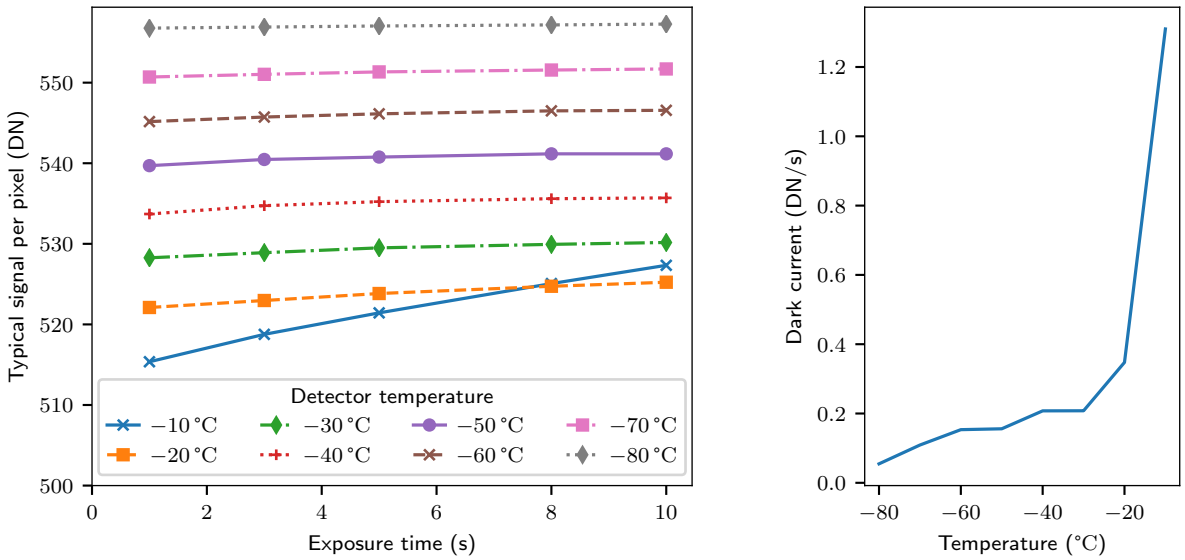

(a) Signal level. **(b)** Dark rate.

Figure 4.11: Dark signal of a typical pixel. The measured signals have been averaged per pixel over the 30 recordings. The median pixel result is used for these figures. The results are based on the same data as those shown in Figure 4.9, but the employed mode of evaluation is less influenced by hot pixels and cosmic rays. (a) Signal levels produced by the dark detector over different exposure times at different temperatures. (b) Dark current as the slope of the signal level determined by linear regression of the curves in (a).

with the standard deviation of the data. It is shown in Figure 4.10. The data suggests a readout noise of 2.1 DN and a dark noise that increases approximately linearly over time.

The presented results are, however, influenced by so-called hot pixels, which show a disproportionate rise of the dark signal over time compared to the other pixels, thus significantly increasing the mean signal level. Furthermore, the calculated standard deviation is increased by the different signal levels of neighbouring pixels, including hot pixels, although such different mean signal levels would be accounted for by the subtraction of a dark frame. Instead, the figure of interest for the signal noise analysis is how much the signal level of a single pixel varies

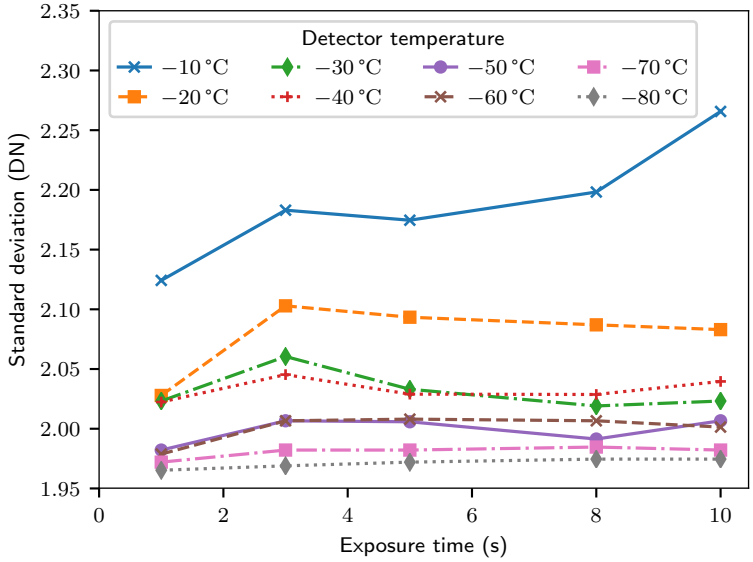

Figure 4.12: Estimate of the typical dark noise per pixel. The standard deviation of the data is calculated per pixel across the 30 recordings. Then, the median of the different pixels is determined and shown per temperature and exposure time.

between multiple acquisitions. Therefore, the same data has been analysed again with the mean and standard deviation per pixel calculated across the 30 recordings. To get the result of a typical pixel with negligible influences of hot pixels and cosmic rays, the median of the means and standard deviations is used. The resulting dark levels and rates are shown in Figure 4.11 and the corresponding noise is depicted in Figure 4.12. For most settings, the typical dark levels are similar to the average dark levels shown before in Figure 4.9a. Only for the temperatures of −10 and −20 °C the dark counts are reduced due to the effective exclusion of hot pixels. For −30 °C and below, the thermal excitation of the hot pixels is already low and hence there is no difference in the outcome of the two methods. The resulting noise estimate is reduced as well because this method separates the actual frame-to-frame signal fluctuation from the pixel-to-pixel variation.

For the shortest investigated exposure time of 1 s, the standard deviation is between 1.96 and 2.03 DN for all temperatures but −10 °C, for which the standard deviation amounts to 2.13 DN. This means that the readout noise is approximately 2.0 DN. Shot noise is proportional to the square root of the signal and thus of the exposure time. Since the shot noise applies to the excitation of photoelectrons on the CCD chip, the gain factor needs to be taken into account in the calculation. According to the specifications of the detector, the gain G is 10 electrons/DN for the employed camera settings. For the example of −40 °C, where a dark count rate r of 0.2 DN/s has been measured, a time-dependent dark noise $n(t)$ of

$$\begin{aligned} n(t) &= \sqrt{G \cdot r \cdot t}/G \\ &= \sqrt{10 \cdot 0.2 \cdot t}/10 \\ &= 0.14 \cdot \sqrt{t} \end{aligned} \tag{4.3}$$

is expected. Surprisingly, despite having approximately the expected square root shape for some of the temperatures, the noise increases slower than predicted by equation (4.3), which is physically not possible. After 10 s the noise level for −40 °C should be at least $(2 + 0.14 \cdot \sqrt{10} = 2.44)$ DN. The determined noise level is, however, only 2.04 DN. This suggests that the gain factor stated in the performance sheet is not correct. However, since for temperatures below −50 °C neither the background level nor the signal fluctuation per pixel increases significantly over time, the detector performance in this regime is likely dominated by readout noise in the order of 2.0 DN. Thus, cooling below this temperature should not be necessary for future studies. A reduction of the pixel clock and line shift rate for the readout procedure did not show a reasonable decrease of the noise level in comparison to the additional time required for readout.

In a typical measurement, multiple pixel rows of the detector will be averaged to convert the image into a spectrum. When averaging the dark signal of the detector rows 100 to 150 and then calculating the standard deviation across the 30 recordings, the resulting noise level decreases to <0.5 DN per spectral channel.

4.3.3 Wavelength calibration

Due to a lack of knowledge about the exact distances and angles between the components of the spectrometer, the geometric calculation of the wavelength scale, which has been presented in section 4.1.2, yields only imprecise results. The outer parts of this calculated wavelength scale deviate by up to 5 nm. Therefore, I compiled a catalogue of pixel-wavelength relationships for different grating angles by identification of various Al and Si emission lines based on their observed and theoretically expected line strength ratios. The data is shown in Figure 4.13. For the investigated reference angles, second order polynomial fits are calculated to interpolate between the data points. For intermediate angles, the wavelengths are then linearly interpolated between the polynomials of the neighbouring reference angles, as shown by the horizontal lines in the figure for some example pixels columns. Limited reproducibility of the grating movement results in minor deviations of the interpolated wavelength scale, typically in the order of 0.5–2.0 nm for different regions in the spectrum. Therefore, the wavelength scale is calibrated at least once per measurement session by fitting some prominent spectral lines and comparing their

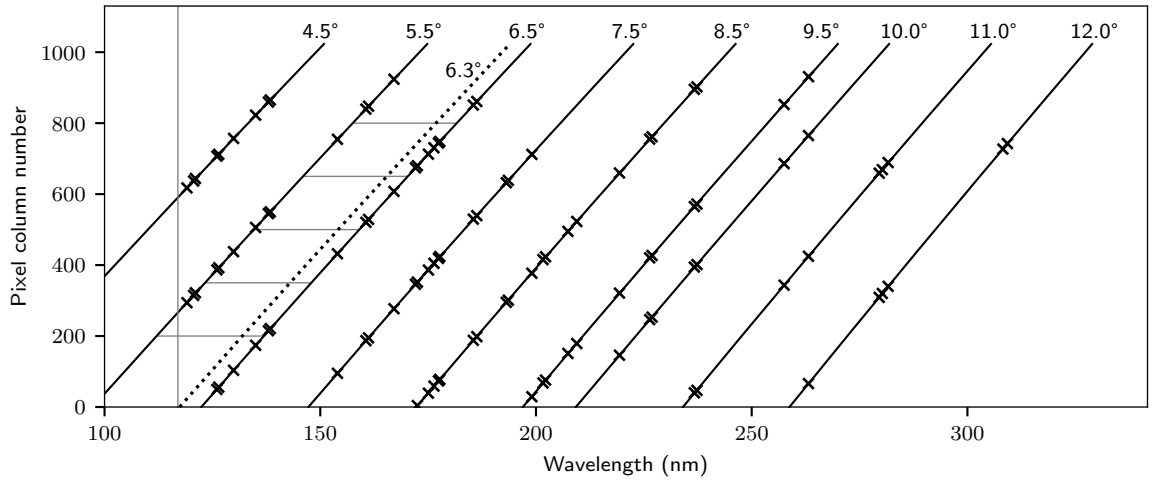

Figure 4.13: Pixel positions of identified Al and Si emission lines for different grating angles from 4.5° to 12.0°. The solid lines are second order polynomials fitted to the data sets per angle. An example interpolation for the frequently used grating angle 6.3° is shown as dashed line. The vertical line at 117 nm indicates the lowest detected wavelength.

measured pixel position to the one predicted from the grating angle. By inversely applying the angle interpolation, an angle offset is derived and the nominal grating angle is corrected to the actual angle. This procedure corrects a shift of the wavelengths scale but not a change in the spread. Due to changes in the set-up and an attempt to better align the diffraction grating, the linear dispersion of the system reflected by the calibration data is slightly off. Accordingly, for optimal calibration results in the spectral region of interest, the reference lines used for calibration should be in the same region. The opposite end of the spectrum may then be up to 0.4 nm off.

4.3.4 Instrumental broadening

The width of detected spectral lines is determined by physical and instrumental broadening mechanisms. For LIBS in vacuum, physical broadening is, in general, expected to be low [19, 96, 97]. However, the detected emission lines appear significantly broadened compared to the theoretical limit of the aberration-free projection of the spectrometer entrance slit onto the detector. Therefore, instrumental broadening likely contributes significantly to the detected line shape. This has been investigated with a fibre-coupled mercury lamp (Hg I, 253.65 nm) as well as with spatially filtered emission of an aluminium plasma (Al II, 167.08 nm).

Characterization with a monochromatic point source

To investigate the instrumental broadening, also known as response function, a fibre-coupled mercury discharge lamp emitting a strong line at 253.65 nm was used. The free end of the 50 µm wide fibre was mounted on an x-y-translation stage in the middle of the vacuum chamber after removing the sample holder. For both the imaging (0^{th} order) and the spectral operating mode of the spectrometer, I found a line width of two pixels FWHM, corresponding to 0.13 nm. This result is in agreement with the theoretical limit of the system, the symmetric projection of the 56 µm wide entrance slit onto the detector with a pixel width of 26 µm. Translating the fibre end laterally and vertically through the sample chamber, however, caused a movement of the spectral line on the detector. The observations are shown in Figure 4.14. Here, the lateral and vertical movement of the fibre end between the images is 1 mm in the respective direction. Comparing the spectral line to the reference marker (thin black line) shows clearly a change in the recorded detector images. The spectra in Figure 4.15, which are extracted from the middle row of images in Figure 4.14, emphasize this observed shift. They have been generated by vertical binning of the detector rows 100 to 150. For a plasma plume spanning several millimetres this means that

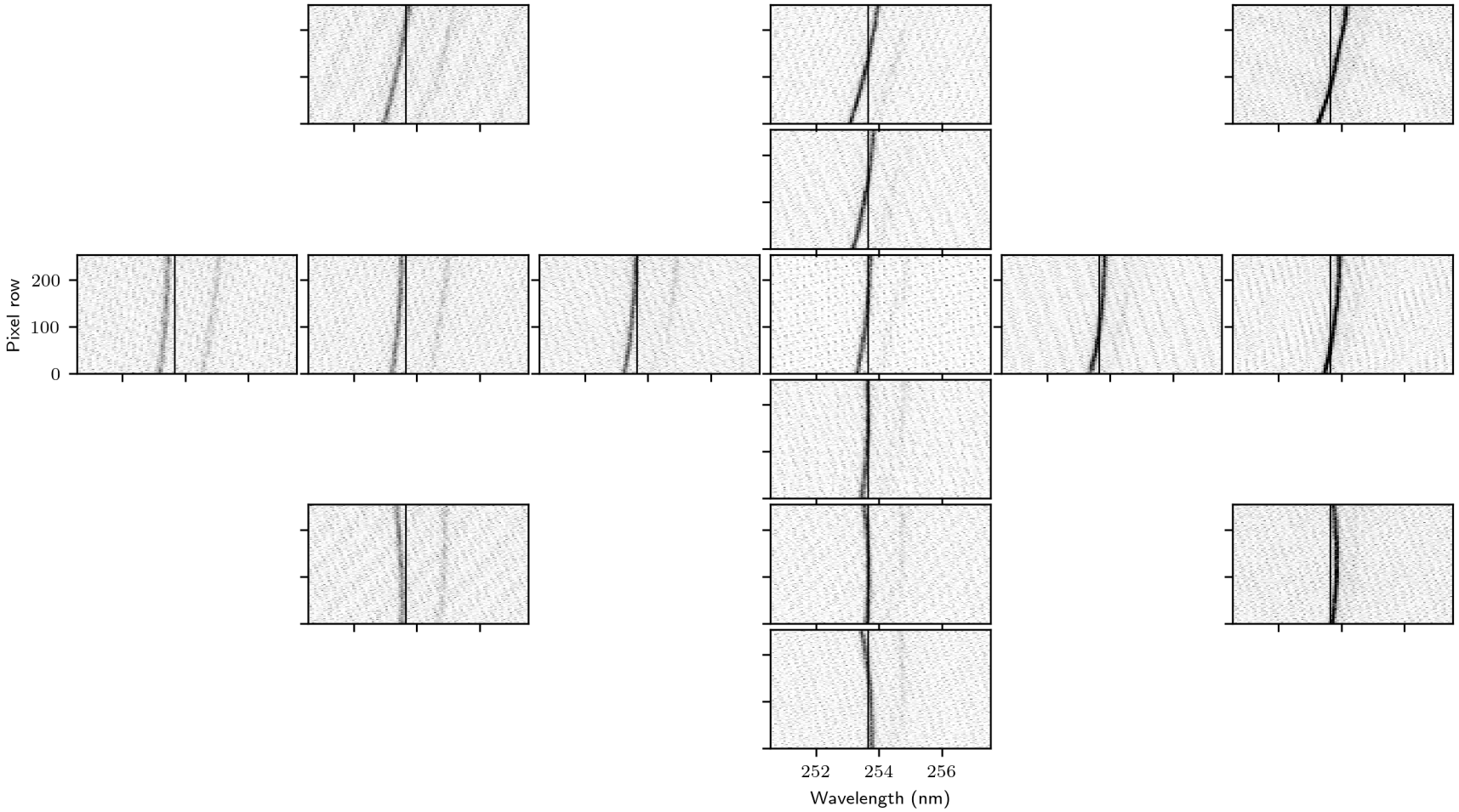

Figure 4.14: Spectra of a fibre coupled-mercury lamp to deduce the instrumental response function. The 50 µm wide fibre is moved laterally and vertically in the sample chamber with neighbouring panels corresponding to a movement of 1 mm in the respective direction. For a plasma with a diameter of approximately 5 mm, these fibre positions reflect the cross-sectional emission of the plasma plume. The vertical black line serves as reference to see the change of the recorded signal. The x- and y-scales apply to all panels, and the colour scale ranges from 0 (white) to 250 and above (black) counts. Since the system is open and filled with ambient air, detector cooling is switched off causing a high noise level.

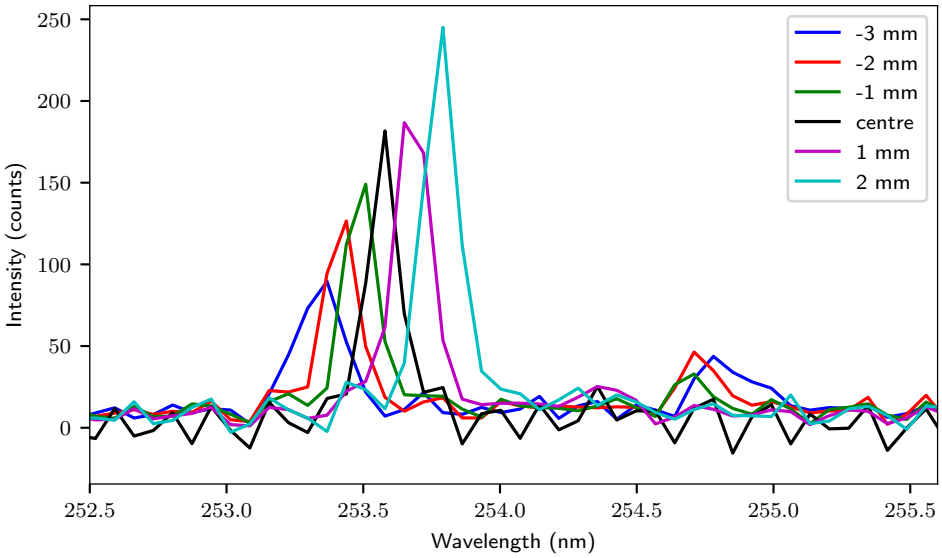

Figure 4.15: Spectra of the Hg I line extracted from the middle row of images in Figure 4.14. The detector rows 100 to 150 have been binned to generate the spectra. The legend gives the lateral position of the light source. During the translation of the fibre over 5 mm, the spectral line moves on the detector, resulting in an apparent spectral shift of 0.44 nm. For the position −3 mm, the *ghost line* at 254.8 nm has approximately half the intensity (area) of the *main line*.

a single spectral line is projected onto multiple positions on the detector at the same time and therefore appears broadened.

Another observation is the tilting of the lines depending on the vertical position of the source. This can to some extent be exploited to deduce the source region of certain emission lines, i.e. if the emission originates from higher outer parts of the plasma or if it is localized in the centre, but is disturbing and undesired in most applications. For a perfect spectrometer, the characteristics of the light field should be decoupled at the entrance slit, and all light passing through the slit with a direction that allows to reach the subsequent optics should arrive at the detector at a well-defined position. Due to optical aberrations inherent in the curved imaging grating this perfect spectrometer case is not quite given and the imaging performance for rays hitting the outer parts of the grating is reduced [92]. When the source is moved laterally, most of the light reaches the slit with a non-zero angle to the optical axis, thus shifting the centre of gravity of the light field to one or the other side of the grating. This leads to a higher fraction of signal suffering aberration and hence moves the lines on the detector. The effect can be intensified if the grating is not properly positioned in the design of the spectrometer. Simulations with Zemax Optical Studio suggest that a displacement of the grating by only 0.5–1.0 mm is sufficient to cause a measurable shift of the detected line positions. These simulations, however, can only give a coarse estimate because neither the radius of curvature nor the exact arrangement of the grating grooves is stated in the description of the spectrometer. Both effects could be further enhanced by the general obliquity of the optical axis due to the slight leaning of the grating. Although a correction of the leaning with shimming has been attempted, a lack of alignment references hampers further improvement at the moment.

The origin of the ghost lines seen in some panels of Figure 4.14 could not be identified. They were discussed with the manufacturer of the spectrometer, who could unfortunately not provide a solution. Although the ghost line in the leftmost panel of the central row of images has approximately half the intensity of the main line in this panel, see Figure 4.15, these ghost lines do not appear in typical LIBS measurements or at least not with significant intensities. Therefore, they are not further investigated.

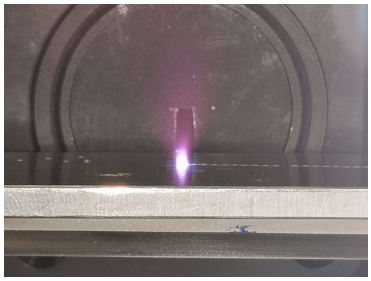

(a) Core. Only the central part is transmitted.

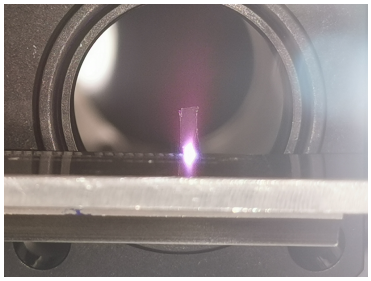

(b) Corona. Only the outer parts are transmitted.

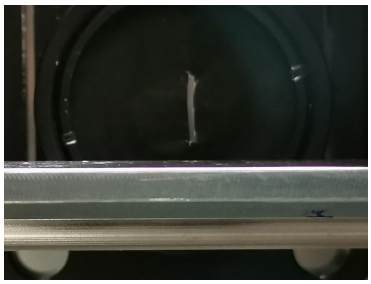

(c) Slit. Only a column above the sample surface is transmitted.

Figure 4.16: Photographs of the different apertures used to investigate geometric broadening. The apertures are placed approx. 1 cm behind the targeted spot on the sample.

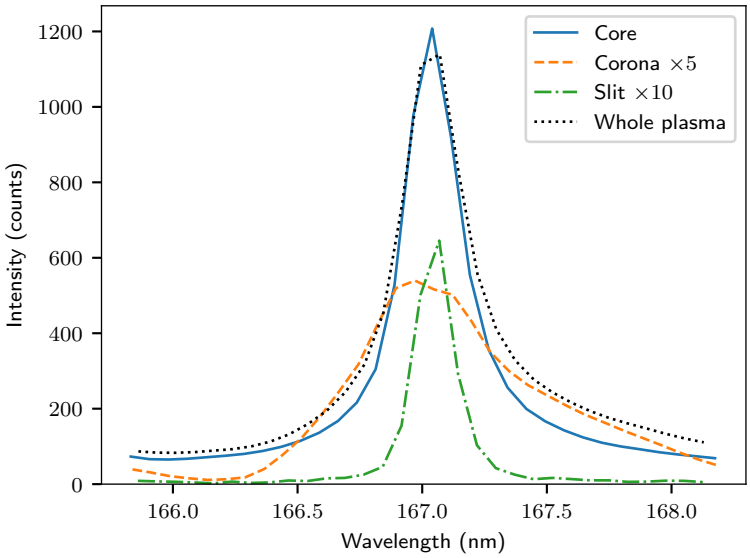

Figure 4.17: LIBS spectra of an aluminium plate recorded with different apertures, see Figure 4.16. The signals *corona* and *slit* are scaled by a factor of five and ten, respectively, to allow for direct comparison of the line shapes. The *whole plasma* spectrum was taken without any aperture. It is roughly comparable to the sum of the *corona* and the *slit* signal. All spectra show the average of 10 measurements recorded with a pulse energy of 32 mJ.

Instrumental response to spatial regions of the plasma

Many LIBS instruments have a limited and well-defined field of view, as it would be the case for this system as well if the OAP was replaced with a mirror of customized shape, properly projecting the plasma plume onto the entrance slit. At the current state, however, light from all regions of the plasma is coupled into the spectrometer but with a lower efficiency, thus causing geometric broadening as predicted from the Hg lamp measurements discussed in the previous part of this section. Since the intensity distribution across the cross-section of the plasma plume is unknown and may be different for the VUV transitions than expected from the visual appearance of the plasma, different apertures have been placed near the sample to study the emission regions separately. These apertures were cut out of black aluminium foil and placed approximately 1 cm behind the plasma, allowing only radiation originating from the plasma centre (*core*), the outer regions (*corona*) or the column above the plasma centre (*slit*) to reach the detector, see Figure 4.16. The distance of 1 cm was chosen in order to minimize any interference effects that the physical barrier of the aperture might have on the plasma expansion [98, 99], but at the same time reliably mask different zones of the plasma.

The spectra acquired with theses apertures are shown in Figure 4.17. Comparing the signal from the core to the signal of the whole plasma, one can see that the line centre has an approx-

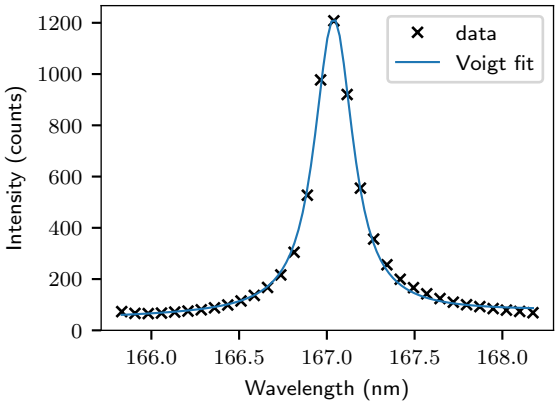

Figure 4.18: Voigt fit to the Al II emission line at 167.08 nm recorded with the *core* aperture. The fit results in a Lorentzian half-width of $\gamma = 0.120$ nm and a Gaussian standard deviation of $\sigma = 0.031$ nm. The Lorentzian-dominated line profile suggests a significant contribution of Stark broadening due to the high electron density in the plasma initiation phase.

imately equal amplitude. The aperture mainly reduces the tails of the line intensity distribution, as expected from the Hg lamp experiments. The remaining core signal is almost symmetric. A Voigt fit to the data is shown in Figure 4.18. It reveals a Lorentzian-dominated shape of 0.262 nm FWHM, with a Lorentzian half-width of $\gamma = 0.120$ nm and a Gaussian standard deviation of $\sigma = 0.031$ nm. This is already less broad than for the unobstructed plasma data (FWHM = 0.308 nm) but still broadened compared to the Hg lamp results. The corona signal, on the other hand, is strongly asymmetric and rather broad with a FWHM of 0.67 nm. Although it is low in intensity and had to be scaled up by a factor of five in order to be clearly visible in Figure 4.17, it suffices to broaden the emission lines of the unobstructed plasma.

The line width not being at the instrumental limit despite using the *core* aperture suggests that physical broadening mechanisms are relevant as well. The Lorentzian shape could be explained by Stark-broadening as a result of high electron densities in the plasma initiation phase. While it is, in general, assumed that spectral lines emitted by vacuum plasmas are less affected by self-absorption [100] and Stark broadening [96] due to the lower density of the plasma species, the lowest investigated pressure in the study by Dreyer et al. [96] is about 140 Pa (1 Torr). For even lower pressures the plasma life time is reduced and Stark-broadened emission from the early plasma due to an initially high electron density can likely dominate the time-integrated signal. Loiseleur et al. [101] found an electron density in the order of $10^{26}\,\mathrm{m}^{-3}$ at the end of the laser pulse for an excitation scheme similar to my experiment. Measurements with a slit aperture placed 2 mm above the sample surface as shown in Figure 4.16c, show an even lower line width, though also with considerably less intensity. The corresponding spectrum in Figure 4.17 is scaled up by a factor of ten to be comparable. Analysis of the line shape results in $\gamma = 0.039$ nm, $\sigma = 0.053$ nm and FWHM = 0.171 nm, which is already close to the instrumental limit of approximately 0.13 nm found with the Hg lamp in the first part of this section. The reduced Lorentzian component supports the interpretation of Stark-broadened emission originating from the plasma centre, which is spatially gated out. Besides the Stark broadening in the plasma core being blocked, the influence of self-absorption is reduced as well because the plasma centre is also the part with the highest atom density.

Despite the resolution enhancing potential of apertures close to the sample, most experiments have been conducted without an aperture. This is mainly because the apertures were mounted on posts and placed in the chamber without any fixation. If the aperture then moves between the measurements of a series, the results would no longer be comparable. Especially for the slit placed above the sample surface, variations in the sample thickness would inconsistently mask the most intense part of the plasma plume and might introduce severe systematic errors. Therefore, most of the spectra analysed in this work will show asymmetric lines with widths in the order of

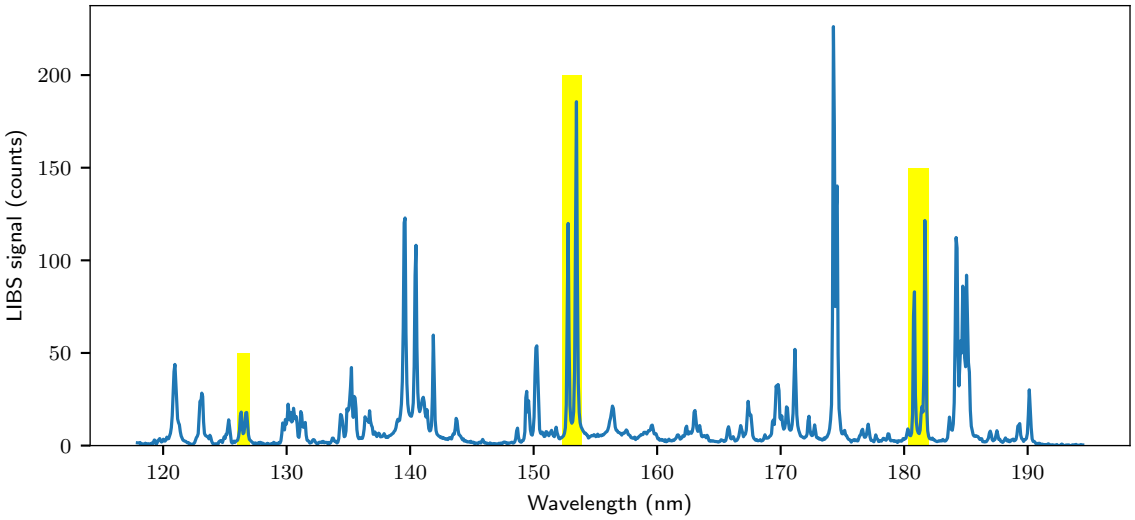

Figure 4.19: Average of ten LIBS spectra of a Si wafer recorded with 40 mJ laser pulse energy in a 6 hPa N_2 atmosphere. The emission lines shaded in yellow are used for the sensitivity estimate. For these measurements, a slit aperture as shown in Figure 4.16c and explained in section 4.3.4 was used to enhance the resolution.

0.31 nm FWHM.

4.3.5 Relative sensitivity estimates

In the deep-UV and vacuum-UV wavelength range, the sensitivity of an instrumental set-up can vary strongly across the detected spectrum. It is influenced not only by the quantum efficiency of the detector, which in my case has been provided by the manufacturer, but also by the choice of materials used for the optical components and possibly by residual atmosphere. To determine the sensitivity, one would usually use a calibrated light source and compare the detected signal to the calibration data. Ideally, this would result in a number of detector counts per photon introduced into the set-up or emitted by the plasma. Most of these calibration lamps are, however, coupled to optical fibres or the radiation is produced inside a bulb of quartz glass, both of which do not transmit wavelengths below 170 nm [69]. For the VUV, special versions of deuterium lamps with a VUV-transparent MgF_2 window are available. Unfortunately, there was no opportunity to use such a lamp during the time of my thesis. As an alternative, I estimated the spectral response by comparison of measured spectra of a Si wafer to simulated LIBS spectra of Si. For the simulations, I used a tool that was developed in our group and is based on the approach described in section 2.1.3. However, as mentioned in section 2.1.2, the LTE required for the simulations to be applicable is in general not present in the inhomogeneous and highly dynamic vacuum plasma [49]. Therefore, the measurements for this investigation are conducted in a 6 hPa N_2 atmosphere. This still does not ensure LTE conditions but makes them more likely for some phases of the plasma life time. Finally, the temporal decay behaviour of the temperature describing the plasma captured with the time-integrated detection scheme needs to be reflected in the simulations. As a first approximation, this is achieved by summing simulated spectra with equilibrium temperatures linearly decreasing from a start value T_{init} to 300 K. The intensity ratios of suitable lines within the simulated spectrum are then compared to the intensity ratios measured with the instrument.

Identification of suitable lines

Since the theoretical assumption of LTE made for the spectrum simulations has limited validity, in general and especially for spatially and temporally integrated measurements, the quality of the sensitivity calibration depends strongly on the selected emission lines and the simulation parameters. Suitable emission lines should span a large portion of the spectral range, be fairly

λ/nm	E_u/eV	E_l/eV	g_u	g_l	A_{ul}/s^{-1}
126.042	9.84	0.00	4	2	2.57×10^9
126.473	9.84	0.04	6	4	3.04×10^9
126.501	9.84	0.04	4	4	4.73×10^8
152.671	8.12	0.00	2	2	3.81×10^8
153.344	8.12	0.04	2	4	7.52×10^8
180.801	6.86	0.00	4	2	2.54×10^6
181.692	6.86	0.04	6	4	2.65×10^6
181.745	6.86	0.04	4	4	3.23×10^5

Table 4.2: Spectroscopic constants of the Si II lines used for the sensitivity estimate [52]. λ: wavelength; E_u and E_l: energy of upper and lower level; g_u and g_l: degeneracy of upper and lower level; A_{ul}: Einstein coefficient for spontaneous emission.

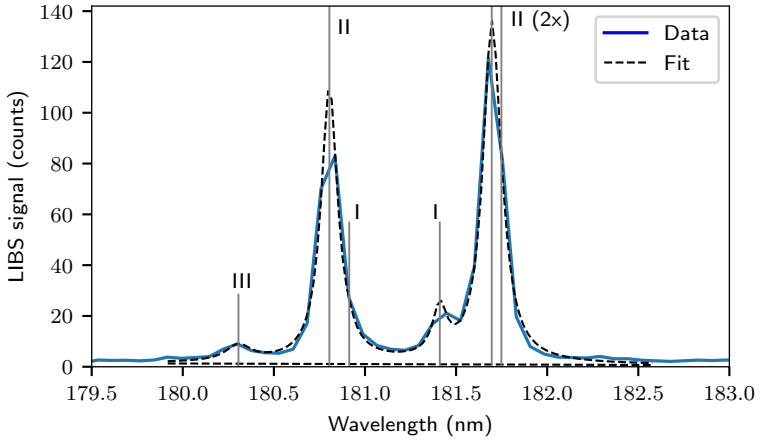

Figure 4.20: Simultaneous fit to Si I, II and III lines to derive a suitable start temperature for the simulation of intensity reference spectra. The data has been recorded on a Si wafer with a laser pulse energy of 40 mJ.

isolated and strong in the recorded spectra, and show a similar temperature behaviour of their emission intensity. For the latter, this means that emission lines from the same ionization stage and with similar energy levels should be considered. Ideally, the considered transitions would share the same upper energy level. Then, the emission intensity ratios between the lines would be entirely decoupled from the temperature and solely depend on the Einstein coefficients with some deviations due to self-absorption. Unfortunately, such series of emission lines are rarely available while at the same time all being in the range of detection and of significant intensity.

The LIBS spectrum of a Si wafer acquired with 40 mJ pulse energy, on which the sensitivity calibration will be based, is shown in Figure 4.19. In the detected range, the above requirements are only met by three Si II multiplets located at 126, 152 and 181 nm, shaded yellow in Figure 4.19. The spectroscopic constants for these lines extracted from the NIST Atomic Spectra Database [52] are summarized in Table 4.2. Involving the ground state or a level nearby the ground state, these lines are likely influenced by self-absorption [41], which may result in an inaccurate assessment of the line strength.

Si I transitions would be expected to be more stable in their intensity ratios when disregarding self-absorption, but are too weak in the spectra. Si III has a ground state transition at around 130 nm, while all other Si III transitions in the observed spectral range are related to upper levels of 20 eV and above. From Si IV only one pair of lines at 140 nm is frequently detected.

Line λ/nm	relative intensity 21 300 K	25 000 K	27 700 K
126.042 126.473 126.501	73	110	139
152.671 153.344	37	42	48
181.692 181.745	1	1	1

Table 4.3: Emission line intensities predicted for three different plasma temperatures. The intensities are given as the sum of the indicated groups relative to the doublet at 181.7 nm. The Si II emission line at 180.801 nm listed before was not used for the final results, because of interference with Si I emission.

Simulation results

The input plasma parameters for the simulation algorithm are the initial electron temperature T_{init}, the electron density n_e and the area particle density n_A, which is the product of the particle number density and the length of the line-of-sight through the plasma. I will use an average value of $1 \times 10^{23}\,\text{m}^{-3}$ for n_e, because the instrumental resolution is too low and not known well enough to infer n_e from line broadening, as it is common practice in LIBS studies in the visible wavelength range [102]. Besides these experimental limits, there is limited data on the Stark broadening parameters for the Si lines used here. The n_A being the main parameter for the incorporation of self-absorption has a strong influence on the predicted line strengths. Since it can only be deduced from calibrated line intensities or by the shape of the spectral lines after a correction for instrumental and Stark broadening, both of which are not sufficiently available, I will again use a typical value of $5 \times 10^{19}\,\text{m}^{-2}$ found in other unpublished projects by our research group. Accordingly, the parameter left to adjust for the simulation, which also shows the strongest influence on the intensity ratios of the simulated emission lines, is the electron temperature. To estimate an appropriate temperature, a model of six Lorentzian lines has been fitted to a set of Si I, Si II and Si III emission lines between 180 and 182 nm of the data shown in Figure 4.19. The spectral region of interest together with the calculated fit is shown in Figure 4.20. In this narrow spectral range of only 2 nm width, the sensitivity of the system is assumed to be constant. This allows to compare the line intensity ratios of the three ionization states between simulation and measurement. In a trial-and-error approach, I found the Si I/Si II ratio best described with a temperature of 21 300 K, while the Si III/Si II ratio on the other hand suggests a temperature of 27 700 K. Since the parameter in question is the initial temperature but the signal is time-integrated, estimating the temperature from Saha-Boltzmann plots [102], as it is common practice in the LIBS community, is not feasible in this case. Therefore, I use the values found by testing as well as 25 000 K as a compromise between both of them for the sensitivity estimate. The relative intensities predicted by the simulation are listed in Table 4.3. Comparing these predicted relative intensities to the intensities of the yellow-shaded emission lines in Figure 4.19, one can quickly see that the sensitivity is drastically decreased towards the shorter wavelengths.

Referencing simulation and measurement

For a quantitative analysis, the detected emission line intensities are extracted by fitting Lorentzian line profiles to the data, see Figure 4.21. To increase the resolution, the spectra have been acquired using a slit aperture close to the plasma like the one shown in Figure 4.16c. For details about the effect of apertures see section 4.3.4. The measured intensities are then divided by the predicted intensities. The results are presented in Table 4.4 and visualized in Figure 4.22. De-

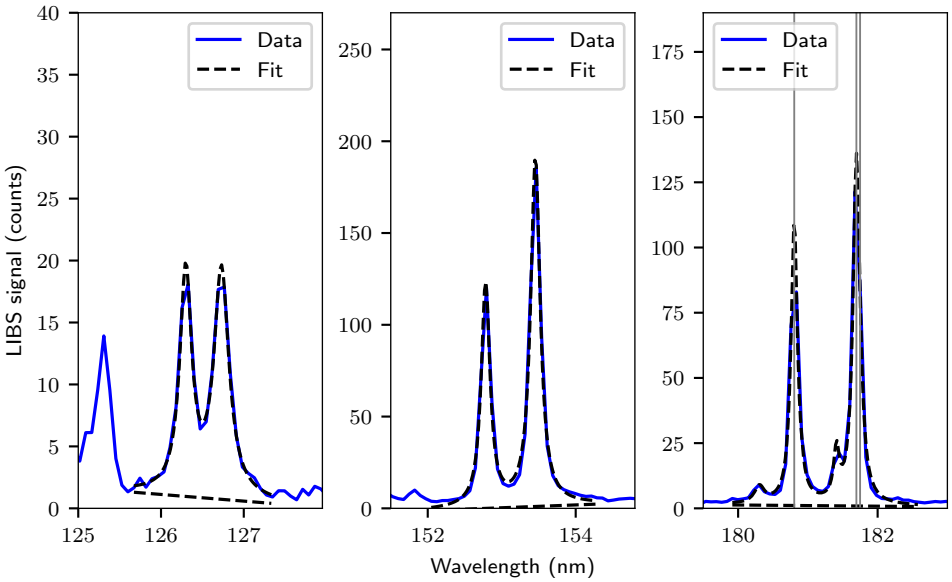

Figure 4.21: Lorentzian fits to the average spectrum taken at 40 mJ from the Si wafer. The vertical lines in the right panel indicate the positions of the relevant Si II emission lines. Due to interference with Si I, see Figure 4.20, the left line at 180.801 nm is not used for the sensitivity calibration.

	relative sensitivity in %		
λ/nm	21 300 K	25 000 K	27 700 K
126	0.28	0.19	0.15
153	3.06	2.68	2.37
181	100	100	100

Table 4.4: Relative sensitivity derived for the three spectral positions 126, 153 and 181 nm. Since the mirror coating is expected to cause most of the losses and to have the highest reflectance at long wavelengths, the sensitivity at 181 nm is used as reference and set to 1.

pending on the initial temperature used for calibration, the derived sensitivities differ by a factor of 1.5 between the lowest and the highest value calculated for 126 nm. Nonetheless, in all three cases the sensitivity at 126 nm is more than two orders of magnitude lower than at 181 nm. These results further suggest that the OAP coupling the plasma emission into the spectrometer has a cut-off wavelength between 153 and 181 nm. Since the UV-enhanced aluminium mirror coating is nominally designed for the range >250 nm, this is not particularly surprising. Still, such a low sensitivity towards the shorter wavelengths is not obvious, because, as one will see in the following chapters, the O I triplet at 130 nm is one of the most prominent signals in LIBS spectra of geological samples. Also the Si IV doublet at 140 nm is often seen in Si spectra in vacuum and exhibits high signal levels for the higher laser pulse energies. The lowest transitions observed so far for different samples are located around 120 nm and are attributed to Si II, Si III, H, Cl I and S III. The Lyman-α transition of H, which could be a very sensitive marker for hydration and adsorbed water, is strongly suppressed by the reduced sensitivity of the current set-up, but may otherwise be worth further investigation with optimized components. Future measurements may produce intermediate data points in the sensitivity characterization, e.g. from Al II and Al III lines.

Finally, it should be noted that the detector was only cooled to −50 °C for these measurements because the employed N_2 atmosphere had approximately room temperature and therefore counteracted the cooling. As I will show in section 7.4, the sensitivity of the set-up for wavelengths below approximately 150 nm is additionally reduced due to a thin ice layer forming on the detector over time, whose growth rate and thickness likely depend on the detector temperature. Accordingly, at the temperatures of −80 and −60 °C, as they are used for the measurements in

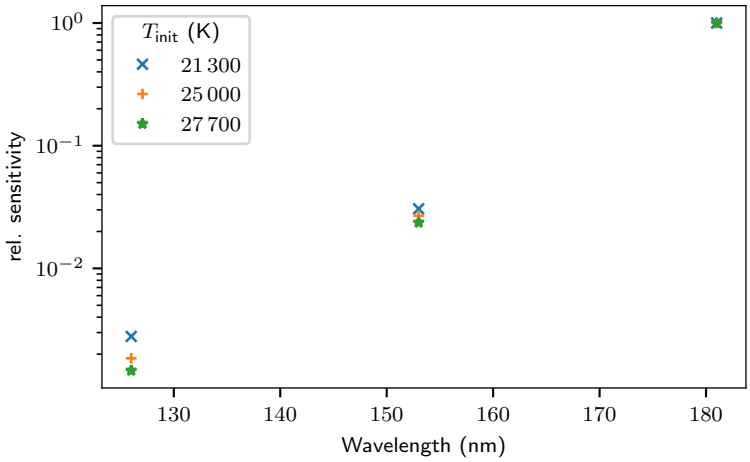

Figure 4.22: Relative sensitivity derived by comparison of measured intensity ratios to the ones from simulated spectra with different initial temperatures. The signal at the short wavelength end of the spectral range is reduced by more than two orders of magnitude.

chapters 5, 6 and 7, the relative sensitivity at 126 and 153 nm may be even lower.

4.4 Measurement routine and data processing

In this section, I will describe the typical measurement and data processing procedure. Except for the dark signal subtraction, which is part of the camera software provided with the spectrometer, all data processing was realized with Python scripts, which I developed myself, using the scientific computing and plotting packages numpy, matplotlib [103] and scipy [104].

After cooling the CCD detector to the desired temperature at the beginning of every measurement session, a dark frame is recorded. For the dark frame, a CCD image is captured with the same detector settings as for the later measurements but without firing the laser. Due to the long exposure times of 8–10 s, cosmic rays are frequently detected. To avoid artefacts in the dark corrected spectra, the dark frame is recorded again, if a cosmic ray was observed. Unless there was a reason to assume a significant change in the dark signal, the same dark frame is used for the rest of the session. After longer breaks or if the cooling of the detector was paused since the last measurement, a new dark frame is recorded. The dark frame is then automatically subtracted from the subsequent recordings. For a typical LIBS measurement, the emission of 25 laser-induced plasma plumes excited at the same location on the sample is integrated on the CCD chip. The sample is then moved by approximately. 1 mm to record the next spectrum.

An example of a dark-corrected CCD recording for a plasma formed on an aluminium plate is shown in the upper panel of Figure 4.23. The spectral lines are oriented vertically and usually span multiple columns. They often appear tilted, as can be seen in the figure, and some of the lines also show a slight bend. Both effects originate from optical aberration and are discussed in detail in section 4.3.4. The leftmost column in this recording corresponds to 117 nm, the rightmost corresponds to 194 nm. Potentially captured cosmic rays in the recorded spectra are identified by comparing the signal differences of neighbouring pixels to the maximum pixel value of the image, to the standard deviation along the pixel column and to a fixed threshold value. If necessary, the perturbation of detected cosmic rays can be reduced by replacing the extraordinarily high signal value with an average value of the neighbouring pixels in the same column. As a next step, the image is rotated by up to $\pm 1.5°$ to correct for the tilted spectral lines. The correct rotation angle is deduced from one representative image of the measurement session and is then applied to all other images. For different sample types, individual rotation angles are determined since the appropriate angle depends on the emission characteristics and spatial distribution of the signal source, as discussed in section 4.3.4. After rotation of the

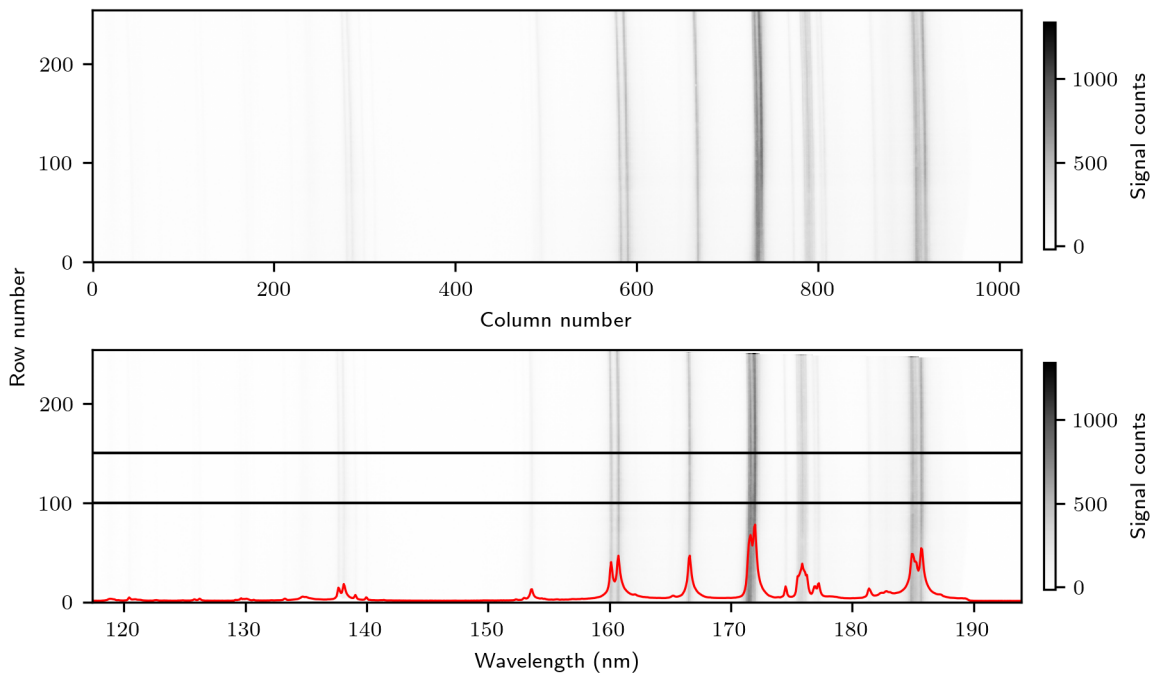

Figure 4.23: Dark-corrected CCD image recorded from an aluminium plate plasma. The spectral lines are oriented along the pixel columns. Aberrations and imperfect alignment cause a rotation and in some cases also bending of the lines. *Top:* raw data. *Bottom:* extraction of line-plots from the rotated and wavelength scaled image. The line-plot is shown in red; the black markers at detector rows 100 and 150 indicate the range used for line-plot extraction.

image, a range of rows is selected and averaged along the columns, thus generating uncalibrated spectra, which can be wavelength calibrated as described in section 4.3.3. Typically, the rows 50 to 200 are selected, because the bending of the spectral lines is negligible in this region of the recorded image. In the case of heavily bent lines, the number of rows used for averaging may be reduced to maintain a certain resolution. This comes, however, at the cost of higher noise levels in the resulting spectra. The bottom panel of Figure 4.23 shows the same recording rotated clockwise by 1°, together with the line spectrum (red) deduced from the detector rows 100–150, as indicated by the black horizontal lines. In this graphic, the wavelength scale has already been applied. From the generated spectra, signal intensities can be derived using fit models of different shapes or summing across a set of spectral channels. Owing to the rather low resolution of the spectra, especially in the earlier measurements, many emission lines suffer from interference with neighbouring lines. Hence, for most of the cases I applied fit models of multiple Gaussian, Lorentzian or Voigt-shaped line profiles. The exact procedure will be described in the respective study.

4.5 Summary

A VUV-LIBS set-up has been developed around a commercial spectrometer and subsequently characterized. The design was driven by four major requirements, which have been identified in measurements with a preliminary vacuum chamber. These requirements were 1) a working pressure below 10^{-2} Pa to be representative for celestial bodies without atmosphere, 2) a load lock capability to facilitate sample exchange while the spectrometer is evacuated, 3) a sample translation mechanism to allow probing multiple locations per sample, and 4) relay optics to collect the plasma radiation and couple it into the spectrometer. In this first iteration of a VUV-LIBS set-up, all four requirements could be resolved with commercial off-the-shelf components.

Characterization of the system showed that the detector dark signal is dominated by readout noise, while the dark current and thus the shot noise of the dark current are negligible for detector

temperatures $\leq -50\,^{\circ}\mathrm{C}$ and exposure times up to 10 s. Lacking the opportunity to use a VUV calibration source during the time of this project, I estimated the spectral sensitivity by comparing emission line intensity ratios for selected Si II emission lines at 126, 152 and 181 nm detected in a 6 hPa N_2 atmosphere to line ratios simulated on the basis of local thermodynamic equilibrium. The results of this sensitivity estimate depend strongly on the simulation parameters and differ by a factor of 1.5 between the lowest and the highest derived relative sensitivity at 126 nm. Nonetheless, the analysis of the relative sensitivity shows independently of the simulation parameters that the sensitivity at the shortest investigated wavelength of 126 nm is about two orders of magnitude lower than the sensitivity at 181 nm. Most of the signal losses are likely caused by the off-axis parabolic mirror, which couples the plasma radiation into the spectrometer, because its reflective coating is not optimized and also not specified for wavelengths below 250 nm. Furthermore, the relevant broadening mechanisms were investigated and were found to be dominated by instrumental and Stark broadening. Measurements with a fibre-coupled Hg discharge lamp as a monochromatic point source yielded a line width of 0.13 nm FWHM, which corresponds to the theoretical limit determined by the width of the spectrometer's entrance slit. The measurements further revealed that the position of the spectral line on the detector changed when moving the fibre end laterally and vertically by up to 2 mm in each direction. This means that emission from a plasma with a diameter in the order of 5 mm will be detected as a superposition of multiple shifted spectra, leading to an apparent line broadening. This was further investigated with apertures close to an Al plasma, which only allow radiation from the central part, the outer part, or a vertical slice above the central part to reach the detector. The results show a significant contribution of the outer regions of the plasma to the total line width. Furthermore, the high electron density during the plasma initiation phase has been found to cause considerable Stark broadening, which also has a strong impact on the line width due to the short plasma life time. When only detecting the slice above the plasma centre by using a slit aperture, which is placed above the sample surface, this early high-electron density phase can be spatially gated out and line widths of 0.16 nm FWHM can be achieved, which are close to the instrumental limit.

Chapter 5

Line identification from pure samples

There are far less LIBS studies reported for the VUV range than for the commonly used UV, visible and NIR spectral range, presumably mostly due to the experimental challenges inherent in this spectral range. Existing VUV-LIBS publications were often found to be unsuitable as a reference for how a potential VUV-LIBS space instrument could perform. Their respective measurements have either been conducted in an argon or nitrogen purge atmosphere [105], which considerably changes the plasma development and dynamics compared to LIBS in vacuum [11, 21], or they employed high laser pulse energies [106] that are not feasible for a power-constrained space instrument. Sometimes, purge atmosphere and high pulse energies are further combined with multi-pulse configurations [107], thereby strongly influencing the excitation state of the plasma. Prediction of spectral line intensities based on LTE, see section 2.1.3 for details, which is as well inadequate for vacuum conditions but could provide some guidance towards expected emission intensity ratios, is also not always possible because fundamental spectroscopic constants such as Einstein coefficients are not available for all transitions in the atomic spectral data bases by NIST [52] and Kurucz and Bell [53].

As a consequence, I conducted a first study on samples containing only a single element, such as pure metals, and on other chemically simple substances like different carbonates and sulfates, in order to assign detected spectral lines to the elements and to establish a catalogue suitable for our experimental conditions. Different laser pulse energies have been tested for each sample because the laser coupling and the analytical quality of the resulting plasma differed between the samples. Due to the limited size of the samples, often only four or five spectra could be acquired per setting. The spectra shown in the first two sections for line identification are the averages of all measurements with the chosen set of experimental parameters.

In section 5.3, the dependence of the emission intensity on the laser pulse energy is investigated for emission lines of different ionization states. The observed dependence may in some cases assist line identification because ions of a higher degree might not show up for lower laser energies and also show different trends for an increase in laser pulse energy than do neutral and singly ionized species. The last section of this chapter gives an overview of the detected lines of the elements Al, C, Ca, Cl, Cu, Fe, H, K, Mn, Na, Ni, O, P, S, Si, Ti and Zn. For Mg, no lines have been identified.

5.1 Pure metal spectra

Metals typically emit many closely-spaced emission lines in the UV spectral range, which complicate the detection of other elements in the same spectral range, e.g. as the C I emission line at 247.9 nm is interfering with Fe II emission [62, 108]. In the form of oxides, especially from Al and Fe, but also from Ti, metals occur frequently in geological samples and are therefore relevant to the application of VUV-LIBS in planetology. To identify their emission lines, six sputtering targets of Al, Cu, Fe, Ni, Ti and Zn have been studied as metal samples of high purity in the range of 99.60–99.99 %. Additionally, a Si wafer has been probed. Although Si is not a metal, its

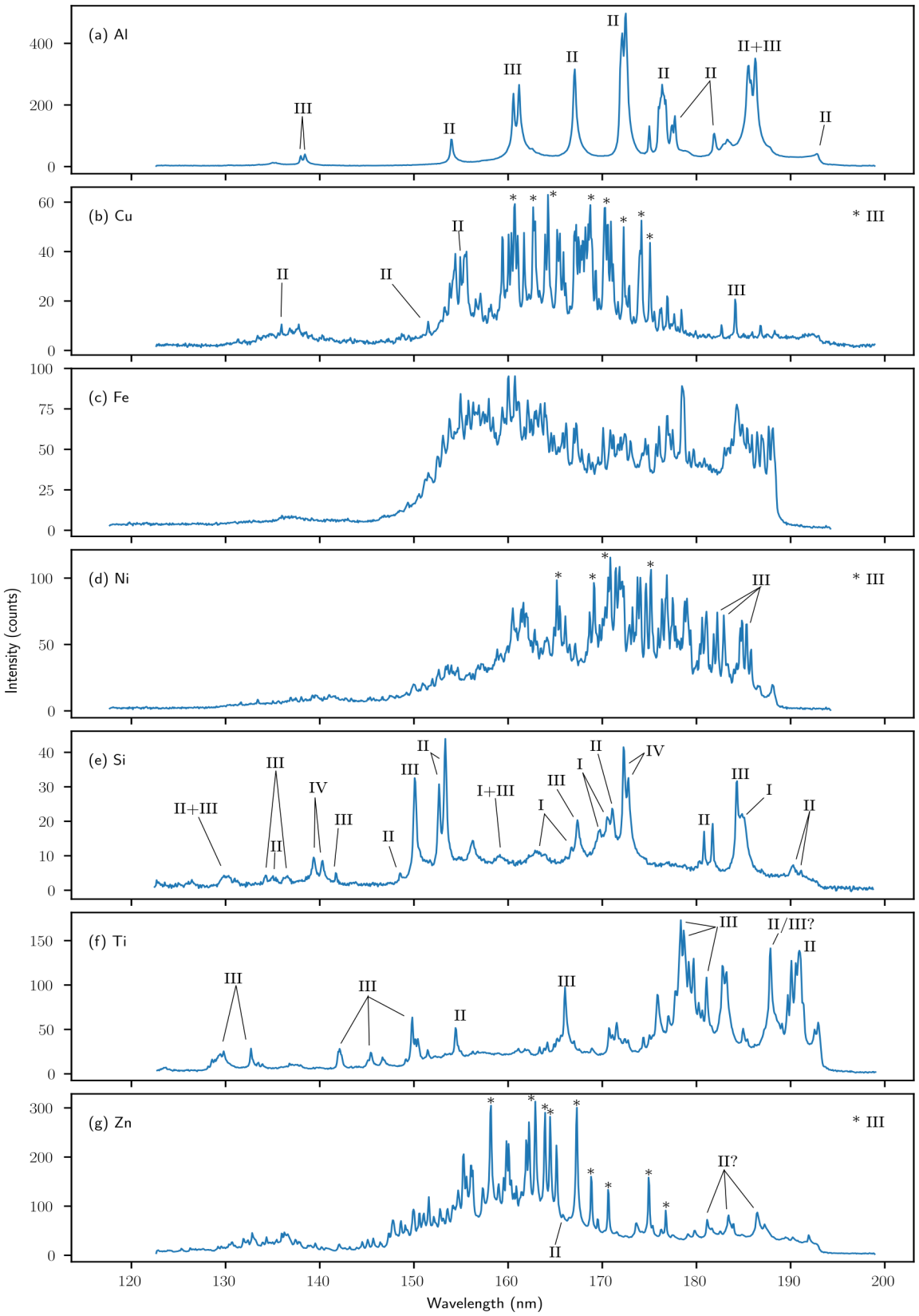

Figure 5.1: Spectra of pure metal samples. Labels I, II and III indicate neutral, and singly and doubly ionized species of the respective metal in the sample. For readability, some Cu III, Ni III and Zn III lines have been asterisked (*). Uncertain assignments, e.g. due to a mismatch to the reference positions in the data bases, are indicated with a question mark (?). They only appear in the spectra of the particular sample and are therefore likely from the respective element or from an impurity of an element not studied here.

spectrum is included in this section due to the mono-elemental and hard character of the wafer as opposed to the brittle pellet samples presented in section 5.2.

Figure 5.1 shows spectra of these samples recorded with a pulse energy of 19 mJ for the sputtering targets and of 25 mJ for the Si wafer. Like in the common UV range, the transition metals Cu, Fe, Ni and Zn emit very dense series of spectral lines that can partially not be resolved with the present set-up. Below 150 nm, however, emission of these elements ceases and other elements having emission lines at shorter wavelengths could easily be detected. Due to the distribution of energy on many transitions, the intensity of single lines is limited and strong emission lines of other elements could still be identified despite spectral interference. All identified Fe emission lines originate from Fe II, while the spectra for Cu, Ni and Zn are dominated by doubly ionized species. Ti is also a transition metal but shows considerably less dense emission lines compared to the aforementioned metals, see Figure 5.1(f). The identified Ti II and Ti III lines spread across the whole detection range of 125–195 nm.

For Al, an element highly abundant in many geologic samples, very strong Al II emission lines have been identified at 167.1 nm and at 172.1 and 172.5 nm, Figure 5.1(a). Another group of six Al II emission lines around 176.4 nm, which are not entirely resolved, appears to be a characteristic marker because of its pattern: an enhanced line peaking out of the middle of an almost 1 nm wide plateau. The Al III doublets at 138 and 161 nm are also high in intensity. They appear, however, weak because of the decreasing sensitivity of the set-up towards shorter wavelengths.

Si, making up almost 30 wt.-% of the Earth's crust [109], is present in many geologic samples, also beyond Earth in samples from the Moon [110] or Mars [111]. In the spectrum of the Si wafer, Figure 5.1(e), emission lines from neutral to triply ionized species can be identified. The ratio between them depends strongly on the employed laser pulse energy, as will be discussed in section 5.3. The most dominant emission lines are of Si II at 152.7 and 153.3 nm, and Si III at 150.1 nm. Two Si IV lines at 139.4 and 140.3 nm are also detected in many spectra despite the low sensitivity of the system in this spectral range.

5.2 Sulfur and different salts

Besides pure metal samples, multiple salts have been studied in order to identify emission lines of the alkali and alkaline earth metals Na, Ca and Mg, which are major rock forming elements, but also of C, Cl, P and S from the anionic part of the salts. The latter are challenging to detect and to quantify with LIBS in the conventional UV to NIR range and hence, VUV-LIBS is expected to be especially advantageous for those elements. A sample of pure sulfur powder has been prepared and studied as well. For these pellet samples pressed from the respective powder, the laser coupling is very different compared to the metal samples. For many spectra shown here, a laser pulse energy of 25 or 32 mJ was required to excite analytically useful plasma plumes in the low-pressure environment.

5.2.1 Sulfur-bearing samples

Spectra of pure sulfur, $MgSO_4 \cdot 7\,H_2O$, Na_2SO_4, K_2SO_4 and a mixture of CaF_2 and gypsum ($CaSO_4 \cdot 2\,H_2O$) are shown in Figure 5.2. In order to enhance the visibility of low intensity emission lines without the distortion and apparent noise inherent in a logarithmic scaling, the y-axis has been segmented in two linear parts with different spreads for many of the spectra. A horizontal line indicates the level where the scaling changes. This mode of presentation introduces sharp bents on the edges of the peaks that reach into the upper part of the graph, but in exchange allows to see both strong and weak emission lines at the same time and to get an impression of the signal-to-noise ratio for the weaker emission features.

As mentioned above, different laser pulse energies had to be used for these measurements due to different laser coupling with the sample. The pure sulfur pellet already produced useful

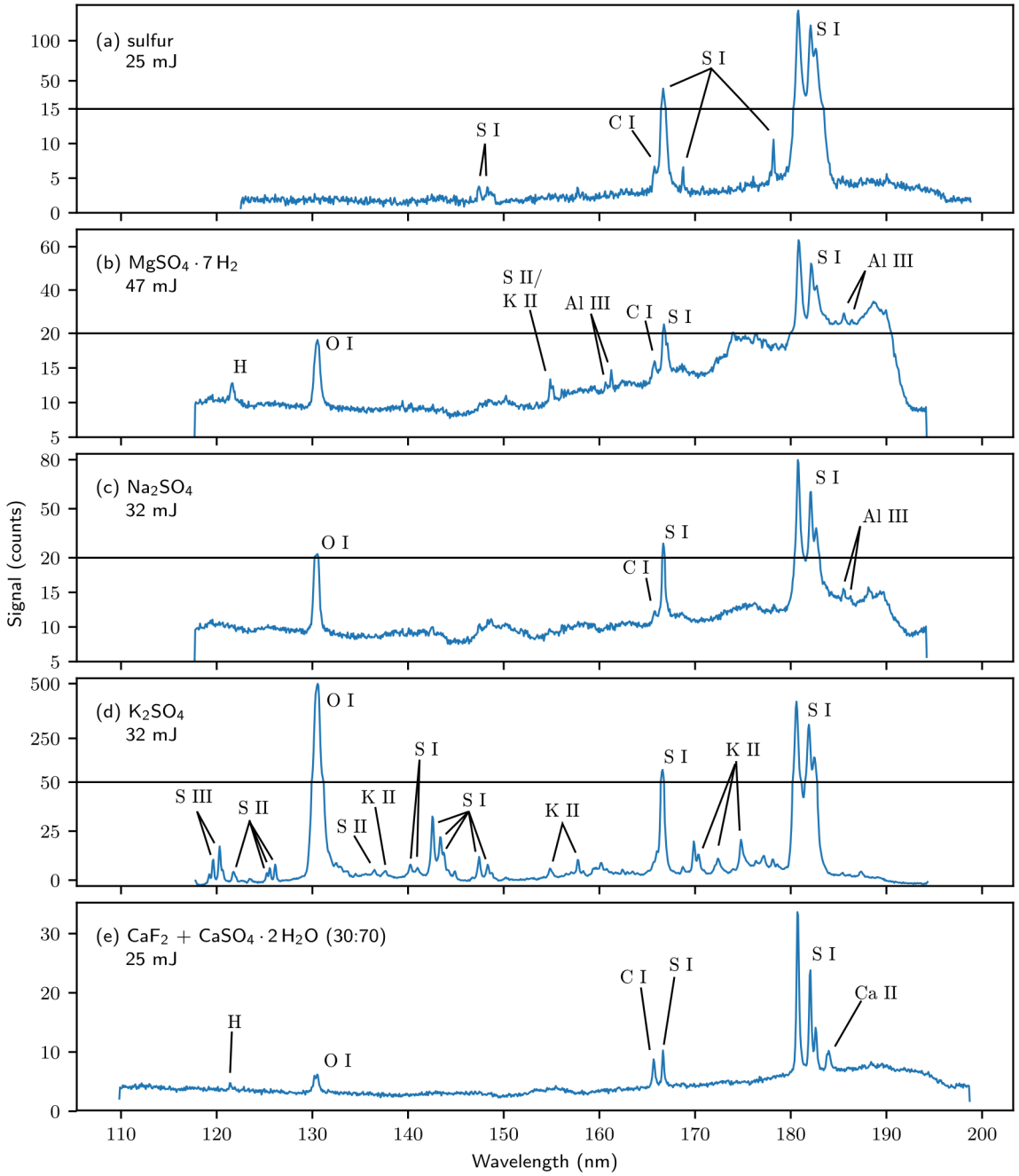

Figure 5.2: Spectra of (a) S, (b) $MgSO_4 \cdot 7\,H_2O$, (c) Na_2SO_4, (d) K_2SO_4 and (e) a 30:70 mixture by weight of CaF_2 and $CaSO_4 \cdot 2\,H_2O$. The employed pulse energies are given in the respective panel. The four strong S I emission lines seen in the spectrum of pure sulfur at 166.7, 180.7, 182.0 and 182.6 nm are clearly visible in the sulfates as well. To increase the visibility of low intensity emission lines, the y-scale in the panels a, b, c and d is split in two linear parts with different spreads. The black horizontal lines mark the transitions between the segments.

spectra at a moderate pulse energy of 25 mJ, while for the hydrated $MgSO_4$ sample the pulse energy had to be almost doubled to obtain spectra of a comparable quality. A similarly weak coupling has been observed for gypsum, suggesting that the hydration state might be a parameter of influence. Still, the gypsum sample was probed with 25 mJ for the spectrum shown here, which explains why the S I lines are much weaker than in the other spectra. Furthermore, for CaF_2 + gypsum, spectra recorded at two different grating angles have been concatenated, leading to the larger spectral range compared to the other spectra.

In all spectra shown in Figure 5.2, four prominent S I emission lines at 166.7, 180.7, 182.0 and 182.6 nm can be observed. Two more S I emission lines of lower intensity are visible at 168.8 and 178.2 nm in the spectrum of pure sulfur, together with a very weak hint of the S I lines at 147.4 and around 148.5 nm. Due to the high pulse energy used for $MgSO_4$, the spectrum in Figure 5.2b also shows one line at 154.9 nm, which has been attributed to S II. The bump on the short wavelength side of the 166.7 nm emission line could potentially be attributed to a S II transition as well with an upper energy level of 21 eV. This is supported by the emission line being stronger in the $MgSO_4$ spectrum, which has been recorded with an almost twice as high laser pulse energy compared to the spectrum of pure sulfur. It is, however, even stronger in the CaF_2+$CaSO_4$ spectrum acquired with 25 mJ, opposing this explanation. Neither the NIST data base nor the atomic spectral line data base by Kurucz and Bell lists another transition of the involved elements around the measured position of 165.7 nm. Another realistic explanation could be a carbon impurity, e.g. due to contamination with organic material during sample handling. The observed C I emission around 165.7 nm, which is a group of six unresolved spectral lines, is very intense as we will see in the carbonate spectra in the following subsection. The signal level comparable to the neighbouring S I line in the CaF_2+$CaSO_4$ spectrum is, however, surprising. Simulations with different initial temperatures, see section 2.1.3 for details, predict that the line strength of all six C I lines together is about five times higher than that of the S I line. Accordingly, to reach a comparable signal level, the C concentration would need to be in the order of a fifth of the S concentration, which should not be the case for impurities or surface contamination. On the other hand, the spectroscopic constants in this spectral range are sometimes not well researched yet, leaving the attribution to C I as the most likely explanation.

Emission lines from Mg have not been identified in Figure 5.2b. From wavelength tables, the strongest lines in the observed spectral range would be expected at 182.8 nm from Mg I and at 173.8 nm from Mg II. The small peak at 185.5 nm is also visible in the Na_2SO_4 spectrum, though much weaker, and should therefore not relate to Mg. It is also too strong in the Na_2SO_4 spectrum to come from a Mg impurity, which could otherwise explain its existence. The spectral position matches an Al III line, as does the accompanying weaker emission at 186.3 nm. Although Al is not stated as a trace impurity by the chemical company providing the sample material and its concentration should therefore be rather low, the attribution to Al III is further supported by the two weak features at 160.6 and 161.2 nm, which match Al III emission lines as well.

Another weak feature in the $MgSO_4$ spectrum is the so-called Lyman-α transition of H at 121.6 nm. It is also detected in the sample containing hydrated $CaSO_4$, shown in panel (e). As described in section 4.3.5, the sensitivity of the current set-up is reduced by approx. two orders of magnitude in this spectral range compared to the 180 nm range. Hence, the Lyman-α transition is supposedly at least as intense as the strongest S I line at 180.7 nm.

The spectrum of Na_2SO_4 also shows only the stronger S I lines at 166.7 nm and around 180 nm, and the O I triplet at 130 nm, but no emission from Na. The NIST data base for Na lists only transitions from ionized species with a minimum upper energy level of 42 eV for Na II. Thus, emission from Na, which is known for its very intense yellow lines at 589 nm in LIBS spectra recorded in the visible range [112], is not expected in the VUV.

The very similar K_2SO_4 exhibits a richer spectrum with multiple K II emission lines but also additional S I, II and III lines, which have not been observed in the sample of pure sulfur. Compared to the NIR emission at 766 and 770 nm from K I, these K II lines are, however, rather weak. The appearance of additional emission lines from ionized sulfur could be explained by a

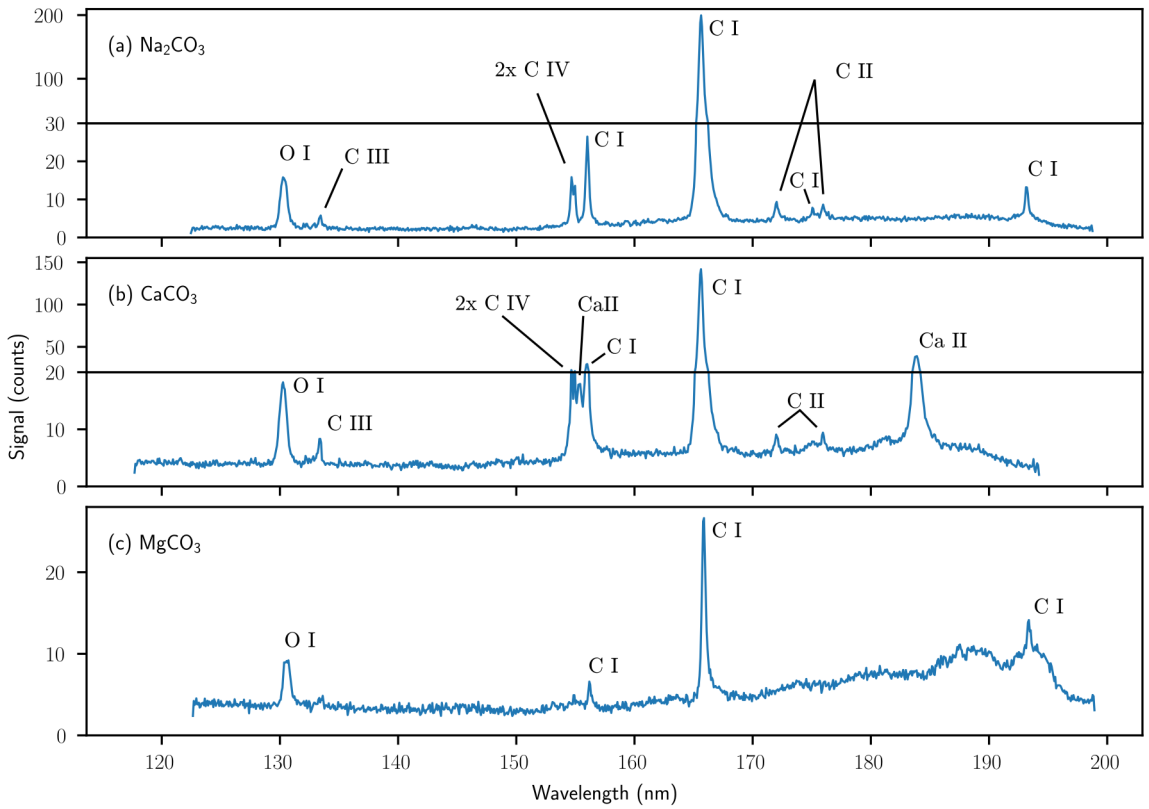

Figure 5.3: Spectra of the carbonate samples (a) Na_2CO_3, (b) $CaCO_3$ and (c) $MgCO_3$. The employed pulse energies are 25 mJ for Na and 32 mJ for Ca and Mg. Multiple emission lines from C I, C II, C III and C IV as well as the O I triplet can be seen in the spectra. Except from Ca, the cations do not show any emission. The panels a and b have segmented y-axes with two linear parts to increase the visibility of low intensity emission lines.

higher electron temperature due to improved laser coupling. On the other hand, the intensity of the K_2SO_4 spectrum and its features is in general higher than that of the spectrum of Na_2SO_4, which has been measured with the same pulse energy of 32 mJ: The O I triplet has a more than one order of magnitude larger amplitude and the amplitude of the S I triplet at 180 nm is increased by a factor of five. This may be due to experimental differences that make the spectra not directly comparable. The K_2SO_4 spectrum has been recorded after the detector was sent to the manufacturer for maintenance as mentioned in section 4.3.2 while all other S-related spectra have been acquired earlier. Upon the return of the detector, the set-up was re-aligned in order to reduce the observed aberrations. Furthermore, after this re-alignment a higher detector temperature of −60 °C instead of −80 °C has been employed, which may influence the sensitivity of the detector. A similarly increased sensitivity is suspected for the chloride spectra in section 5.2.3 and for the study about Cl detection in lunar analogue in chapter 7, which have been recorded after the re-alignment as well.

For Ca, another element expressing strong lines (e.g. Ca II at 393.4 and 396.8 nm) in typical LIBS spectra already at very low concentration levels [113], only one pair of lines, which cannot be resolved, has been identified at 183.8 and 184.0 nm, originating from singly ionized species.

Finally, all four sulfate spectra show the O I triplet at 130.2, 130.5 and 130.6 , which is merged to one broad feature centred around 130.3 nm due to physical broadening and the limited resolution.

5.2.2 Carbonates

Na_2CO_3, $CaCO_3$ and $MgCO_3$ have been studied as C-bearing compounds. Their spectra are shown in Figure 5.3. All three spectra show the intense C I emission line at 165.7 nm that has been referenced in the previous subsection as a potential C impurity in the sulfate spectra,

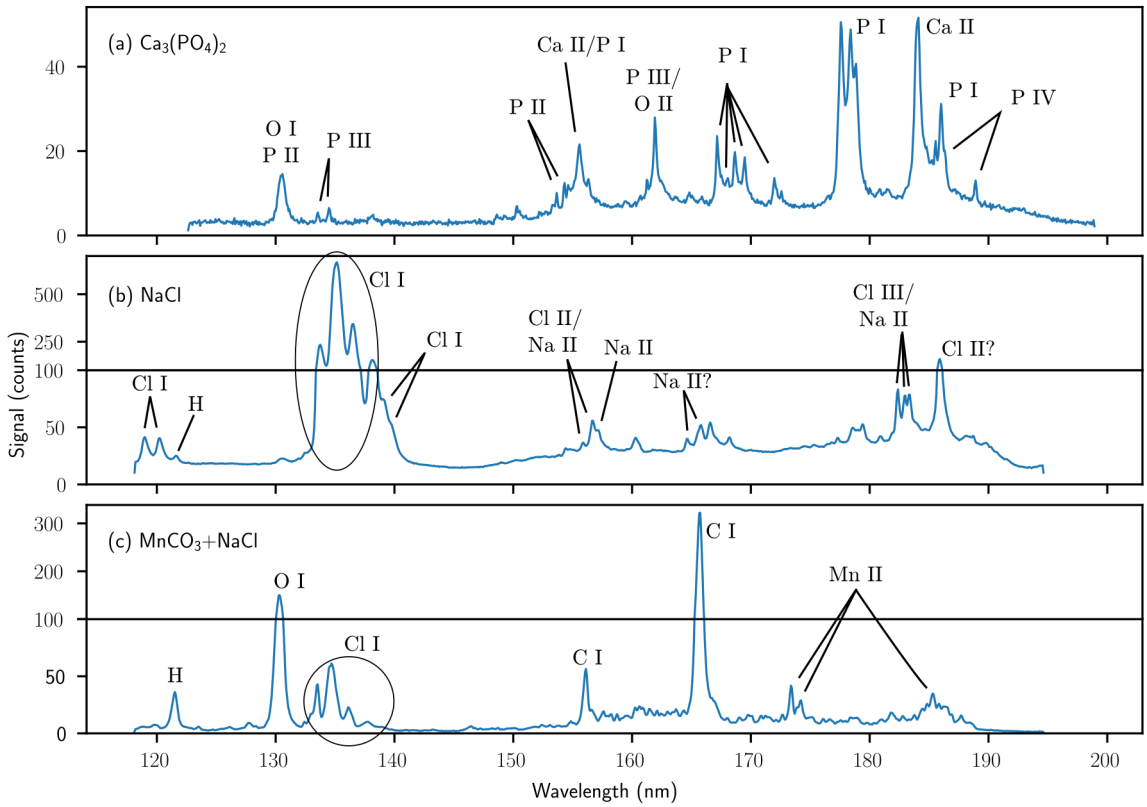

Figure 5.4: Spectra of (a) $Ca_3(PO_4)_2$, (b) NaCl and (c) $MnCO_3$+NaCl (ratio unknown). The employed pulse energy is 25 mJ for all three samples. While phosphorus has several moderate intensity emission lines distributed across large parts of the spectral range, chlorine exhibits very intense emission concentrated around 135 nm. The $MnCO_3$ containing sample shows three emission lines from Mn II. Panels b and c have split y-axes with the lower sections being stretched to enhance the visibility of weak emission lines.

especially for the CaF_2+$CaSO_4$ sample. Further C I emission lines, which can be identified in pure samples but might be easily superseded upon spectral interference in mixtures, are located at 156.1, 175.2 and 193.1 nm. The transitions emitting at 172.2 and 176.0 nm have been attributed to C II. Besides neutral and singly ionized carbon emission, also transitions from C III at 133.5 nm and from triply ionized C IV at 154.8 and 155.1 nm have been identified. The attribution to such a high ionization state is supported by a significant increase in emission intensity for these lines relative to the other emission lines in the spectra when increasing the laser pulse energy.

The cationic emission is similar to the observations made for the sulfates: Na and Mg do not show any emission lines and Ca has an ionic transition at 184 nm. For $CaCO_3$, however, another Ca II transition at 155.4 nm can be observed. Its absence in the gypsum spectrum can be explained with the in general stronger signal detected for the $CaCO_3$ sample, due to an apparent better laser coupling and the higher pulse energy of 32 instead of 25 mJ.

5.2.3 Phosphorus and chlorine

For phosphorus and chlorine line identification, I prepared a sample of $Ca_3(PO_4)_2$ and a sample of NaCl. Furthermore, a mixed sample of $MnCO_3$+NaCl at an unknown ratio from a previous study was examined with the VUV-LIBS set-up. The spectra are shown in Figure 5.4.

For the phosphate sample, many emission lines attributable to P I, P II, P III and possibly even P IV can be observed, ranging from 133 to 186 nm. Most of them are, however, low in intensity. This suggests high detection limits but increases the chance to find interference-free emission lines. From this spectrum, the P I triplet at 177.5, 178.3 and 178.8 nm appears most promising for phosphorus detection in unknown samples, as it is the most intense emission signal and has a pattern, which should be resolvable with most instruments. The structure of four more

P I lines at 167.2, 168.0, 168.6 and 169.4 nm and the single P I line at 185.9 nm could be used as supportive indicators for the presence of phosphorus. The intensity ratios between all these lines should be similar in most conditions, as the respective transitions involve similar upper energy levels ranging from 7.0 to 8.1 eV. If more and more phosphorus is ionized in a hot plasma, of course, the intensities for these lines will drop and one will need to test for the ionic P II (153.6 and 154.2 nm) and P III (133.5 and 134.4 nm) transitions. Further P II emission lines are located in the range 130.2–131.1 nm, which are superimposed on the O I triplet in the shown spectrum but can still be recognized from a red shift of the centre of the compound emission feature. The observed emission line at 161.9 nm is probably ionic, as its relative intensity compared to the rest of the spectrum rises upon an increase of the laser pulse energy, and may be attributed to P III or O II. Since O II has not been observed at this wavelength in any other spectrum so far, P III seems more likely. Two spectral features located at 186.3 nm on the edge of the P I line and at 188.9 nm may originate from P IV. Unfortunately, for the line at 186.3 nm no spectrometric details are available in the line data bases to estimate a likelihood for the emission. Lastly, the origin of the emission line at 155.5 nm is uncertain: It might be related to Ca II, as has been observed with a similar intensity in $CaCO_3$, or it could be attributed to a P I transition, which is only listed in the data base by Kurucz and Bell but not in the one provided by NIST. Although it has been found in the spectrum of $CaCO_3$, no sign of this emission line has been observed in the spectrum of CaF_2+$CaSO_4$, thus questioning the attribution to Ca. Measurements on different phosphates could reveal if the P I line listed in the data base by Kurucz and Bell is typically of observable intensity or not.

The NaCl spectrum is dominated by five Cl I lines at 133.6, 134.7, 135.2, 136.3 and 138.0 nm, of which the lines at 134.7 and 135.2 nm cannot be resolved in the displayed spectrum. Considering the low sensitivity of the set-up in this spectral range, the line strength of these lines must be considerably higher than for any other emission line discussed so far. On the other hand, the O I triplet in the spectrum of the carbonate-chloride mixture, panel (c), is also significantly stronger than in any other sulfate or carbonate spectrum shown before, with the exception of K_2SO_4, for which a similarly increased sensitivity has been noted. Both NaCl and $MnCO_3$+NaCl have as well been studied after the re-alignment of the set-up and at the higher detector temperature of −60 °C, thus supporting systematic differences compared to the older measurements. Besides these strong Cl I lines, weaker transitions of Cl I have been identified at 118.9 and 120.1 nm, and on the wing of 138.0 nm line at 139.0 and 139.7 nm. Furthermore, weak emission at the position of the Lyman-α transition (121.6 nm) and of the O I triplet (130.3 nm) can be identified, suggesting the presence of adsorbed water at the sample surface. Many of the remaining spectral features cannot be identified with certainty. First of all, for the clearly evident emission line at 185.9 nm no reasonable transition is listed in the data bases. The most probable transition found for this spectral line is from Cl II and located at 185.7 nm, according to NIST [52]. However, the listed reference wavelength and the measured wavelength after a local wavelength calibration is typically less than 0.1 nm off. The transitions at 155.8 and 156.5 nm can be attributed to Cl II or Na II. For the transition at 157.1 nm, which probably belongs to the same group as the previous two potential Na II transitions, only Na II is listed in the data bases. Thus, all three emission lines probably originate from Na II. Two more Na II transitions could be located at 164.6 and 165.8 nm. The three lines detected at 182.3, 182.8 and 183.3 nm could be either from Na II as well, or from Cl III. Since none of the Na II lines has been observed in Na_2SO_4 or Na_2CO_3, the attribution to Cl-related emission lines is, in general, more reasonable. Further studies on both chlorine- and sodium-bearing samples should be conducted in order to clarify the origin of the observed emission lines. The spectrum of the mixed sample of $MnCO_3$+NaCl exhibits three Mn II lines at 173.4, 174.5 and 185.3 nm in addition to the Cl I lines around 134 nm, the C I lines at 156.1 and 165.7 nm, O I at 130.3 and H at 121.6 nm.

Due to the optimized wavelength calibration, see section 4.3.3 for details, most of the emission features observed in the spectra of this section could be identified and uniquely attributed to emission lines expected from spectral data bases. The relative intensities of these emission lines

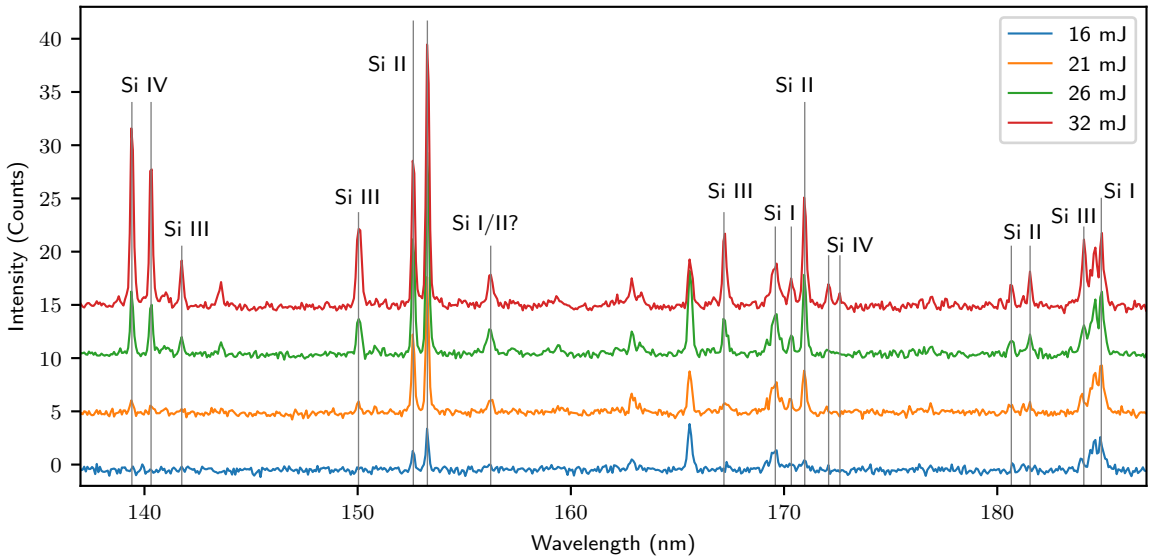

Figure 5.5: LIBS spectra of a Si wafer recorded with different laser pulse energies. Si IV lines appear at 26 mJ and their intensities increase strongly with the laser pulse energy while Si I and Si II intensities change only little. The emission line at 165.7 nm is likely from C I due to contamination during sample handling. A vertical offset between the spectra has been applied for clarity.

are, however, difficult to compare due to (1) the different laser coupling for the various samples leading to different required and employed pulse energies, (2) two different configurations of the set-up, supposedly leading to significant differences in the sensitivity, and (3) the sparse data on the system response determined in section 4.3.5. Lastly, uncertain and partly incomplete data in the spectral data bases prevent the prediction of expected intensity ratios and thereby complicate the identification of some observed emission features in the VUV spectral range.

5.3 Dependence of the ionization state on the laser pulse energy

The LIBS signal depends, among other factors of influence, on the laser power density (irradiance). In ambient atmospheric conditions, the expanding plasma is confined by the surrounding gas and frequent collisions between the plasma species result in an equilibrium state on short timescales, which can be described by a temperature. Studies have shown that this equilibrium temperature for a certain phase after the plasma initiation changes only slightly upon changes in the laser pulse energy and therefore in the irradiance [114, 115]. A common explanation for this counter-intuitive behaviour is that the spatial extent of the plasma increases for higher pulse energies, resulting in unchanged density and pressure conditions [115, 116]. Thus, as long as saturation effects such as self-absorption can be neglected, the emission intensity ratios of the spectral lines remain mostly unchanged while the total intensity of the spectrum increases with pulse energy due to a larger amount of ablated mass [27]. In vacuum, on the other hand, the high degree of ionization reached during plasma initiation is conserved because the lack of confinement and the inherent long mean free path length hamper efficient electron-ion recombination. This suggests an already higher degree of ionization for a laser-induced plasma in vacuum, as reported in other publications [5, 21, 117]. Higher laser powers cause an even higher degree of ionization during the plasma formation, which is then maintained and results in stronger emission lines from high ionization states.

In agreement with observations by Radziemski et al. [27], I found that increasing the laser pulse energy adds additional lines to the spectra that are related to higher ionized states. This can be seen in Figure 5.5, showing spectra of the Si wafer at different laser pulse energies. The spectra have been acquired in vacuum while using the slit aperture, cf. Figure 4.16c, to increase the resolution and to suppress emission from the plasma centre, thus gating out the plasma

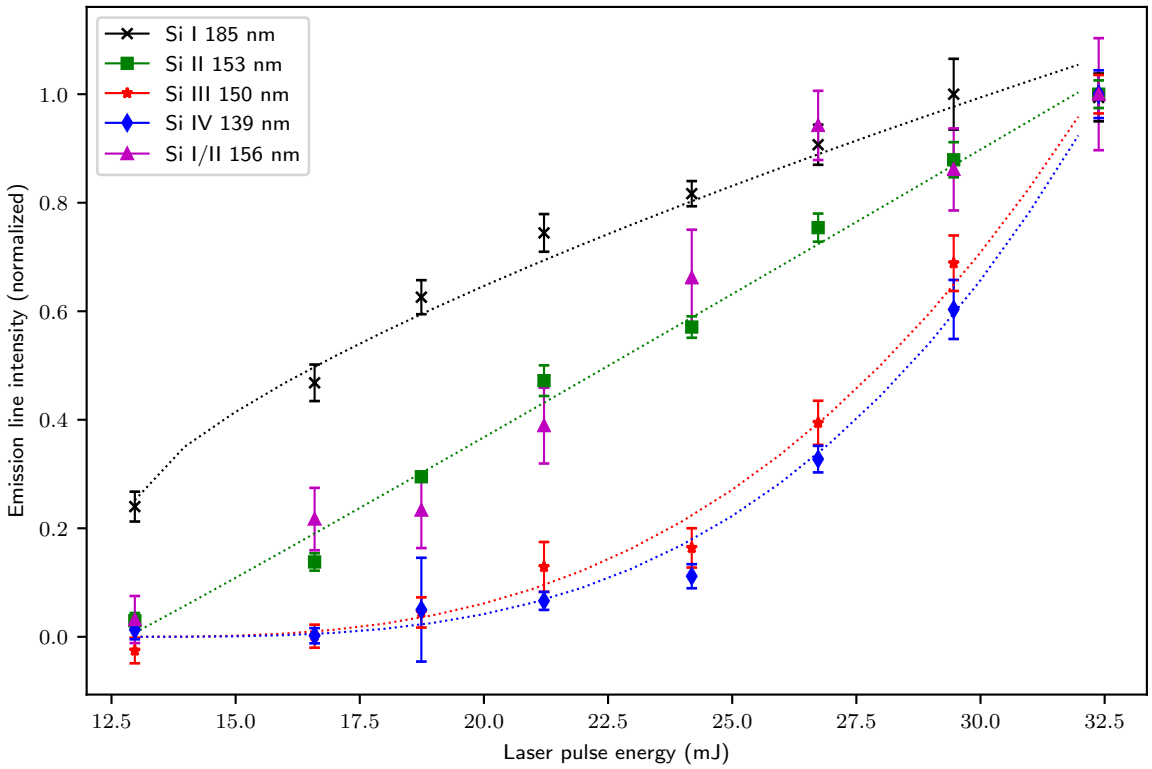

Figure 5.6: Intensities of emission lines of different ionization states as a function of laser pulse energy. All curves have been normalized to compare the energy-intensity relationship. The magenta triangles refer to the transition at 156 nm, which could not be uniquely identified as Si I or Si II by reference wavelengths. From the obtained trend shown in this graph, it could still be either of them, but Si II looks more likely. The dotted lines are guides to the eye based on fits of $y = c \cdot x^a$ with appropriate offsets. The error bars indicate the standard deviation of the ten measurements per pulse energy.

initiation phase. With 16 mJ per pulse, the excitation is still close to the LIBS threshold and a very dim plasma is generated. The first spectral lines appear at 152.7 and 153.3 nm as well as between 169.2 and 170.1 nm and between 184.0 and 185.5 nm. The latter have an SNR of 5-10 and are related to neutral Si. The doublet around 153 nm is a bit stronger and belongs to Si II. Knowing their positions, one can also see indications of the Si II lines at 180.8 and 181.7 nm with an SNR of ≈ 2. Increasing the pulse energy to 21 mJ gives rise to another emission line of singly ionized species at 171.1 nm, while the aforementioned neutral emission lines gain intensity and the hinted Si II lines become identifiable as lines. At 26 mJ, a Si IV doublet at 139.4 and 140.3 nm, and Si III lines at 141.7, 150.1 and 167.3 nm appear. For the highest pulse energy of 32 mJ, the Si IV doublet becomes one of the most dominant features of the spectrum.

The different intensity gain for lines of different ionization states can be intuitively seen from the emission line constellation around 170 nm: The left S I line at 169.8 nm is already visible for the lowest employed pulse energy and does not change much in intensity when increasing the laser pulse energy, while the close-by S II line at 171.1 nm only appears for 21 mJ and above and quickly supersedes the S I line. An analytical approach is shown in Figure 5.6, where the intensities of emission lines of different ionization states are shown with respect to the laser pulse energy. To extract the intensities, the spectral channels related to the respective emission line have been summed after subtracting the local background level derived from a linear regression in the peak region. This is preferred over a fit to the spectrum in order to be able to also assess an intensity for very weak emission lines with amplitudes in the order of the noise level. The data has then been normalized with the maximum intensity of the line to make the gain behaviour visible. Fit functions of the shape $f(x) = c \cdot x^a$ with appropriate offsets are used as guides to the eye. The figure shows that the neutral emission line at 185 nm has a strong increase in intensity at first, but grows only slowly for higher pulse energies. The ionized transitions, on the other

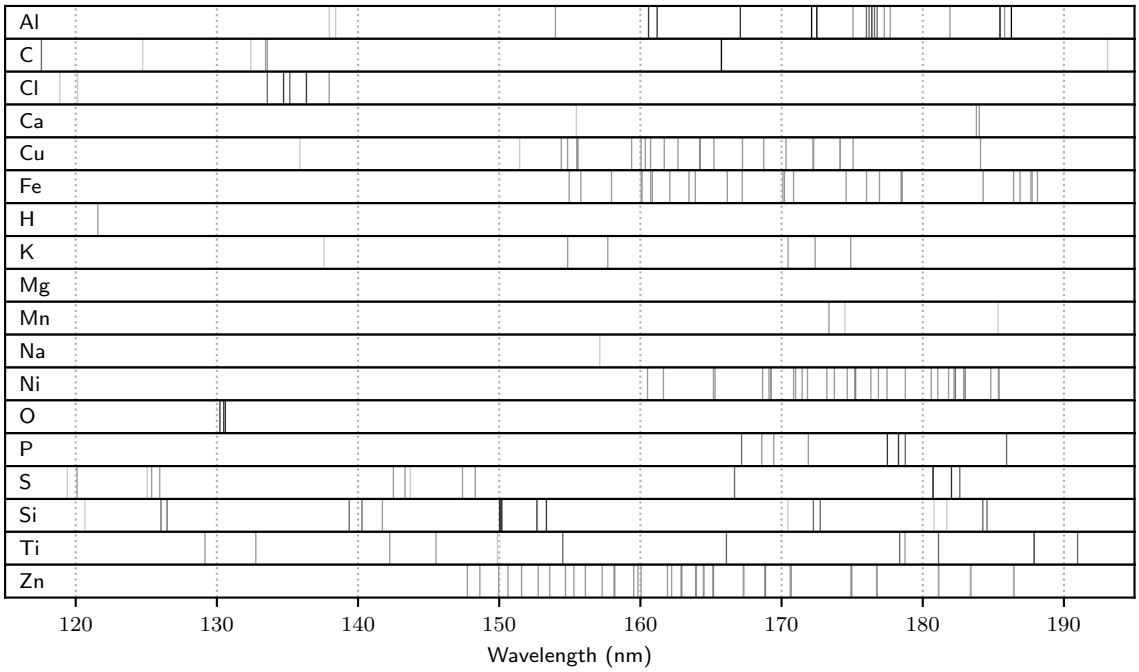

Figure 5.7: Reference positions of identified spectral lines of different elements. The grey level of the markers indicates the intensity estimate for the respective line, with bright markers for weak lines and dark markers for strong lines. Most lines of the dense spectra of Cu, Fe, Ni and Zn have been automatically extracted from Figure 5.1 and set to an intensity level of 2 according to Table 5.1. For Mg, no emission line has been identified.

hand, are weak in the beginning and strongly gain intensity at higher laser pulse energies. While all three ionized lines show an increasing slope, this trend is more pronounced the higher the ionization state. The difference between the behaviour of the depicted Si III and Si IV lines is rather low. This is likely related to the high energy level of the selected Si III transition. The lower level involved in this transition has an energy of $E_l = 17.7\,\text{eV}$, while the other lines relate to transitions to the ground state. For Si III, however, the lowest E_l for transitions in the wavelength range 130–190 nm is 6.6 eV at 130.3 nm, where the set-up has a low sensitivity. The signal of the 19.0→10.3 eV transition at 141.7 nm is weak as well, leaving the analysed line as the best choice.

One emission line in Figure 5.5 at 156.2 nm cannot be uniquely identified. It could either be a Si II transition listed in the NIST atomic spectra data base [52] without further details like energy levels or Einstein coefficients, or a Si I transition from 7.9 eV to the ground state listed in the atomic spectral line data base by Kurucz and Bell [53]. The magenta triangles in Figure 5.6 show the pulse energy-to-line intensity relationship for this line. The similarity of the trend to that of the Si II transition shown in green suggests that it is also a transition originating from Si II rather than from neutral Si.

5.4 Potential spectral interferences

Figure 5.7 gives an overview of the identified lines of 17 elements. For Mg, no line has been identified. For the metals Cu, Fe, Ni and Zn, most of the displayed emission lines have been automatically extracted from the respective spectrum shown in Figure 5.1. The poor resolution of the spectra and the vast amount of emission lines in the data bases without complete information did not allow a line-by-line assignment of the observed emission. The relative intensities of the other lines have been estimated subjectively and are grouped in five intensity levels according to Table 5.1. In the overview figure, they are represented using different greyscale values, with brighter markers indicating weaker lines. The automatically extracted metal lines are shown with an intensity level of two. In addition to the figure, the identified lines and their intensity

Level	Description
5	Very strong line. Should be present whenever element is detected.
4	Strong line. Should usually be present when element is detected.
3	Medium line. Usually visible; might disappear for certain plasma conditions.
2	Weak line. Can still be detected in low interference scenarios.
1	Very weak line. Might not be useful in many cases.

Table 5.1: Definition of relative intensity levels.

estimates are listed in Table 5.2.

These results must, however, be used with caution. The relative intensities of the identified lines strongly depend on the plasma conditions [118], as has been shown in the previous section. Some of the porous salt samples express very low line intensities which were mainly caused by poor laser coupling and an in general weaker plasma. In other matrices like doped metals or naturally grown rocks, these lines might possibly be much stronger than indicated. Emission lines from S II and S III, for example, have only been observed in K_2SO_4 and pyrrhotite (Fe_xS), but not in pure sulfur. Furthermore, the assigned intensities are as detected with the present VUV-LIBS set-up. Without measuring the sensitivity of the set-up in the VUV, the detected signal intensities cannot be corrected for the instrumental response. Lastly, not all emission lines could be identified yet and some elements might emit further strong lines not listed here.

According to Figure 5.7, many elements should have interference-free emission lines, depending on the other constituents of the sample. Based on the samples studied so far, the elements Al, C, Cl, O, S and Si can typically be uniquely identified.

λ/nm	Species	Int.	λ/nm	Species	Int.	λ/nm	Species	Int.	λ/nm	Species	Int.
117.571	C III	3	154.501	Ti II	3	167.168	P I	3	176.860	Ni*	
118.877	Cl I	1	154.694	Ni*		167.215	Fe*		176.936	Fe*	
119.406	S III	1	154.842	Cu II	2	167.232	Cu*		177.280	Al II	2
120.097	S III	2	154.848	K II	2	167.305	Zn III	4	177.470	Ni*	
120.135	Cl I	1	154.957	Fe*		167.307	Ni*		177.495	P I	4
120.650	Si III	1	155.288	Ni*		168.598	P I	2	177.697	Al II	2
121.567	H I	2	155.464	Ca II	1	168.653	Ni*		178.284	P I	4
124.738	C III	1	155.513	Cu II	3	168.734	Cu*		178.364	Ti III	3
125.058	S II	1	155.585	Cu*		168.809	Ni*		178.463	Fe*	
125.381	S II	2	155.780	Fe*		168.859	Zn III	3	178.528	Fe II	3
125.952	S II	2	156.104	Ni*		169.107	Ni*		178.742	Ti III	2
126.042	Si II	3	157.121	Na II	1	169.251	Ni III	3	178.766	P I	3
126.473	Si II	3	157.294	Ni*		169.449	P I	2	178.768	Ni*	
129.162	Ti III	2	157.690	K II	2	170.092	Fe*		180.603	Ni*	
130.217	O I	4	157.953	Fe*		170.205	Fe II	2	180.731	S I	5
130.486	O I	4	158.153	Zn III	4	170.314	Cu*		180.801	Si II	1
130.603	O I	4	158.186	Ni*		170.444	Si I	1	181.063	Ni*	
132.395	C II	1	159.378	Cu*		170.460	K II	2	181.101	Zn II	1
132.760	Ti III	2	159.527	Ni*		170.615	Ni*		181.119	Ti III	3
133.453	C II	2	159.825	Ni*		170.665	Zn III	3	181.135	Ni*	
133.571	C II	2	160.049	Cu*		170.851	Fe*		181.692	Si II	1
133.573	Cl I	3	160.049	Ni*		170.851	Ni*		181.828	Ni*	
134.724	Cl I	4	160.054	Fe*		170.990	Ni III	2	181.929	Al II	2
135.166	Cl I	3	160.121	Fe II	2	171.458	Ni*		182.034	S I	4
135.877	Cu II	1	160.347	Cu*		171.837	Ni*		182.212	Ni*	
136.345	Cl I	4	160.505	Ni*		171.897	P I	2	182.305	Ni III	3
137.590	K II	1	160.577	Al III	4	172.127	Al II	5	182.624	S I	3
137.953	Cl I	2	160.720	Cu*		172.237	Cu III	3	182.901	Ni*	
137.967	Al III	1	160.731	Fe*		172.253	Si IV	3	183.000	Ni III	3
138.414	Al III	1	160.845	Fe II	2	172.274	Cu*		183.357	Zn II	1
139.376	Si IV	3	161.187	Al III	4	172.380	K II	2	183.419	Ni*	
140.277	Si IV	3	161.633	Ni*		172.498	Al II	5	183.801	Ca II	2
141.724	Si III	2	161.691	Cu*		172.738	Si IV	3	184.006	Ca II	2
142.241	Ti III	2	161.915	Ni*		173.205	Ni*		184.091	Cu III	2
142.503	S I	2	162.085	Fe*		173.355	Mn II	2	184.255	Si III	3
143.328	S I	2	162.214	Ni*		173.737	Ni*		184.282	Fe*	
143.697	S I	1	162.662	Cu*		174.137	Cu III	2	184.551	Si I	3
145.519	Ti III	2	162.886	Ni*		174.161	Cu*		184.820	Ni*	
147.399	S I	2	162.919	Zn III	4	174.485	Mn II	1	185.327	Mn II	1
147.744	Ni*		163.441	Fe*		174.574	Fe*		185.358	Ni*	
148.304	S I	2	163.893	Fe*		174.650	Ni*		185.414	Ni III	2
148.629	Ni*		163.933	Zn III	4	174.896	K II	2	185.472	Al III	5
149.870	Ti III	1	163.934	Ni*		174.917	Ni*		185.803	Al II	2
149.957	Ni*		164.221	Cu III	4	174.963	Zn III	3	185.939	P I	3
150.024	Si III	4	164.233	Cu*		175.061	Al II	2	186.279	Al III	5
150.115	Si III	4	164.458	Ni*		175.068	Cu*		186.412	Zn II	1
150.119	Si III	4	164.482	Zn III	4	175.183	Ni*		186.434	Fe*	
150.188	Si III	4	165.132	Ni*		175.243	Ni III	3	186.471	Ni*	
150.622	Ni*		165.174	Zn III	3	176.011	Al II	3	186.895	Fe*	
151.449	Cu II	1	165.175	Ni*		176.021	Fe*		187.665	Fe*	
151.583	Ni*		165.207	Cu*		176.198	Al II	3	187.747	Fe II	2
152.671	Si II	4	165.287	Ni III	2	176.326	Ni*		187.889	Ti III	4
152.767	Ni*		165.738	C I	5	176.395	Al II	4	188.127	Fe*	
153.344	Si II	4	166.094	Ti III	3	176.582	Al II	3	190.966	Ti II	3
153.582	Ni*		166.157	Fe*		176.733	Ni*		193.091	C I	1
153.983	Al II	2	166.669	S I	3	176.769	Zn III	2	199.053	Al II	2
154.397	Cu*		167.079	Al II	4	176.773	Al II	3			

Table 5.2: Identified VUV lines sorted by wavelength λ. An asterisk (*) in the species designation indicates that the emission line has been extracted automatically. Therefore, the ionization state is unknown, the listed wavelength is subject to deviations in the wavelength calibration and there is a potential risk that the emission line originates from an impurity. The relative intensity (Int.) is subjectively judged according to Table 5.1.

Chapter 6

Detection and Quantification of Sulfur in Lunar Analogues

Sulfur is one of the elements that are challenging for LIBS to detect in the commonly investigated wavelength range but at the same time of particular interest for planetary scientists [11, 27]. It plays an important role when assessing a planet's geological history with respect to volcanic activity and to the past atmospheric conditions [119, 120]. In the light of recent ambitions to return to the Moon in the upcoming decade [4] and to establish a permanent research facility on the lunar surface [2, 3], similar to the International Space Station, in-situ resource utilization (ISRU) became an important topic [121, 122]. While ISRU often refers to the production of space craft fuel, i.e. H_2, O_2 and hydrocarbons, on the Moon and other planets to allow refuelling for deep-space missions [123, 124], it also includes other aspects such as the production of building materials [125]. Besides the production of S-based lunar concrete [126], Vaniman et al. [29] identified several other potential applications based on the availability of S on the lunar surface, such as the use of liquid SO_2 in hydraulic systems or storage batteries based on Na and S, thereby pointing out the element's relevance. According to the Lunar Sourcebook [127, sec. 8.7], the highest S concentrations encountered on the Moon are in the order of 0.2 at% S.

For detection with LIBS, Gaft et al. [26] compared S emission lines in the VUV (S I; 180.7, 182.0 and 182.6 nm), the NIR (S I; 909.5 and 922.1 nm), and the visible spectral range (S II; 542.7 and 544.9 nm) for different excitation wavelengths as well as for single and double pulse configurations. Investigating S in coal, they found increased signal levels for the emission lines in the visible and NIR spectral range with the double pulse configuration, but the LOD remained in the order of 5–10 %. When using the VUV emission lines, on the other hand, concentrations below 1 % S could be detected already with single pulse excitation. Due to the intended application of in-situ S assessment in coal mining, the experiments were conducted in ambient air with a N_2-filled spectrometer. For other publications reporting on the VUV emission lines of S I around 180 nm, different atmospheric conditions have been employed, mainly argon at different pressures, but none of them involves a pressure below 200 Pa [27, 105, 107, 128, 129].

In this chapter, the potential of VUV-LIBS for the detection and quantification of S in a matrix of lunar analogue material is investigated. The experiments are conducted at an ambient pressure of $\leq 10^{-2}$ Pa, which is sufficiently low for LIBS to emulate the lunar atmospheric conditions [21], while using a laser pulse energy of 25 mJ, which is in the operating range of the ChemCam laser [10] and therefore realistic for an in-situ space instrument. The detection and quantification of S are based on a univariate approach to test their feasibility in a first study with this new VUV-LIBS set-up. In future studies, the presented results may be improved due to experimental improvements on the one hand, but also through the use of multivariate analysis techniques on the other hand. The first section gives an overview of the samples investigated in this chapter. Section 6.2 presents a preliminary study with samples of Na_2SO_4 mixed in Na_2CO_3 for the detection of S without interfering emission of Al, Fe, Si and Ti from the lunar analogue matrix. The subsequent sections treat the detection of pure S in Lunar Highland sim-

Name	Matrix	Admixture	Concentrations (at% S)
Na_2CO_3/Na_2SO_4	Na_2CO_3	Na_2SO_4	0.5; 1.0; 1.6; 2.0; 2.7; 3.0; 3.6
LHS/S1	LHS-1	S	0.5; 1.0; 1.6; 2.0; 2.5; 3.0; 3.5; 4.1; 5.0; 6.0; 7.0; 8.1
LHS/S2	LHS-1	S	0.6; 1.5; 2.1; 2.5; 3.1; 3.6; 4.0; 5.0; 6.0; 6.9; 7.9
LHS/K_2SO_4	LHS-1	K_2SO_4	0.5; 1.1; 1.5; 2.1; 2.5; 3.0; 3.5; 4.1
LHS/Na_2SO_4	LHS-1	Na_2SO_4	0.5; 1.1; 1.6; 2.0; 2.5; 3.2; 3.5; 3.8; 4.1
LMS/Na_2SO_4	LMS-1	Na_2SO_4	0.5; 1.0; 1.3; 1.6; 2.0; 2.5; 3.1; 3.6; 4.1

Table 6.1: Overview of the prepared samples used in this study.

ulant (6.3), the detection of S from sulfates in Lunar Highland simulant (6.4), and the detection of S from Na_2SO_4 in Lunar Mare simulant (6.5). The spectra presented here have been recorded without a resolution-enhancing aperture, cf. section 4.3.4. Large parts of the results have been published [130].

6.1 Samples

For this study, pure S as well as two different sulfates have been mixed into the lunar regolith simulants LHS-1 (Lunar Highland) and LMS-1 (Lunar Mare) [87] in varying concentrations to investigate the potential for quantification of S. An overview of the investigated samples is given in Table 6.1. The stated concentration is the bulk concentration calculated from the actual amount of the components used for sample preparation and therefore differs from an intended equidistance in molar fraction. The samples from one series were mixed and pressed within one day to reduce systematic differences within the series. Gaps in the concentration series arise because some samples broke during the transfer to the sample holder or otherwise during sample handling and could therefore not be analysed. A relationship between fragility and S concentration has not been observed. Furthermore, some samples fell off the sample holder during the measurement. This mainly occurred when the sample holder was close to one end of its translation range and may be due to a mechanical resonance with vibrations from the turbomolecular pumps. The unusable samples were not reproduced in order to avoid systematic differences. Since the samples were stored in plastic boxes, adsorption of water vapour on the sample surface is possible and could lead to incomparable results for newer samples. Due to the later arising necessity to confirm the results of the first measurements with lunar analogue material, the sample series of LHS with pure S (LHS/S1) has, however, been reproduced entirely, thus resulting in the series LHS/S2.

6.2 Sodium sulfate in sodium carbonate

An averaged spectrum of the four measurements with 25 mJ pulse energy on the sample with 1.6 at% S is shown in Figure 6.1. In the spectrum, all the carbon related emission lines from different ionization states identified in chapter 5 as well as the O I triplet around 130 nm can be found. The strong S I lines at 180.7, 182.0 and 182.6 nm observed in pure S and various sulfates during line identification can also be seen, but have a very low intensity compared to the three stronger C I emission lines. They are, however, free from interference as intended for this initial study. The fourth strong S I line at 166.7 nm is superimposed by the close-by strong C I line, which dominates the spectrum. Since this S I emission line has a similar line strength as the emission line at 182.6 nm, it would likely still be difficult to identify at this low S concentration even when the broadening of the C I line was reduced with the slit aperture, cf. section 4.3.4. Nonetheless, the emission intensity for S can be assessed and related to the molar fraction of S.

A close-up of the spectral region around 180 nm for the same sample is shown in Figure 6.2. Other than for the complete spectrum presented in Figure 6.1, this figure shows a single measurement, meaning the integrated signal of 25 consecutive plasma plumes excited at the same

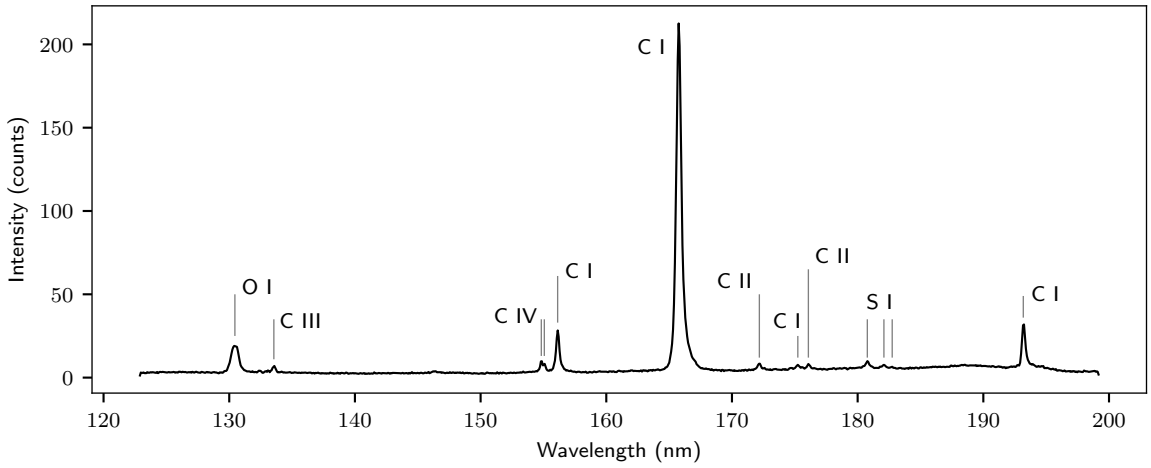

Figure 6.1: Average spectrum of four measurements on the sample of the Na_2CO_3/Na_2SO_4 series with 1.6 at% S.

location on sample surface. While two of the three emission lines are clearly evident, the third emission line at 182.6 nm cannot be identified as such with certainty. The SNR for this line is only 3.4, based on a noise level estimate in the adjacent spectral window 177.3–179.0 nm. To measure the intensity, a model of three lines and a linear background estimate is fitted to the data. For the strongest line at 180.7 nm, a Voigt profile is used to best capture the peak area, as this will be used as the intensity measure in calibration curves. To reduce the number of fit parameters, the other two lines are only modelled with a Gaussian shape. Both of them are not used for the calibration curves and are mainly included to improve the estimate of the base line level for the 180.7 nm emission line.

The top panel of Figure 6.3 shows the calibration curve for S based on the extracted intensities. The red crosses mark the average intensity per sample. Additional black horizontal bars visualize the results of the individual four measurements per sample. The signal intensity for

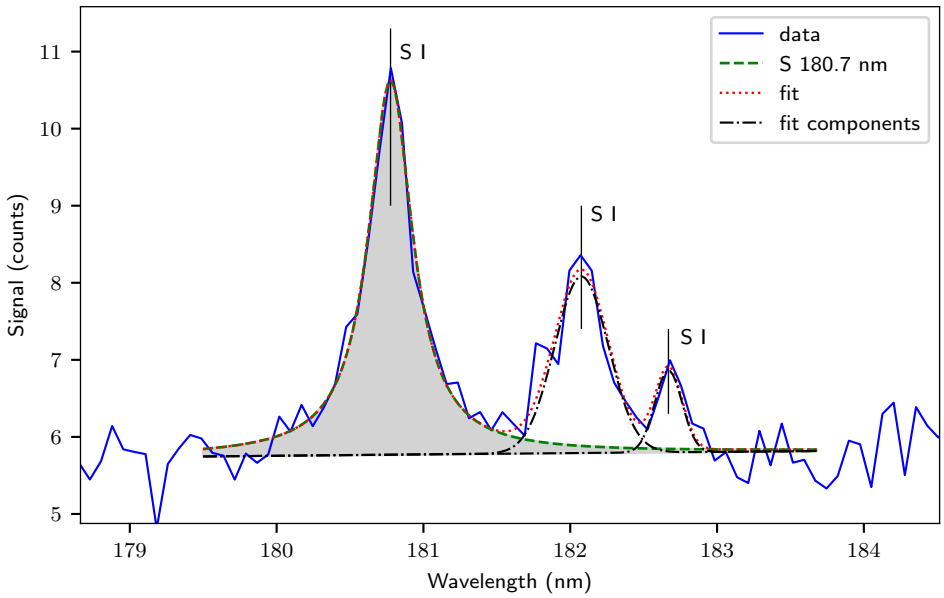

Figure 6.2: Example fit for one of the Na_2CO_3/Na_2SO_4 spectra with 1.6 at% S. The strongest transition at 180.7 nm, shaded in grey, is used for calibration and has been modelled with a Voigt profile. The other two S I transitions at 182.0 and 182.6 nm are modelled with Gaussian shapes at a fixed wavelength offset from the 180.7 nm line. The weaker line of these two, at 182.6 nm, has an SNR of only 3.4 in this example spectrum. Therefore, both emission lines are mainly considered to properly assess the base line level of the major emission line at 180.7 nm.

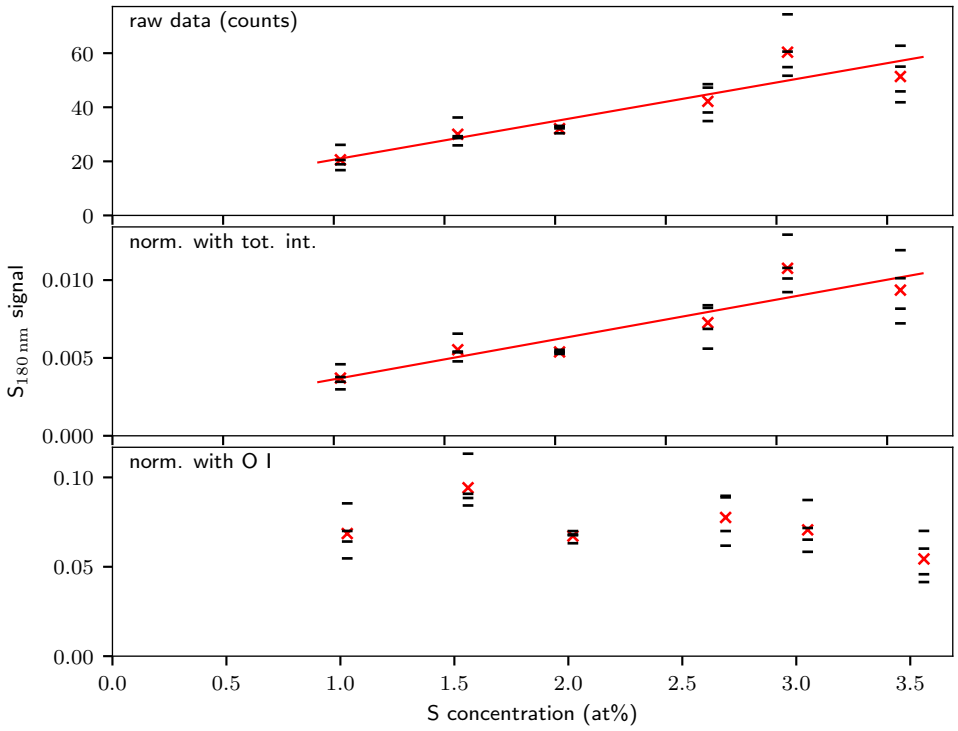

Figure 6.3: Calibration curve for Na_2SO_4 in Na_2CO_3. The red data points show the mean intensity per sample while black horizontal bars indicate the respective individual results of the four measurements. A linear regression of the means per sample is shown in red as well. The three panels refer to the raw data (top), to normalization of the data with the total intensity of the spectrum (middle), and to normalization with the O I triplet at 130 nm (bottom). In the latter case, the data no longer shows a relationship between signal intensity and concentration. Therefore, no regression has been calculated.

the sample with 0.5 at% S is missing in this figure was too low to extract and is therefore not shown. From the data, one can see an approximately linear increase of the S I emission intensity with the S concentration. The straight line is a linear regression through the mean intensities per sample with a coefficient of determination (R^2) of 0.85. Deviations of the mean intensities from the linear regression seem to be higher for the larger concentrations and higher intensities. This might, however be due to the low number of only four measurements per sample. For the sample with 3.0 at% S, for example, two of the measurements lie close to the regression line and the mean intensity for this sample is mainly increased by one outlying high value. As discussed in section 3.3, I do not expect a large variance in the local concentration for these samples, since they were prepared from fine-grained powders. The quality of the calibration curve can be measured with the root mean square error of calibration, given here as the relative deviation of the concentration predicted from the mean signal intensity per sample from the respective bulk concentration, as defined by equation (2.8) in section 2.2.1. For the presented calibration curve, RMSEC amounts to 12.4 %. This means that a concentration derived from a measured signal intensity and this calibration curve is expected to be within ±12.4 % of the unknown true concentration of the investigated sample with a confidence of 1σ.

6.2.1 Normalization

To account for fluctuations in the laser pulse energy and other factors influencing the emissivity of the plasma, two normalization approaches have been tested. They are described in more detail in section 2.2.2. In the first approach, the data has been normalized with the total intensity of the spectrum, i.e. divided by the sum of the spectral channels from 128 to 190 nm. In the case of Na_2SO_4 in Na_2CO_3, however, the total intensity is dominated by the C I emission line. The result is shown in the middle panel of Figure 6.3. For this set of data, normalization with the total intensity does not appear beneficial but neither does it have a negative influence on the

results. The R^2 of 0.84 for the linear regression is similar to the one without normalization and the data points align similarly along the calibration curve. For the highest three concentrations, the signal scatter is slightly increased, suggesting that the scatter may be of random nature or due to variations in the S concentration rather than being correlated to the total intensity. Nevertheless, due to the similar results for the means per sample the RMSEC is with 14.0 % close to the value without normalization.

The lower panel of Figure 6.3 shows the normalization with the O I triplet at 130 nm as an internal standard. This line triplet has been selected as the internal standard because of the relatively constant amount of oxygen in most sample series. In the case of the Na_2CO_3/Na_2SO_4 series the O concentration ranges from 50 to 52 %. Furthermore, this O I triplet is the only neutral emission line observed in the spectra of the lunar analogue matrices shown in the next subsections, besides the S I emission lines of the analyte. As mentioned in section 2.2.2, origination from the same ionization state is one of the key requirements formulated by Barnett et al. [63] for spectral lines to be used as an internal standard. Despite both emissions being from the same ionization state and having a fairly similar upper energy level (O $I_{130\,nm}$: 9.52 eV, S $I_{181\,nm}$: 6.86 eV [52]), normalization of the S I emission line with the O I triplet appears not suitable. A trend of signal increase with concentration is no longer evident in any form. Later investigations in the course of the chlorine study presented in chapter 7 show a decrease of the O I signal over time, which is likely the reason why a normalization approach with this particular emission feature does not succeed. This observation will be discussed in more detail in section 7.4.

6.2.2 The limit of detection

Three methods to derive the limit of detection (LOD) have been applied to the data. They are defined in section 2.2.3.

LOD_1 For the sample with 1.0 at% S, the SNR for the S I emission line at 180.7 nm ranges from 5 to 8 for the four spectra. Therefore, the line can confidently be identified in all four measurements. For the lower concentration of 0.5 at% S, the S I line can no longer be identified. The emission intensity for this sample is expected to be approximately a factor of two lower and hence the SNR would be in the order of 2.5–4.0. In summary, S cannot be reliably detected in the sample with 0.5 at% S and LOD_1 amounts to 1.0 at%. Since normalization scales all spectral channels equally, it reduces both the signal level and the noise level at the same time. Hence, the line identification potential stays unchanged and LOD_1 is independent of applied normalizations.

LOD_2 The second method, the one recommended by the International Union of Pure and Applied Chemistry (IUPAC), yields a detection limit of 0.67 at% for the non-normalized data. This value sounds reasonable, since S has been detected in all four measurements for the concentration of 1.0 at%, while it was not detectable at 0.5 at%. Thus, the detection limit should be somewhere in between, as is the LOD_2 of 0.67 at%. After normalization with the total intensity, LOD_2 is slightly lower with 0.60 at%. This is due to the slightly reduced standard deviation of the data for the three lowest concentrations, which is used as a replacement for the base line fluctuation. Keeping in mind that only four values have been used to calculate the standard deviation, which may therefore not be a good measure for fluctuations of the data, the difference in LOD_2 for non-normalized and normalized data is negligible. Since it is not possible to derive any kind of calibration after normalization with the O I triplet, there is no LOD_2 for this case.

LOD_3 The method suggested by Currie [67] takes all individual results into account and further considers that the measurement of an unknown sample to which the calibration will be applied is subject to random signal fluctuations. It therefore requires specifying a number of measurements of the unknown sample that will be conducted and averaged before inferring a concentration from the detected signal intensity. Assuming that one will take and average 15 spectra per sample, as I

	R^2	RMSEC (%)	LOD_1 (at%)	LOD_2 (at%)	LOD_3 (at%)
raw data	0.85	12.4	1.0	0.67	1.03
tot. int. norm.	0.84	14.0	1.0	0.60	1.07
O I norm.	–	–	1.0	–	–

Table 6.2: Coefficient of determination of the calibration curves, calibration error and LODs for the Na_2CO_3/Na_2SO_4 sample series before and after normalization. When normalizing the data with the O I triplet, a calibration is no longer possible and hence R^2, RMSEC, LOD_2 and LOD_3 cannot be determined.

did for the series with lunar simulant samples presented in the following sections, LOD_3 amounts to 1.03 at% before and to 1.07 at% after normalization. These results are again similar but this time the LOD without normalization is lower, thus confirming that normalization with the total intensity does not make a significant difference for these data. Furthermore, the calculated LOD_3 is close to the lowest detected concentration and hence also feasible. When expecting only four spectra per sample to be recorded and averaged, LOD_3 increases to 1.31 and 1.37 at% before and after normalization, respectively.

The results of this preliminary study are summarized in Table 6.2. Considering the low number of measurements per sample and the resulting limited certainty of the derived LODs, the results for LOD_1, LOD_2 and LOD_3 are fairly close to each other. The LOD_2 method gives the most optimistic estimate of 0.67 at% for non-normalized data. This method relies on the standard deviation of the three lowest measured concentrations. Since only four measurements per sample have been conducted in this preliminary study, the standard deviation may, however, not give a proper estimate of the expected signal fluctuation. Figure 6.4 shows the measured SNRs for the samples with 1.0 and 1.6 at% S as well as a linear regression giving an estimate of the SNR for lower concentrations. The two horizontal lines indicate an SNR of 3 and of 6, respectively, for orientation. The regression suggests that at the LOD_2 concentration of 0.67 at% the SNR will be approximately 3.2. For a method delivering highly reproducible signal levels, an SNR of 3.2 could be considered as detectable. However, since the LIBS signal tends to fluctuate rather strong, as can be seen from the four measurements per sample, the amplitude of the S I emission line could be lower than three times the noise level for some measurements of a sample with a concentration of 0.67 at% S and hence, the spectral line cannot not be reliably detected for such a sample. When extrapolating the lowest observed SNR per sample, which is only a coarse estimate due to the low number of measurements, the SNR = 3 limit is already reached at 0.83 at% S. Therefore, the LOD_2 estimate for these data is likely too optimistic and a higher LOD around 1.0 at% should be assumed, as has been derived with the methods LOD_1 and LOD_3.

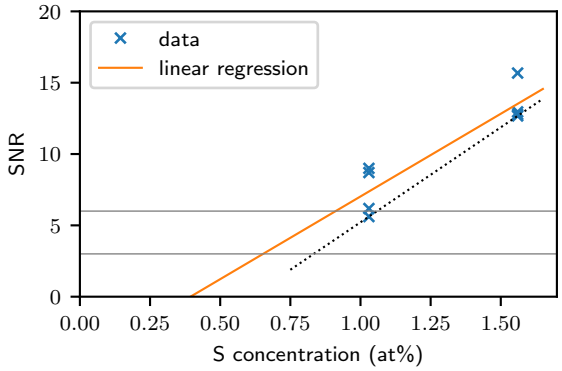

Figure 6.4: Observed SNR for the Na_2SO_4/Na_2CO_3 samples with 1.0 and 1.6 at% S. The linear regression extrapolates how the SNR reduces for lower concentrations. The dashed line gives a worst-case estimate derived from the lowest SNR of each sample. The horizontal lines mark an SNR of 6, for which a reliable detection is feasible despite signal fluctuations inherent in the method, and of 3, which is often considered as the lower limit for direct line identification. For the calculated LOD_2 concentration of 0.67 at% S, the expected SNR is only 3.2.

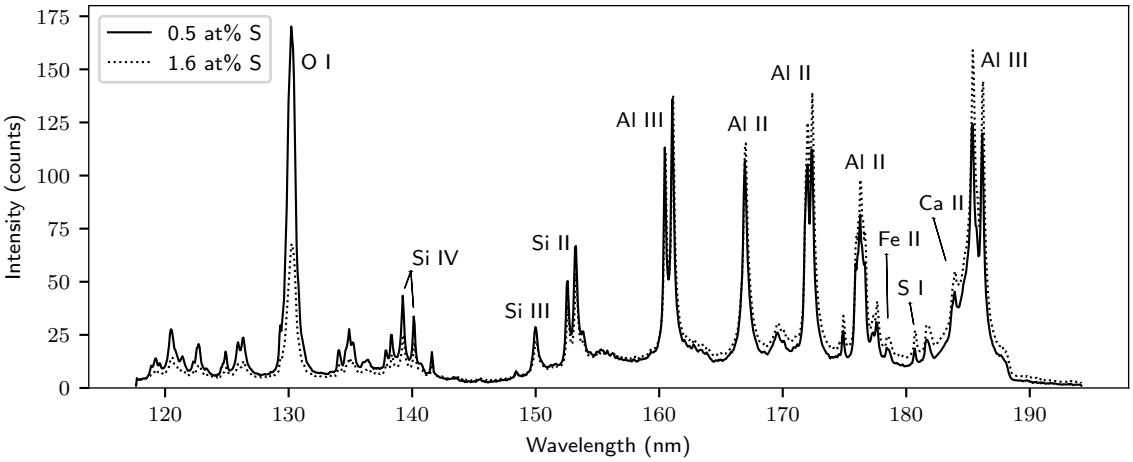

Figure 6.5: Average spectrum of the LHS/S1 samples with 0.5 and 1.6 at% S. Besides the S I emission at 180.7 nm, the O I triplet at 130 nm as well as emission lines from Si II, III and IV, and Al II and III can be seen. Ca II emission at 184 nm, on the wing of the Al III emission is evident, too.

6.3 Pure sulfur in Lunar Highland simulant

Since elemental S is available as a high-purity powder, the analyte can be mixed into the lunar simulant matrix without adding other material to the sample that is not directly related to the research question of detecting S in a lunar context. This should further allow to prepare samples with higher S concentrations while at the same time keeping the lunar simulant at $\gtrsim 70\,\%$ by weight and hence the main component of the sample. Therefore, samples with 0.5 to 8.1 at% S have been prepared.

6.3.1 The fit procedure

For the lunar simulant series, the laser pulse energy was set to 25 mJ from the beginning and hence 15 measurements could be taken per sample. The average spectra for the samples with 0.5 and 1.6 at% S are shown in Figure 6.5. The spectra exhibit mainly Al and Si emission lines from ionized species as well as the O I triplet at 130 nm. The S I emission lines around 180 nm are located between Al II and Al III emission. Except for O I, the emission lines of the matrix elements have similar intensities for both samples. The S I emission intensity is increased for the higher S concentration.

Figure 6.6 shows a close-up of the S I emission region. Additional emission lines from Ti III (181.1 nm), Si II (181.7 nm) and Al II (181.9 nm) cause spectral interference with the S I triplet. Furthermore, two emission lines from Ca II (180.7 nm) and from Si II (180.8 nm) are located in this spectral region. They are so close to the S I line at 180.7 nm that they cannot be distinguished from it. However, from measurements on pure lunar analogue I expect them to be constant and rather low in intensity. As for the sample series with the Na_2CO_3 matrix, only the strongest S I line will be used for calibration because it can still be identified at lower concentrations than can the other two S I emission lines. To evaluate its integrated intensity, it has been fitted with a Voigt profile. The five remaining lines indicated in Figure 6.6 are included in the fit as well. They are modelled with Gaussian profiles with fixed wavelength offsets to the main S I line in order to reduce the number of free parameters. Including them in the fit proved necessary to properly estimate the base line level of the S I line over the investigated range of S concentrations and to be able to use the same fit model for the LMS-based samples as well. In addition to using Gaussian shapes for the additional lines, the number of fit parameters was further reduced by setting the line width (standard deviation σ) for the additional lines to $\sigma = 0.13\,\text{nm}$, corresponding to a FWHM of 0.31 nm. This value is in accordance with the typical line width due to instrumental broadening found in section 4.3.4 and has been found to yield the best results. The width of the

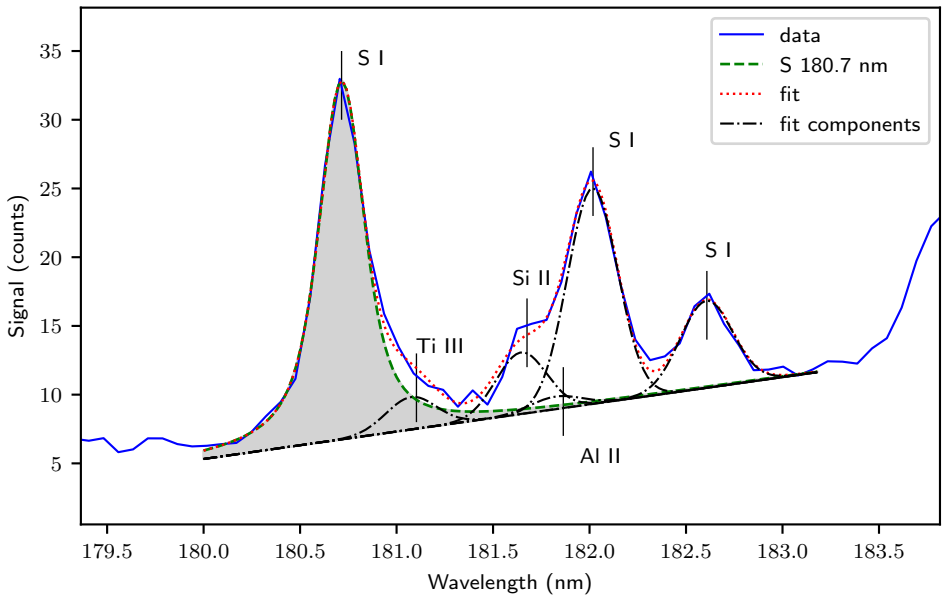

Figure 6.6: Close-up of the spectral region around the S I emission at 180 nm. The three S I emission lines are clearly visible in this example spectrum of the LHS/S1 sample with 2.5 at% S. Interfering emission from Ti III, Si II and Al II is also present. A model of six lines is fitted to the data, with the area of the most intense S I emission line, shaded in grey, being used for calibration. Two more interfering lines of Ca II (180.7 nm) and Si II (180.8 nm), both not indicated in the figure, cannot be differentiated from the S I line at 180.7 nm and will contribute to the extracted intensity. In spectra of pure LHS they have, however, been found to be fairly constant and low in intensity.

S I line at 182.6 nm, was left variable as this allowed to account for the long wing of the Al III line at 185.5 nm in some of the spectra.

6.3.2 Calibration curves

The integrated intensities of the S I line at 180.7 nm derived from fits to spectra of the LHS/S1 samples are shown in Figure 6.7 (black data). Other than for the carbonate matrix investigated before, there is no general linear trend apparent from the data. For the lowest concentrations of up to 3.1 at% S as well as for the sample with 4.1 at% S, the measured signal intensity is rather low. Around concentrations of 3.5 at% the signal intensity increases steeply with S abundance and at 6.0 at% reaches values that are about one order of magnitude higher than for 3.1 at% S. For the even higher concentrations of 7 and 8 at% S, the intensity slightly decreases. In order to confirm that this observed behaviour of the intensity is not an experimental artefact, a new set of samples named LHS/S2 has been prepared and investigated. The results of the new measurements are shown in Figure 6.7 as well (blue data). They are similar to those of LHS/S1, thus suggesting that the observed concentration-intensity relation is real.

Although the sample consists of 87 wt% lunar simulant even for the highest investigated S concentration and the matrix should therefore not be significantly altered, the reproducibility of this non-linear behaviour suggests that it is inherent in samples of S mixed in LHS. The saturation at higher concentrations could be due to self-absorption [66], which is, in general, expected to be low in vacuum owing to the low density of the freely expanding plasma but has been reported in different publications [117, 131].

For the steep signal increase beginning around 3.5 at% S, different explanations have been considered but none of them is fully consistent with the observations. Firstly, the coupling of the laser could be enhanced due to S. This would result in a larger and brighter plasma, and should therefore also increase the emission intensity of the other spectral lines. Such a gain in intensity has, however, not been observed. Another closely related explanation could be that S directly affects the matrix material on a chemical level, e.g. by reducing the dissociation energy

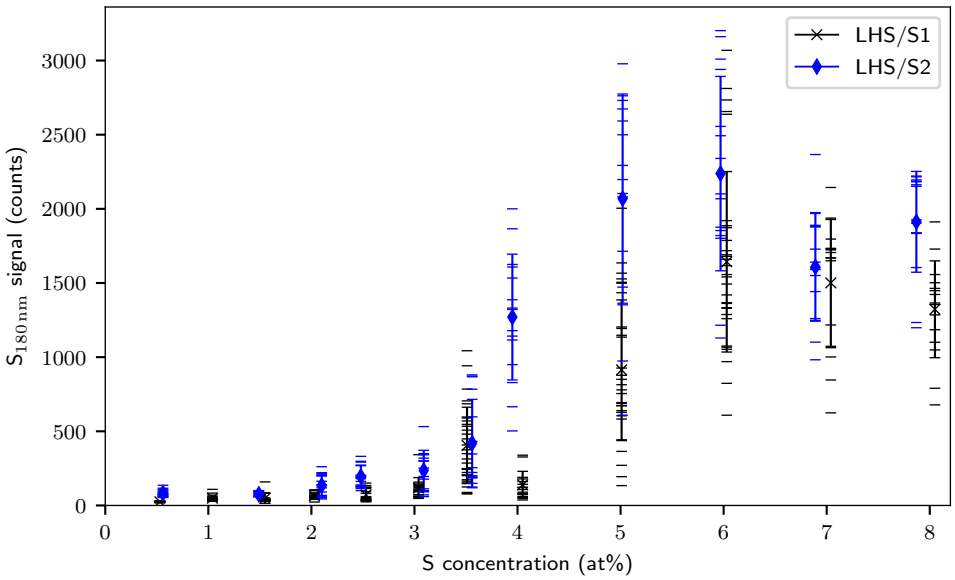

Figure 6.7: Calibration data for the two sample series LHS/S1 (black) and LHS/S2 (blue). The crosses and diamonds with uncertainty bars show the mean and standard deviation per sample while the horizontal lines indicate the results of the individual measurements. The plotted intensity is not the sole S I emission at 180.7 nm, but also contains the underlying Ca II and Si II emission from the matrix material. For concentrations higher than approximately 3 at% S, a steep increase in the signal intensity can be observed, resulting in values that are about one order of magnitude higher for 6.0 than for 3.0 at% S. For even higher concentrations, the intensity saturates and even decreases slightly. Furthermore, the intensities measured for the higher concentrations show significant fluctuations.

of the chemical bonds. This would ease the ablation of material and thereby increase the amount of ablated material in the plasma. However, if stoichiometric ablation is assumed, this should as well enhance the emission intensity of other spectral features, which has not been observed. A third option could be the selective evaporation of S. Based on an approximate laser spot diameter of 500 µm, the mean irradiance during the laser pulse is in the order of 1 GW/cm^2. Therefore, thermal processes such as melting and vaporization considerably participate in the ablation process [39]. The low boiling point of pure S (445 °C [132]) compared to that of the main component of the lunar simulant, SiO_2 (2230 °C, [133]), might result in non-stoichiometric ablation. If large grains of S are in the laser-irradiated area, the S could be evaporated before the matrix minerals and therefore make up a disproportionate fraction of the plasma species. Plasma shielding, which is typically observed in plasmas excited with nanosecond pulses and hampers further material ablation during the end of the laser pulse, could then inhibit the slower evaporation of matrix minerals [134]. While local S enrichments with diameters of up to 150 µm have been observed in the samples, see section 3.3 for details, this does not explain why the disproportionate signal increase only appears for concentrations above approximately 3.5 at% S. Furthermore, plasma shielding is expected to be reduced in low pressure atmospheres. To investigate this hypothesis, one could employ significantly higher irradiances, e.g. from picosecond or femtosecond lasers. Then, non-thermal processes would dominate the material ablation and the thermodynamic properties of the material such as the melting and boiling point are less relevant [135].

This unexplained behaviour should be investigated in a dedicated study, which may involve mixing pure S in other matrices, but on the other hand also preparing samples with higher S concentrations from molecules. For this present study about S detection in a lunar context, I will in the following focus on the lower concentration range of up to 4.0 at% S.

For this reduced range of concentrations, the data shows an approximately linear relationship for LHS/S1 with the exception of the sample with 3.5 at% S, see Figure 6.8. A linear regression with $R^2 = 0.87$ for the data of up to 3.0 at% S is shown as well. For LHS/S2, this linear behaviour is not observed; especially when considering the data point for 4.0 at% S, which lies with

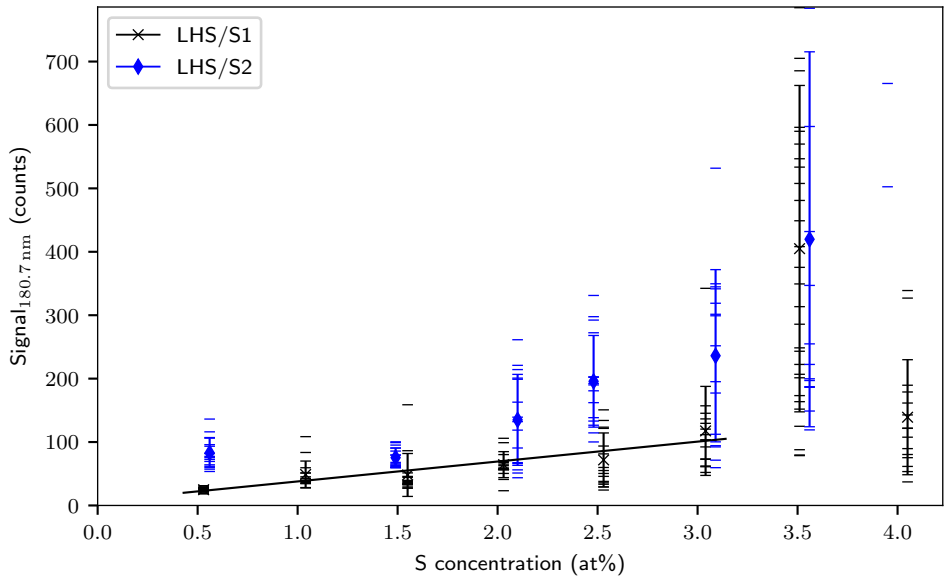

Figure 6.8: The low concentration range of the LHS/S1 and LHS/S2 calibration data. The data point for 4.0 at% S of the LHS/S2 series lies off the scale with (1270 ± 424) counts.

(1270 ± 424) counts far off the displayed scale. The uncertainty bars indicating the standard deviation per sample are relatively large compared to the mean value. The typical relative standard deviation observed here is in the range 30–60 %. These large fluctuations are probably partly due to the sample heterogeneity found during sample characterization with Raman spectroscopy in section 3.3. This is supported by the fact that the mean intensities of the LHS/S1 samples are described well by the calibration line for those lower concentrations.

The RMSEC for the established calibration is 17.6 % and therefore allows quantification within ±0.5 at% S in the limited spectral range.

6.3.3 Limits of detection

LOD_1 is based on the reliable detectability of the element in question. This includes that the intensity of an identified or fitted line can be uniquely attributed to the respective element. In the case of S in an LHS matrix, this means that the underlying emission due to Ca II and Si II needs to be separated from the S I emission. Therefore, for 14 spectra of pure LHS, the emission intensity in the range from 180.5 to 181.0 nm, where the three unresolved emission lines are located, is summed after a local background subtraction. The results range from 11.0 to 15.6 counts, with an average of 12.7 and a standard deviation of 1.35 counts. The non-integer counts are due to the linear regression used to estimate the background level, which has been evaluated at the wavelengths of the spectral channels. For certainty in detection, the integrated intensity derived in the same way, i.e. summing spectral channels, for a S-bearing sample should be higher than the mean plus three times the standard deviation of pure LHS, thus higher than 16.8 counts. For the lowest concentration sample with 0.5 at% S, this is only the case for 10 out of 15 measurements. When desiring a confidence of 90 % as it is often the case, then 14 (nominally 13.5) out of 15 measurements would need a positive test result. Hence, reliable detection is nominally not given and LOD_1 is 1.0 at%, which is the next higher measured concentration in the series and for which all 15 measurements have an integrated intensity above the threshold. Due to the observed variance in the local concentration, a reliable detection at 0.5 at% is still feasible. For the measurements with intensities below the threshold, the local concentration may have been far below the detection limit, potentially close to a local blank spot. Furthermore, four of the five below-threshold intensities amount to 15.7 counts and above, and are close to the threshold and at the same time higher than the highest detected value for the blank sample.

LOD_2 is 1.88 at%. This method is strongly influenced by the scatter of the data for the lowest

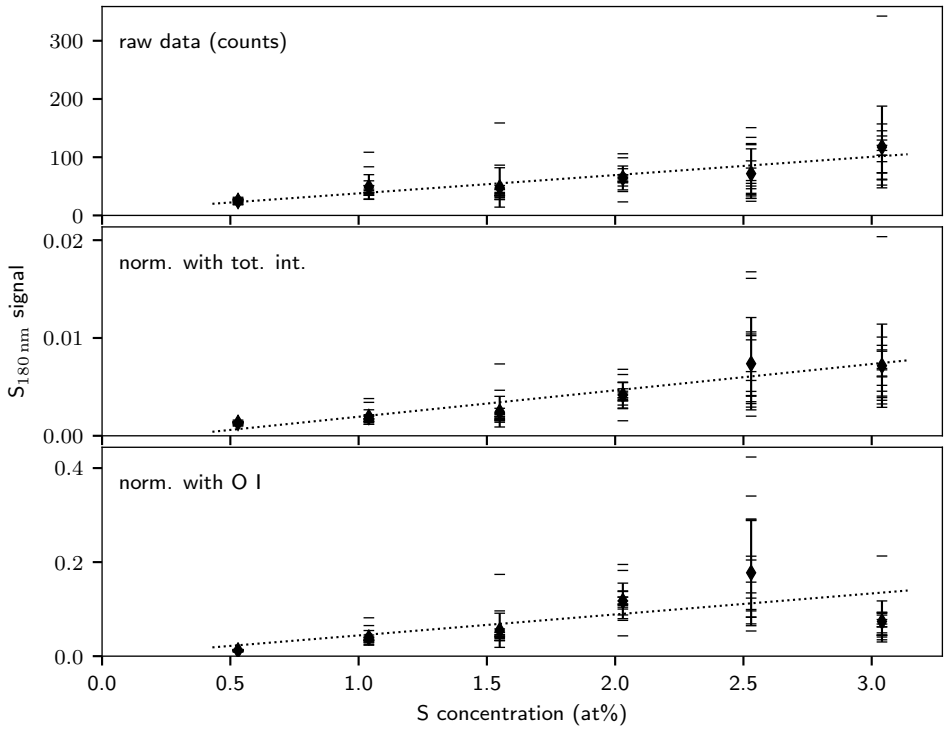

Figure 6.9: Calibration curves for the low concentration range of the LHS/S1 series after normalization with the total intensity of the spectrum (*middle*) and with the O I triplet as an internal standard (*bottom*). For comparison, the non-normalized data is shown again in the top panel.

	R^2	RMSEC (%)	LOD_1 (at%)	LOD_2 (at%)	LOD_3 (at%)
raw data	0.87	17.6	1.0	1.88	1.31
tot. int. norm.	0.90	21.6	1.0	0.91	1.11
O I norm.	0.49	38.2	1.0	1.17	1.55

Table 6.3: Coefficient of determination of the calibration curves, calibration error and LODs for the LHS/S1 sample series before and after normalization.

concentrations, in this particular case by the large standard deviation for the 1.6 at% S data point. LOD_3 is a bit more robust as it respects the scatter of all data points instead of only the lowest concentrations. For the non-normalized LHS/S1 sample series, LOD_3 amounts to 1.31 at%, assuming that 15 measurements will be averaged. Both LOD_2 and LOD_3 are based on calibration curves derived from the data. These require that the analyte concentration of the calibration samples is known. Considering the heterogeneity of the samples, the local concentration in the probed sample volume may, however, deviate from the bulk concentration. Since this local concentration in the sampling volume is not known, the bulk concentration is used for calibration. This introduces an apparent signal scatter which is not related to the LIBS method itself and thereby increases the calculated LOD. Therefore, both LOD_2 and LOD_3 are not well suited for the heterogeneous samples in this study.

6.3.4 Normalization

As for the Na_2CO_3 matrix, I tested normalization with the total intensity of the spectrum and with the O I triplet at 130 nm. The results are shown in Figure 6.9. For normalization with the total intensity, see the middle panel in the figure, the data looks similar to the non-normalized data shown in the top panel. The signal scatter for 1.0 and 1.6 at% S decreases, but it increases for 2.5 at% S. Also the mean values lie similarly close to the linear regression, resulting in a comparable R^2 of 0.90 and an RMSEC of 21.6 %. LOD_2 reduces to 0.91 at% due to the decreased

standard deviation of mainly the 1.0 at% S data point and also LOD_3 is slightly more optimistic than without normalization and amounts to 1.11 at%. In summary, total intensity normalization nominally decreases the LODs, but the quality of the calibration is at the same time reduced as indicated by the higher RMSEC, thus questioning a true benefit from normalization.

For internal standard normalization with the O I triplet, the data points for 2.0, 2.5 and 3.0 at% S move away from the calibration curve. The low R^2 of 0.49 indicates that a linear regression is not applicable for the data. This is further reflected in the high RMSEC of 38.2 %. Interestingly, only the data point at 2.5 at% S shows a significantly increased standard deviation compared to without normalization. For the other data points, the signal scatter is either similar or even reduced. This results in an LOD_2 of 1.17 at% and an LOD_3 of 1.55 at%. Table 6.3 summarizes the R^2 and RMSEC of the calibration curve as well as the three different LODs determined for the non-normalized and normalized LHS/S1 data.

6.4 Potassium and sodium sulfate in Lunar Highland simulant

To investigate the influence of the form of S provision, the two anhydrous sulfates K_2SO_4 and Na_2SO_4 have been mixed into the same lunar simulant. Since neither K nor Na emits strong lines in the VUV, the spectra look similar to the one shown in Figure 6.5 for LHS/S1. The various K II lines identified in spectra of pure K_2SO_4 in chapter 5 cannot be detected here. Accordingly, the fit procedure is the same as for the LHS/S1 and LHS/S2 series presented in the previous section. The calibration curves for non-normalized and normalized data are shown in Figure 6.10. Again, for both series a linear trend can be found in the calibration data, although it is much clearer for the LHS/Na_2SO_4 sample series. The R^2 is 0.70 for LHS/K_2SO_4 and 0.85 for LHS/Na_2SO_4. The deviating mean signal intensities in the LHS/K_2SO_4 series, especially for the sample with 2.5 at% S, lead to a high RMSEC of 30.1 %, while it is only 15.3 % for the LHS/Na_2SO_4 series.

Normalization with the total intensity of the spectrum increases the linearity of the data for both sample series and reduces the RMSEC for LHSK_2SO_4 to 22.6 %. Since the RMSEC is calculated in relative deviation from the calibration curve, the distance to the calibration curve of 87 % for the LHS/Na_2SO_4 sample with 0.5 at% S raises the RMSEC to 17.6 %, despite the increased linearity. As before, normalization with the oxygen emission as an internal standard does not appear beneficial. Despite the reduced scatter found for some samples in both series, for some other samples the scatter increases and the linearity of the data decreases in general. This is reflected in the lower R^2 of 0.63 and 0.77 and the higher RMSEC of 36.0 and 40.7 % for LHS/K_2SO_4 and LHS/Na_2SO_4, respectively. Comparing the O I normalization data of both series, one can see a factor of five difference in the normalized intensities, although the linear regression for the non-normalized data yielded almost equal parameters with $I_{K_2SO_4} = 72.6\,\text{counts/at\%} \cdot c + 12.1\,\text{counts}$, and $I_{Na_2SO_4} = 71.4\,\text{counts/at\%} \cdot c + 14.5\,\text{counts}$. Here, I denotes the detected emission intensity and c is the analyte concentration. This difference after normalization can be explained by an approximately five times lower O I emission intensity observed in the LHS/K_2SO_4 spectra. As I

	R^2	RMSEC (%)	LOD_1 (at%)	LOD_2 (at%)	LOD_3 (at%)
LHS/K_2SO_4					
raw data	0.70	30.1	0.5	1.12	1.33
tot. int. norm.	0.85	22.6	0.5	0.93	1.29
O I norm.	0.63	36.0	0.5	0.63	1.23
LHS/Na_2SO_4					
raw data	0.85	15.3	1.1	1.14	0.93
tot. int. norm.	0.95	17.6	1.1	0.83	0.72
O I norm.	0.77	40.7	1.1	1.88	1.52

Table 6.4: Calibration error and LOD for LHS/K_2SO_4 and LHS/Na_2SO_4 derived from raw and normalized data.

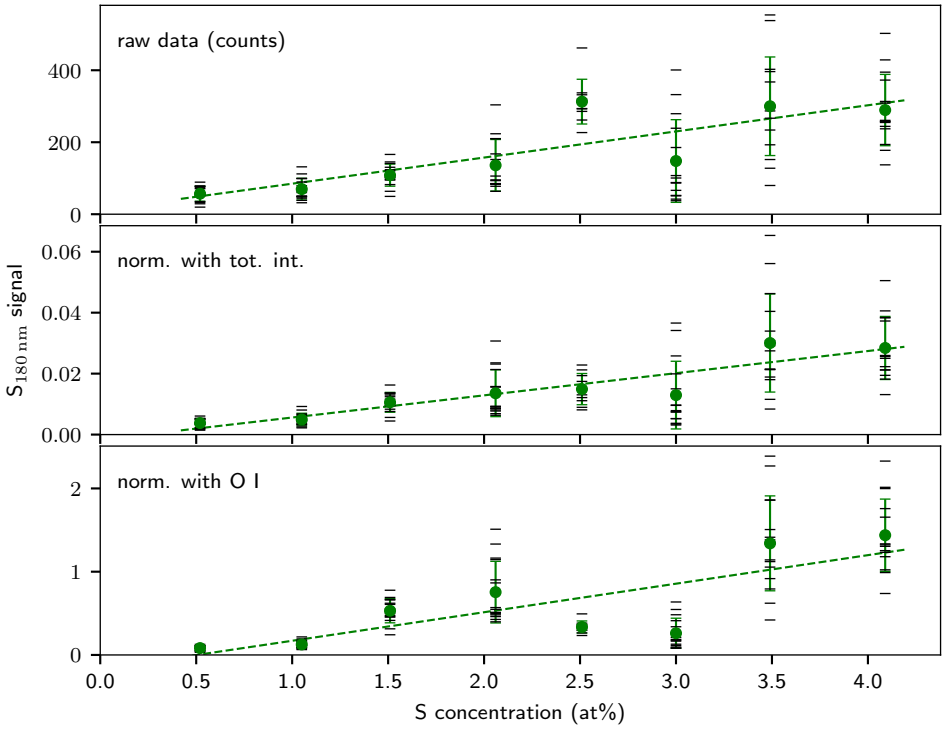

(a) LHS/K_2SO_4.

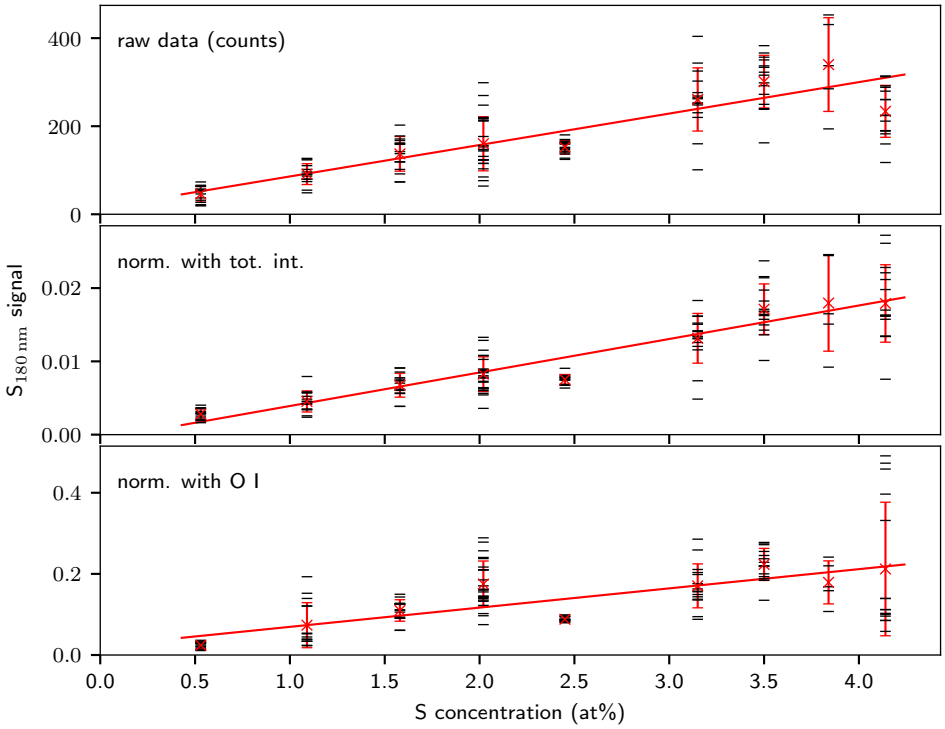

(b) LHS/Na_2SO_4.

Figure 6.10: Calibration curves for (a) K_2SO_4 and (b) Na_2SO_4 in LHS. The three panels show the non-normalized data (*top*), normalization with the total intensity of the spectrum (*middle*) and normalization with the O I triplet at 130 nm as an internal standard (*bottom*).

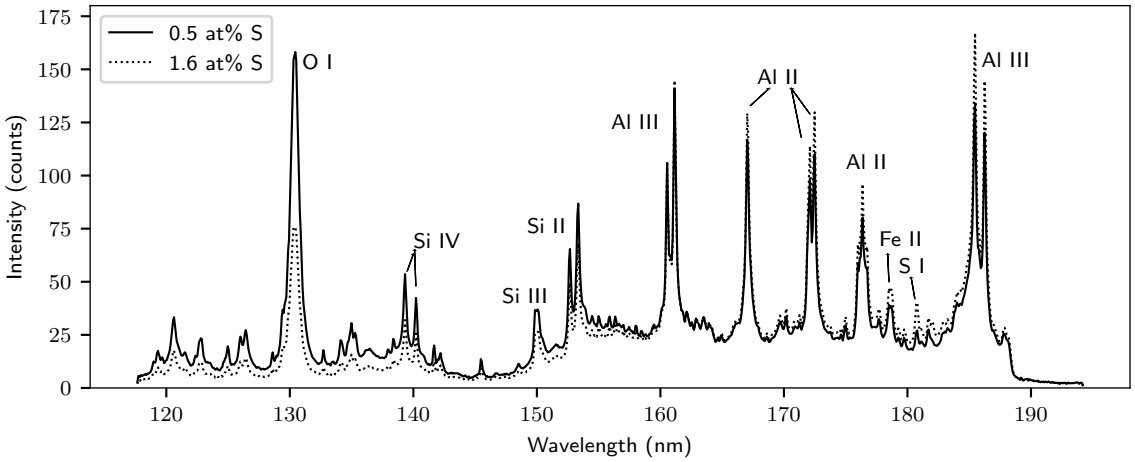

Figure 6.11: Average spectra of the LMS/Na_2SO_4 samples with 0.5 and 1.6 at% S. The spectra look similar to those of the LHS/S1 samples shown in Figure 6.5, but with a stronger Fe II signal due to the higher Fe concentration (LHS: 0.8 at%; LMS: 2.1 at%) and a weaker Ca II signal due to the lower Ca concentration (LHS: 4.4 at%; LMS: 2.3 at%). The increased S I signal at 180.7 nm for the sample with 1.6 at% S compared to the sample with 0.5 at% S can be seen.

will point out in section 7.4 in the following chapter, the difference in the measured O I intensity is likely related to experimental factors rather than to the studied sample, and the O I signal appears to generally decrease over time.

LOD_1 is 0.5 at% for LHS/K_2SO_4, as the signal threshold determined from the pure LHS sample is surpassed in all 15 spectra of the lowest concentration sample. For LHS/Na_2SO_4, on the other hand, only 12 out of 15 spectra yield a signal level above the threshold. The three too low intensities are 13.5, 15.8 and 16.1 counts. While two of these values are again close to the threshold and above the highest detected blank signal of 15.6 counts, one result is rather close to the mean signal of the blank, thus suggesting a depleted region on the sample. Since even for a probability of 90 %, which is the desired confidence defined above, there is a certain chance that only 12 out of 15 measurements yield a positive result, LOD_1 can be assumed to be at least close to 0.5 at%. Nominally, it is, however, 1.1 at%. LOD_2 is similar for both series with 1.12 and 1.14 at% before, and 0.93 and 0.83 at% after normalization with the total intensity for LHS/K_2SO_4 and LHS/Na_2SO_4, respectively. For the internal standard normalization, it is 0.63 at% for the K_2SO_4-containing series and 1.88 at% for Na_2SO_4. As mentioned before, however, the quality of the calibration after normalization with O I is reduced. Lastly, LOD_3 is with 1.33 before and 1.29 at% after normalization with the total intensity almost constant for LHS/K_2SO_4. Due to the in general higher linearity found for the LHS/Na_2SO_4 data, LOD_3 for this series is lower and amounts to 0.93 without and 0.72 at% with total intensity normalization. For completeness, the LOD_3 results for O I normalization are 1.23 at% for LHS/K_2SO_4 and 1.52 at% for LHS/Na_2SO_4. The results are summarized in Table 6.4.

6.5 Sulfur detection in Lunar Mare simulant

The lunar surface consists of two geological units: the bright Lunar Highlands, which cover the majority of the surface, and the Lunar Mare areas, appearing as dark spots when looking at the Moon [136]. In order to cover both of these units, Na_2SO_4 has also been mixed into Lunar Mare simulant (LMS). As shown in Table 3.1, LMS contains more Fe, Mg, Na and Ti than LHS. In exchange, it has lower Al and Ca concentrations. Si and O are the main constituents with similar abundances in both simulants of 15 and 60 at%, respectively. Accordingly, the spectra of the LMS/Na_2SO_4 samples are similar to those of the LHS-based samples, as can be seen in Figure 6.11 for the concentrations of 0.5 and 1.6 at% S. For data extraction, the same fit model of six emission lines is used as described in section 6.3. Due to the higher Ti concentration

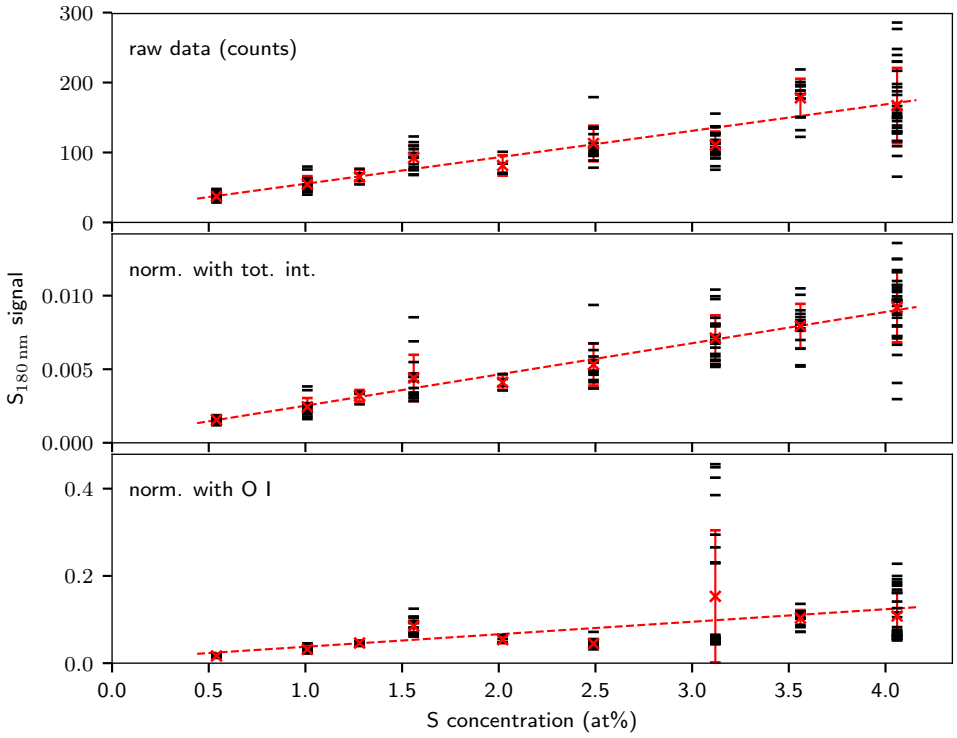

Figure 6.12: Calibration based on the LMS/Na_2SO_4 data. The three panels show again the different normalization methods.

in LMS, including the Ti III emission line at 181.1 nm in the model is now more important to correctly assess the S I emission intensity.

The fitted intensities are shown in Figure 6.12. As before, the intensity increases linearly with the concentration. Another observation is the lower signal scatter per sample in comparison to the LHS-based sample series. This can be explained by the smaller average grain size of LMS of 63 µm compared to 94 µm for LHS, which is expected to result in more homogeneous samples. Only for the sample with 4.1 at% S, the intensities of the individual measurements scatter significantly, as indicated with the black markers in Figure 6.12, thus suggesting a reduced homogeneity for this sample. However, the individual measurements scatter similarly in both directions and many of them are close to the sample's mean.

The generally higher homogeneity of the samples results in more similar standard deviations of the intensities for the different samples. Due to the lower contribution of concentration fluctuations to the standard deviation, the standard deviation of the intensity is now more specific to the VUV-LIBS method itself. This further leads to LOD_2 and LOD_3 being closer to each other with 0.72 and 0.93 at%, respectively. The RMSEC of 14.3 % is similar to the values obtained for the other sample series because it considers only the mean per sample but not the standard deviation of the signal. Since no blank sample of LMS was investigated to assess the background level in the S I emission area at 180.7 nm, the signal threshold for LOD_1 cannot be defined. Due to the lower Ca and the similar Si concentration in LMS compared to LHS, I expect the background level and therefore the detection threshold to be similar or lower than in the LHS blank sample. The lowest signal detected in the LMS/Na_2SO_4 sample with 0.5 at% S amounts to 17.2 counts and is thus above the LHS threshold of 16.8 counts. This suggests that S detection is certain in all spectra for this sample and LOD_1 is 0.5 at%.

After normalization with the total intensity of the spectrum, see middle panel in Figure 6.12, the linearity of the mean intensities is even higher, although the signal scatter of the 1.6 and 3.1 at% S sample increases. The higher linearity results in $R^2 = 0.98$, compared to 0.91 before normalization. The RMSEC as well as LOD_2 and LOD_3 decrease, too, to 8.9 %, 0.57 at% and 0.76 at%, respectively. As for all other sample series, O I normalization does not seem beneficial.

	R^2	RMSEC (%)	LOD_1 (at%)	LOD_2 (at%)	LOD_3 (at%)
raw data	0.91	14.3	0.5	0.72	0.93
tot. int. norm.	0.98	8.9	0.5	0.57	0.76
O I norm.	0.62	40.7	0.5	0.51	2.61

Table 6.5: Coefficient of determination of the calibration curves, calibration error and LODs for the LMS/Na_2SO_4 data before and after normalization.

The decreased signal scatter observed for all samples but the one with 3.1 at% S cannot compensate for the reduced linearity introduced by the normalization, which is reflected in the low R^2 of 0.62, the high RMSEC of 40.7 %, and the very different LOD_2 and LOD_3 of, respectively, 0.51 and 2.61 at%. An overview of the results for the LMS/Na_2SO_4 sample series is given in Table 6.5.

6.6 Summary

After an initial test with Na_2SO_4 in a Na_2CO_3 matrix, S from high-purity powder and S from two different sulfates has been detected in lunar analogue material. In general, the data show a linear increase of the S I emission intensity with the S concentration for up to 4 at% S from sulfates. For the pure S powder mixed in LHS, a disproportionate increase in the emission intensity above approximately 3.5 at% S has been observed. At the moment, non-stoichiometric ablation favouring the evaporation of large S grains in the sample seems the most likely explanation, although it does not fully explain the observed behaviour. Dedicated studies in the future should investigate if it is due to the high concentration of S in general or due to the unbound nature of the S from mono-elemental powder.

The heterogeneity of the samples detected with Raman spectroscopy in section 3.3 likely explains large parts of the observed signal fluctuations per sample. This is supported by a more stable signal level per sample for the series involving the finer-grained LMS. A quantitative analysis of the contribution of the sample heterogeneity to the observed signal fluctuations is not possible because the local concentrations at the locations of the LIBS measurements cannot be assessed with the present set-up.

The presented calibration curves for non-normalized data further indicate significant matrix effects, by very different signal intensities for the different sample series. Only for the similar configurations of K_2SO_4 and Na_2SO_4 in LHS, the obtained calibration curves are close to each other. These matrix effects could not be reduced by normalization with the total intensity or with the O I emission triplet at 130 nm as an internal standard. In general, normalization with the total intensity showed slight improvements by reducing the signal scatter for some samples and increasing the linearity of the data for all sample series, but not to a significant extent. The large increase in the signal scatter of some samples shows that total intensity normalization is still not necessarily beneficial and should be carefully evaluated before applying it to a data set. Normalization with the internal standard O I at 130 nm does not appear suitable for the presented data. The reason for this may, however, be an artefact of the employed instrumentation rather than a property of the emission lines themselves. This will be discussed in more detail in section 7.4 in the following chapter.

The LOD for S detection in a lunar context has been determined using the three methods defined in section 2.2.3. In most cases, LOD_2 and LOD_3 are in the order of 1.0–1.5 at%. Since the signal scatter is largely due to insufficiently homogeneous samples, especially for the LHS-based sample series, both LOD_2 and LOD_3 do not properly reflect the capabilities of the method. Using more homogeneous samples or having knowledge about the actually probed local concentration would likely result in more optimistic detection limits and an in general better calibration. Hence, the more simplistic method for LOD_1 is the best choice for these data. From the investigated

sample series, I find an LOD_1 of 1.0 at% for Na_2SO_4 in the Na_2CO_3 matrix and an LOD_1 of 0.5 to 1.1 at% for the lunar analogue matrices. Due to the confident detection of S in most of the measurements on lunar analogue-based samples with 0.5 at% S, I expect the LOD_1 to be 0.5 at% for all series involving lunar simulants. The laser-ablation spot size of the employed VUV-LIBS has a diameter of approx. 500 µm. Accordingly, negative test results for S are likely due to local depletions of S on the scale of the spot size in the course of the sample heterogeneity, and the sample volumes probed in the respective measurements may have had S concentrations far below the detection limit.

These first results show, that S concentrations below 1 at% can be detected in lunar regolith analogue material with reasonable signal-to-noise ratios for a laser pulse energy of 25 mJ, and with only little interference from matrix emission lines, when using the VUV emission line of S I at 180.7 nm. Furthermore, quantification is generally possible for concentrations below 4 at% S. Since the heterogeneity of the samples has been identified as the main source of signal fluctuations, both the detection and the quantification capabilities can be improved from the experimental side with a higher degree of control over the local S concentration in the probed volume, either by more homogeneous samples or by a spatial characterization of the samples with a reference method. Once this control is achieved, multivariate analysis techniques may yield an additional improvement of the LOD and of the RMSEC and thereby allow to assess the low S concentrations in the order of 0.1–0.2 at%, which may be encountered on the Moon [127].

However, two things should be considered before claiming a usability of VUV-LIBS for the detection of lunar S. First, lunar material is mostly loose regolith while in this study pressed pellets were analysed. Vogt et al. [137] report that a higher laser pulse energy is required for loose regolith as compared to pressed pellet samples in order to obtain an analytically useful plasma, and that the emission intensity of a LIBS plasma of loose material is lower. This suggests, that the limit of detection in a real lunar scenario might be higher. Furthermore, probing loose regolith will lead to a high shot-to-shot variability in the laser coupling, as it has been found in ChemCam data from Mars [138]. The second point to consider is that most of the lunar S occurs as troilite (FeS) and that sulfate (SO_4) minerals hardly exist on the lunar surface [110]. Measurements on a pellet-sized piece of naturally grown pyrrhotite, which is also an iron sulfide, showed a better coupling and yielded a more intense S I signal than measurements of pure S or sulfate pellets. Future studies should investigate if this higher intensity and better coupling compared to sulfates is conserved when the iron sulfide is ground to powder.

In summary, VUV-LIBS is a promising approach for the detection of S in a lunar context, but further testing is needed to confidently evaluate its suitability and some improvements of the experimental set-up may be necessary to achieve the required sensitivity.

Chapter 7

Detection and Quantification of Chlorine in Lunar Mare Analogue

Like S-bearing compounds, also Cl plays an important role in the understanding of the geochemical history of a planetary body, because it affects the stability of minerals and is believed to have participated in volcanic processes, e.g. on the Moon [28]. Therefore, the detectability of chlorine in a lunar context is investigated with VUV-LIBS. The highest Cl concentrations found in Apollo 16 samples are in the range of 200–300 µg/g [127].

To reduce influences of the sample heterogeneity observed before, only the finer-grained LMS is used for the Cl study. Furthermore, I only investigate Cl from one source, namely NaCl, since, in the previous chapter, the form of S provision did not show noticeable influences on the method itself but only on the fit coefficients, as long as the concentrations are low. Lastly, I used a slit aperture positioned slightly above the sample surface, similar to Figure 4.16c, to enhance the spectral resolution of the measurements, as explained in section 4.3.4. To compensate for the lower signal throughput caused by the aperture, the laser pulse energy was set to 40 mJ. For this series, only 12 positions per sample at a fixed distance of 1 mm have been probed. This was deemed necessary because the sample stage moves up and down during translation due to imperfect manufacturing, thereby changing the spacing between the sample surface and the lower end of the slit aperture. These variations in the spacing would lead to inconsistent masking of the plasma plume and would allow a small portion of the very intense core signal to pass the aperture for some measurements but not for the others. A stage movement of 1 mm between the measurements corresponds to two full revolutions of the actuator screw and should result in comparable masking for all recordings. Depending on the origin of this vertical movement, a linear "climbing" of the sample stage during the 25 mm long traverse might still be possible.

In the first section, I will briefly list the samples used in this study. The second section will describe the fit procedure, show the calibration curves and present the derived detection limits, followed by a discussion of the results in the third section. During the evaluation of the data, a general decrease of the shorter wavelength signals, namely the Cl I, O I and Si II emission lines in the range 125–135 nm, has been observed over time. Different hypotheses to explain these observations are discussed in section 7.4.

7.1 Samples

The samples were prepared from Lunar Mare simulant LMS-1 and reagent-grade NaCl powder with the procedure described in section 3.2. The resulting bulk concentrations are given in Table 7.1. As discussed in section 3.3, the local concentrations in the field of view of the LIBS experiment might differ for the probed locations.

Matrix	Admixture	Cl concentration (at%)
LMS-1	NaCl	1.0; 1.9; 2.4; 2.9; 3.4; 3.9; 4.4; 4.9; 10.0

Table 7.1: Overview of the samples used in this study.

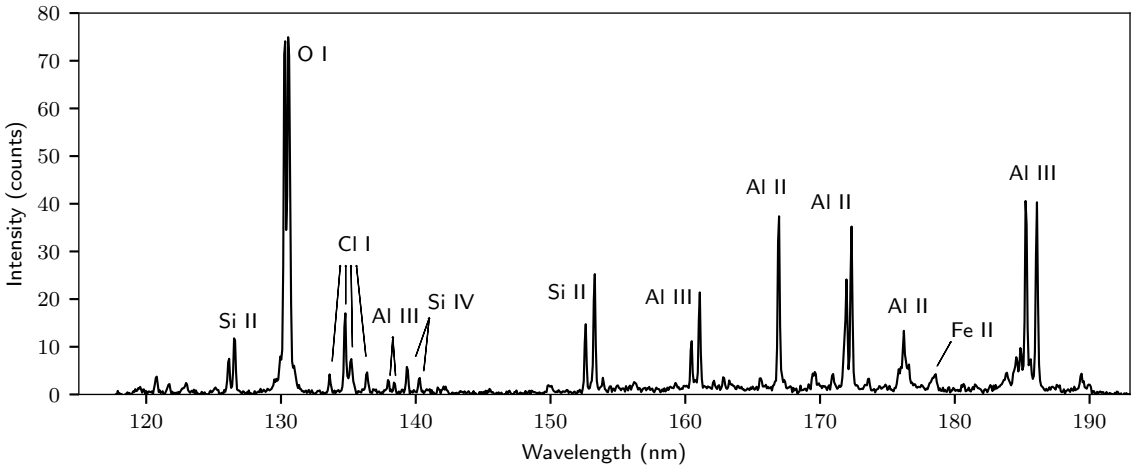

Figure 7.1: Average LIBS spectrum of the sample with 1.9 at% Cl. The four strong Cl I emission lines are located in the spectral range around 135 nm.

7.2 Results

7.2.1 Data extraction

The average spectrum of the 12 measurements of LMS with NaCl at a concentration of 1.9 at% Cl is shown in Figure 7.1. Owing to the slit aperture used in these measurements, continuum emission from the plasma core is widely suppressed and the spectral lines have a typical line width of 0.17 nm FWHM. In addition to the emission lines of the matrix elements identified in section 5 and also seen in the spectra of the LHS- and LMS-based samples of the S study in chapter 6, four Cl I emission lines are clearly evident at 133.6, 134.7, 135.2 and 136.3 nm. Further strong Cl I emission lines expected by Radziemski et al. [27] at the spectral positions 138.0, 139.0 and 139.7 nm, whose absence in their studies has been explained by absorption due to CO_2 atmosphere, are also not visible in my spectra. The Einstein coefficients for these additional Cl I transitions as well as the coefficients of the observed transitions are listed in Table 7.2. From these values, the additional lines are expected to be about two orders of magnitude lower in intensity than the most intense line at 134.7 nm. Therefore, I do not expect to detect them.

A close-up of the region with the Cl I emission lines is shown in Figure 7.2. The fit model used

λ/nm	E_u/eV	E_l/eV	g_u	g_l	A_{ul}/s^{-1}
133.573	9.28	0.00	2	4	1.74×10^8
134.724	9.20	0.00	4	4	4.19×10^8
135.166	9.28	0.11	2	2	2.23×10^8
136.345	9.20	0.11	4	2	7.50×10^7
137.953	8.99	0.00	4	4	1.10×10^7
138.996	9.03	0.11	2	2	1.70×10^6
139.653	8.99	0.11	4	2	1.50×10^6

Table 7.2: Spectroscopic constants of the Cl I lines between 130 and 140 nm [52]. λ: wavelength; E_u and E_l: energy of upper and lower level; g_u and g_l: degeneracy of upper and lower level; A_{ul}: Einstein coefficient for spontaneous emission.

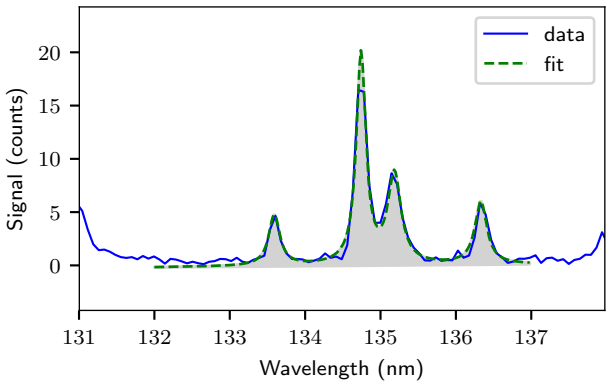

Figure 7.2: Fit example for a spectrum of the 1.9 at% Cl sample. The four Cl I emission lines at 133.6, 134.7, 135.2 and 136.3 nm are modelled as a set of four Lorentzian line profiles with fixed integrated intensity ratios.

	relative intensity	
λ/nm	measured	expected
133.573	1	1
134.724	3.50	4.80
135.166	2.05	1.29
136.345	1.31	0.86

Table 7.3: Measured and expected intensity ratios of the Cl I lines. The expected intensity ratios have been calculated from the spectroscopic constants listed in Table 7.2.

here to extract the Cl emission intensity is composed of four Lorentzian profiles. The wavelength separation between the lines is set to the values given in the NIST atomic spectra database [52]. The intensity ratios between the four emission lines were found to be similar throughout all spectra in the series, except for those related to the lowest concentration sample, where it was difficult to fit the model to the data. Thus, the ratios of the integrated intensities are set to the average values found in a first fit iteration. The line widths are kept variable but typically result in 0.11–0.15 nm FWHM. This rather uncommon approach of fixing the area instead of the line width was chosen because the four transitions originate from two closely spaced energy levels. For the each two lines originating from the same level, the emission intensity ratio is purely determined by the Einstein coefficient and should therefore be constant. Since the two involved upper energy levels are very close with a difference of 80 meV compared to the 9.2 eV excitation energy, even without LTE the population should be similar. Thus, the ratios among all four emission lines are expected to be constant, in agreement with the observation, although the ratios differ from those expected from the spectroscopic constants found in spectral data bases, see Table 7.3, which is likely due to uncertainties of the Einstein coefficients. The line width, on the other hand, is strongly affected by different mechanisms, such as Stark-broadening, Doppler-broadening and instrumental broadening. In section 4.3.4, the latter has been found to depend on the geometry of the plasma plume. Although this spatial influence has been reduced with a slit width, it was not possible to set a width for each line as well.

Underlying Si II and Si III emission from 14 potentially interfering emission lines is hardly evident in the spectra for $\geq$1.9 at% Cl. For the sample with 1.0 at% Cl, in 7 out of 12 spectra only the strongest Cl I line at 134.7 nm can be recognized, superimposed on another spectral feature. Due to the high number of Si lines, they cannot be incorporated in the fit model individually. A spectrum of the region simulated with the algorithm described in section 2.1.3 shows that the Si emission lines form three groups centred around 134.2, 135.0 and 136.4 nm for Si III, Si II and Si III, respectively. It is shown in Figure 7.3. The simulation parameters were $T_{\mathrm{init}} = 25\,000$ K, $n_e = 1 \times 10^{23}\,\mathrm{m}^{-3}$, and a Cl/Si ratio of two. The limited applicability of LTE simulations for time-integrated vacuum plasmas is directly evident from the figure: For the correct Cl/Si ratios in the range 0.07–0.33, the Si emission lines would be on average a factor of 20 higher than

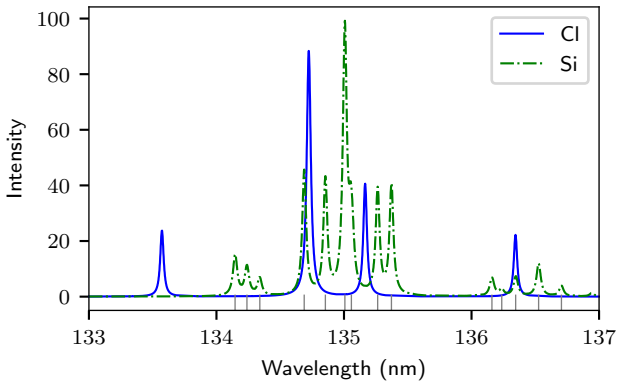

Figure 7.3: Simulated spectra of Cl and Si in the spectral range 133–137 nm. The start temperature for the simulation was set to $T_{\text{init}} = 25\,000$ K, the electron density to $n_e = 1 \times 10^{23}\,\text{m}^{-3}$. Si emission occurs in three groups of lines: Three lines of Si III around 134.2 nm, six lines of Si II around 135.0 nm and 5 lines of Si III around 136.4 nm. The positions of the 14 Si lines are indicated below the curves.

the Cl emission lines. When trying to correct for this with a lower initial electron temperature in the order of 15 000 K, Si III emission vanishes. While this would be in accordance with the observations in this spectral region, it does not explain the observation of the Si IV emission lines around 140 nm in Figure 7.1. In an attempt to account for the Si emission in the spectra when fitting the Cl signal, the three groups have been modelled as compositions of three, six and five Lorentzian lines, respectively, with fixed intensity ratios within the groups as expected from Einstein coefficients [52]. With the additional three fit parameters for the group emission intensities, however, the extracted Cl signal is almost unchanged. Therefore, the Cl signal used in the following for univariate calibration is derived from the fit model described first, disregarding the potentially underlying Si emission.

7.2.2 Univariate calibration and normalization

The intensities extracted from the fits to the spectra are shown in Figure 7.4 as a function of the Cl concentration. The top panel shows the raw data as extracted from the fit. When disregarding the data from the sample with 4.4 at% Cl, one can see a more or less constant signal increase with Cl concentration, though with considerable scattering. Similar to the sulfur study shown in chapter 6, normalization of the data with the total intensity of the spectrum as well as with an internal standard, namely the O I emission at 130 nm, has been tested. For the latter, the signal was additionally scaled with the bulk atomic fraction of O, since the O concentration drops from 59.2 at% (1.0 at% Cl) to 47.5 at% (10.0 at% Cl) throughout the sample series. Normalization with the total intensity of the spectrum, see the second panel of the figure, brings the data points closer together but still shows noticeable deviations. R^2 increases from 0.39 without normalization to 0.65. When the data is normalized with the intensity of the O I emission triplet, see Figure 7.4 bottom, a highly linear relationship with $R^2 = 0.96$ is evident, even including the data point at 4.4 at% Cl and the highest concentration at 10.0 at% Cl.

7.2.3 Limits of detection

As for the sulfur study, the three different LODs defined in section 2.2.3 are determined. The lowest investigated concentration was 1.0 at% Cl, and for this sample at least the Cl I line at 134.7 nm could be identified in all spectra with an SNR > 10. Hence, an LOD_1 of 1.0 at% Cl can be stated. The predictive estimates of reliably detectable concentrations, LOD_2 and LOD_3, are less optimistic due to a large variance in the data. For the raw data and for total intensity normalization, they are in the order of 4–7 at%, while they are around 3.5 at% after normalization with the O I triplet at 130 nm. The exact values are summarized in Table 7.4.

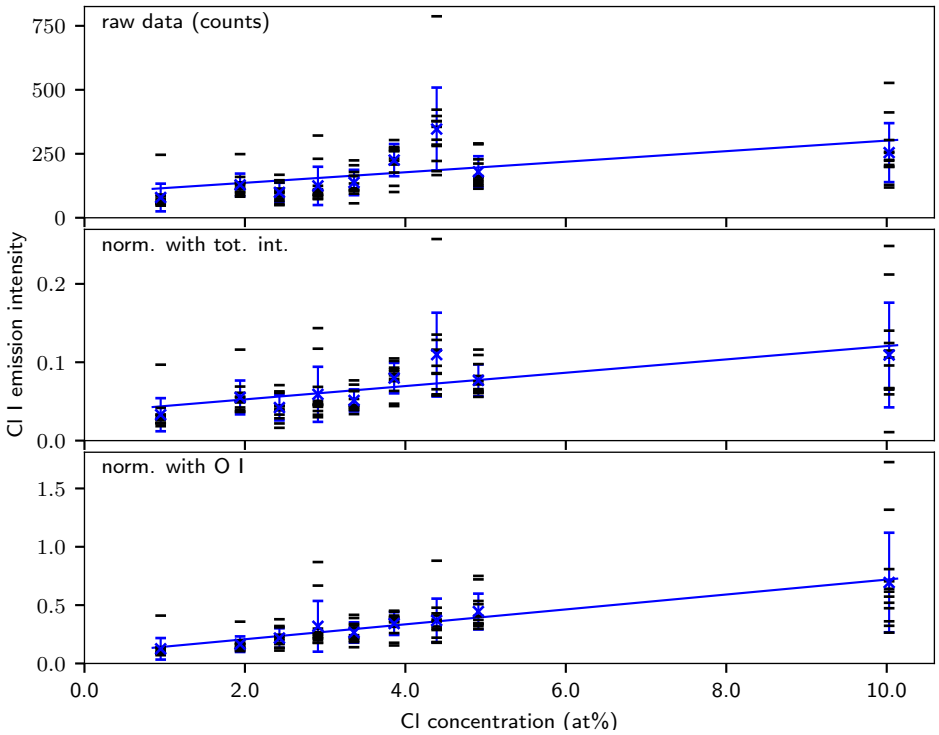

Figure 7.4: Univariate calibration curves for the untreated and normalized data of the LMS/NaCl sample series. The blue crosses with uncertainty bars show the mean and standard deviation of the 12 measurements per sample, which are indicated as black horizontal bars. *Top:* Raw intensities directly extracted from the fit *Middle:* Data normalized with total intensity of the spectrum *Bottom:* Normalization with O I triplet at 130 nm as internal standard, respecting the reduced O abundance for higher Cl concentrations.

	R^2	RMSEC (%)	LOD_1 (at%)	LOD_2 (at%)	LOD_3 (at%)
raw data	0.39	96.0	1.0	6.58	5.37
tot. int. norm.	0.65	62.8	1.0	6.96	4.64
O I norm	0.96	18.4	1.0	3.80	3.12
Si II norm	0.96	18.9	1.0	4.69	3.13

Table 7.4: Coefficient of determination of the calibration curves, calibration error and LODs for the Cl-bearing sample series before and after normalization.

7.3 Discussion

Despite the low sensitivity at the short wavelength end of the spectrometer's operating range, the Cl I emission lines around 135 nm are clearly evident already at low concentrations in the order of a few percent molar fraction. The signal intensity, however, scatters significantly between different spectra from the same sample, which is reflected in the uncertainty bars of the calibration curve shown in Figure 7.4 (top panel). The contribution of the sample heterogeneity to the scatter is expected to be lower than for the S-bearing LHS samples investigated in section 3.3, due to the smaller grain size of the LMS matrix. A look at the individual data points shown in the same figure reveals that the large uncertainty bars drawn to the calibration curve are often due to one or two measurements per sample that result in a far higher intensity than the other measurements for the same sample. This could likely be due to a larger NaCl grain in the area of the laser spot. As pointed out in the previous chapter, the quality of the calibration depends strongly on the homogeneity of the sample. In order to be able to decouple signal fluctuations introduced by the method itself from uncertainties in the local concentration, one would need to assess the local concentrations at the probed locations with a second reference method. This is, however, not feasible with the current instrumentation.

Species	λ/nm	E_u/eV	$E_{ion,I}$/eV	$E_{ion,II}$/eV
Cl I	134.7	9.2	13.0	23.8
O I	130.2	9.5	13.6	35.1
S I	180.7	6.9	10.4	23.3
Si II	126.4	9.8	8.2	16.3

Table 7.5: Spectroscopic constants for the analyte transitions from S I and Cl I, as well as for the internal standard transitions from O I and Si II [52]. λ: wavelength; E_u: upper energy level; $E_{ion,I}$ and $E_{ion,II}$: first and second ionization energy. Only the data for the strongest line of each group is presented.

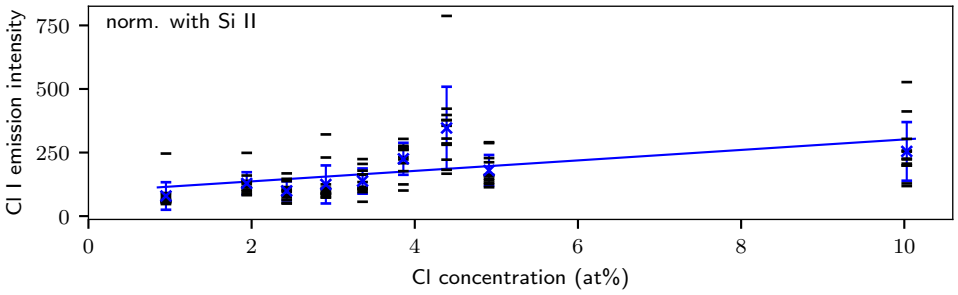

Figure 7.5: Cl I signal normalized with the Si II doublet at 126 nm. As for O I normalization, the mean signal intensity per sample aligns well on a straight calibration line. This suggests, that something affects the short wavelength end of the spectrum around 130 nm and thereby prevents calibration with the non-normalized data.

Similar to the sulfur-related results in chapter 6, normalization with the total intensity of the spectrum has only little influence on the signal scatter per sample, but slightly increases the linearity of the calibration. Surprisingly, normalization with the close-by O I triplet at 130 nm shows significant improvement in terms of linearity and for most samples also regarding the signal scatter, while it was not beneficial for any of the S-based sample series presented in chapter 6. A look at the O I signal in the S-based samples shows a high variance, with a factor of up to 5–8 between different samples, despite the similar O concentrations of (59 ± 2) at% for all samples. The reduced scatter and high linearity seen here in Figure 7.4 (bottom) for O I normalization suggests a systematic effect, influencing both O I and Cl I emission in a similar way. While this is exactly what a normalization is expected to correct for, the failure of O I normalization in the sulfur studies indicates that it is not universal.

Two of the most important criteria for internal standard normalization identified by Barnett et al. [63] are that the analyte and the internal standard have a similar ionization energy and state, and that both the analyte emission line and the internal standard emission line involve upper energy levels of a comparable energy. As shown in Table 7.5, these criteria are better fulfilled for normalization of Cl I with O I than for S I and O I. Therefore, one could expect a positive influence of O I on the chlorine data but not for sulfur. However, since the calibration curves for the sulfur-based series were already good without normalization and became partly useless after normalization with O I, e.g. for the Na_2CO_3 matrix, there is likely a different key factor of influence to consider.

To test how strict the criteria formulated by Barnett et al. [63] are, the data is additionally normalized with the Si II lines at 126 nm. Originating from an ionized species, it should expectedly be less suitable for normalization of a neutral emission line. Furthermore, the first and second ionization energy of Si are significantly different from those of Cl, O and S, as listed in Table 7.5. Only the excitation energies of the Cl I and Si II transition are comparable. The calibration curve for the LMS/NaCl data after normalization with Si II is shown in Figure 7.5. The results are similar to those obtained by O I normalization: The data becomes more linear and for many samples the signal scatter reduces. This is as well reflected in the figures of merit and the LODs listed in Table 7.4. R^2, RMSEC and LOD_3 are almost the same as for O I normalization, while LOD_2 is increased. This similarity between O I and Si II normalization suggests that the deviations observed in the non-normalized Cl data are rather an effect of the spectral

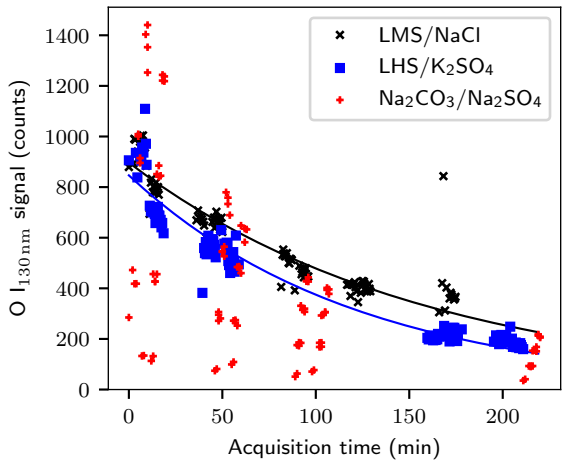

(a) O I emission at 130 nm

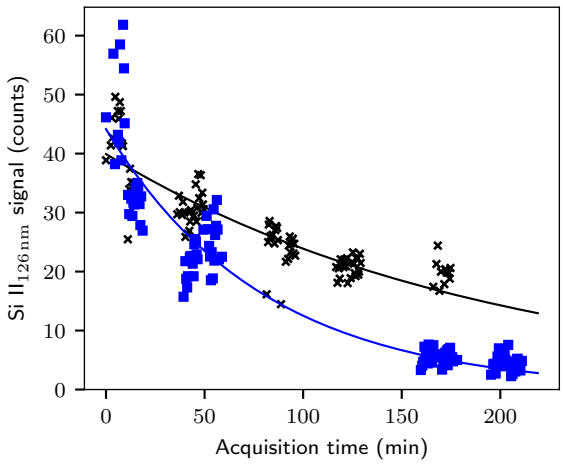

(b) Si II emission at 126 nm

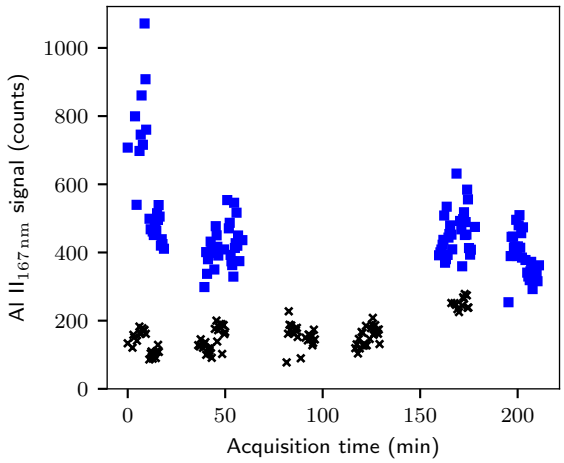

(c) Al II emission at 167 nm

Figure 7.6: Temporal drift of short wavelength emission line strengths from O I at 130 nm (a) and Si II at 126 nm (b) over the measurement session for the Cl-bearing LMS/NaCl samples (black crosses) and, for comparison, for the LHS/K_2SO_4 sample series (blue squares). For both emission lines, an intensity decrease over time is evident, suggesting a potential loss in sensitivity. The longer-wavelength emission of Al II at 167 nm (c) is not affected by this decrease. The values have been scaled with the bulk O, Si and Al concentration of the respective sample. A series of samples with Na_2SO_4 mixed in Na_2CO_3 (red crosses) shows a similar decay for the O I signal but with several data points randomly scattered. The black and blue solid lines are exponential fits to the data of LMS/NaCl and LHS/K_2SO_4, respectively.

region than of the LIBS process itself. An analysis of the temporal behaviour of the O I and the Si II signal over the measurement session reveals a monotonic decrease of the detected intensity for the LMS/NaCl sample series. This may likely influence the Cl I signal as well, but is less evident there due to the varying concentration. Potential reasons for this signal decrease are discussed in the following section.

7.4 Decrease of short wavelength signals over time

When sorting the O I signal used for normalization by the acquisition time, a monotonic decay becomes visible, see Figure 7.6a (black crosses). A similar behaviour can be observed for the close-by Si II lines (Figure 7.6b), which have been used for Cl I normalization as well. Moreover, the same decay occurs for the LHS/K_2SO_4 sample series (blue squares), for both O I and Si II. By contrast, the emission intensity of Al II at 167 nm is almost constant over time within both

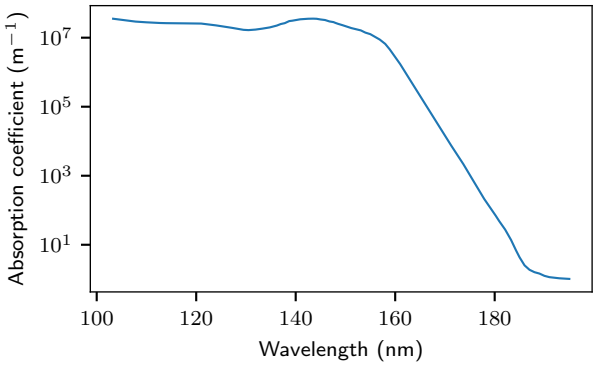

Figure 7.7: Optical absorption of water ice at −7 °C in the VUV spectral range. The data has been taken from Warren [141].

series, as shown in Figure 7.6c. The other S-bearing sample series indicate a similar behaviour but are not shown here, because the data of these series has been collected on multiple days per series. Furthermore, the same general trend is found for the samples from section 6.2 with varying amounts of Na_2SO_4 mixed in Na_2CO_3 (red crosses), although the O I signal scatters a lot more between the different locations per sample. The three sample series shown in Figure 7.6 have been measured on different days.

A likely explanation for wavelength-dependent intensity variations are losses due to absorption along the optical path. Especially in the deep- and vacuum-UV, these can occur at a significant scale [139]. Absorption is wavelength-dependent and could therefore strongly affect Cl I, O I and Si II emission in the 130 nm range while leaving the Al II emission lines at 167 nm and the S I emission lines at 181 nm unchanged. In air, most of the VUV absorption is due to oxygen (O_2) and water (H_2O), but it seems unlikely that absorption is taking place in the residual atmosphere due to the low operating pressure of the system of less than 10^{-2} Pa. For O_2 from ambient air to show noticeable absorption ($\leq$95 % transmission) along the 80 cm long optical path, a pressure of $\geq$1 Pa is required [93]. Water (H_2O) vapour, which is likely another large constituent of the residual atmosphere and may as well be desorbed from the sample surface and the walls of the vacuum chamber, also has an in general high absorption coefficient in the region around 130 nm but is negligible below 10 Pa [140]. The release of H_2O adsorbed by the sample and the formation of O_2 from ablated sample material are also negligible due to the low ablated mass in the order of 100 ng per laser pulse [21]. Moreover, the comparison of the LMS/NaCl and the LHS/K_2SO_4 data in Figure 7.6a suggests that the signal reduction over time is independent of the actual LIBS measurement itself, since the LHS/K_2SO_4 data follows the same trend as the LMS/NaCl data despite a large time gap in the acquisition time where no LIBS measurements were made. Hence, it does not seem to be related to the ablation process.

For the reasons noted above, the most likely explanation of the observed behaviour is the desorption of H_2O from the walls of the vacuum system over time. While the concentration of this desorbed H_2O in the system is too low to cause significant absorption, it could come into contact with the cooled detector and deposit on its surface. In this way, it naturally accumulates on the optical path and forms a thin film of ice. Due to the high absorption coefficient of H_2O ice of more than 10^7 m^{-1} at wavelengths shorter than 150 nm, see Figure 7.7, an ice layer of 50–100 nm forming during the 3 h of the measurement session would be sufficient to explain the observed signal decrease. At wavelengths of 170 nm, the absorption coefficient is already four orders of magnitude lower, which would explain why the Al II and S I emission lines at 167 and 181 nm, respectively, are not affected by such an ice layer.

For a linear growth of the ice layer, one would expect an exponential decrease of the signal intensity. Therefore, the exponential function $y = A_0 \cdot \exp(-x/\tau)$ has been fitted to the O I and Si II intensities in Figure 7.6. The results are summarized in Table 7.6. Except for the first measurements, this exponential fit is a good description of the signal decrease. The quicker

Series	Line	A_0 (counts)	τ (min)	Growth rate (pm/s)
LMS/NaCl	O I	897	159	6.32
LMS/NaCl	Si II	39.9	194	4.22
LHS/K_2SO_4	O I	846	123	8.20
LHS/K_2SO_4	Si II	44.1	79.3	10.3

Table 7.6: Fit coefficients for the temporal behaviour of the O I and Si II signal intensities at 130 and 126 nm, respectively. The employed fit model is an exponential decay of the form $y = A_0 \cdot \exp(-x/\tau)$. The growth rate of the ice layer has been calculated from the time constant τ and the absorption coefficient from Figure 7.7 at the respective wavelength.

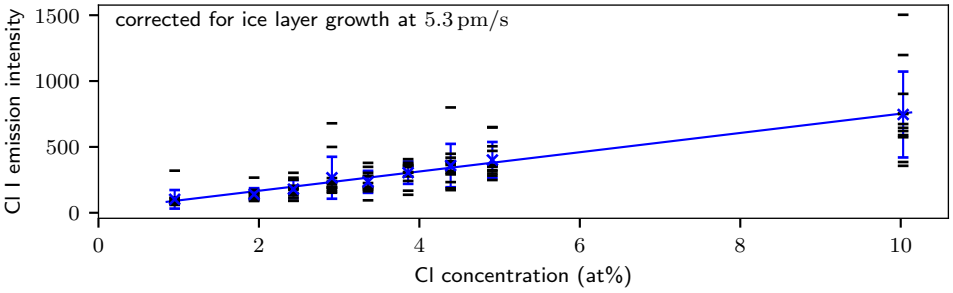

Figure 7.8: Cl I calibration data corrected for temporal loss in sensitivity due to the forming of an ice layer on the detector. The Cl I emission intensity presented in Figure 7.4 (top) has been scaled with a sensitivity factor according to the expected thickness of the ice layer at the time of acquisition. The linearity of the resulting data is similar to that which is obtained by normalization with O I, cf. Figure 7.4. R^2: 0.99; RMSEC: 11.1 %; LOD_2: 2.54 at%; LOD_3: 2.17 at%.

decrease in the beginning of the measurement session might be explained by an initially high supply of H_2O from the atmosphere, while at a later stage H_2O is continuously provided through desorption from the walls at a lower rate. From the time constant τ and the absorption coefficient of H_2O ice at the O I and Si II emission wavelength, the fit results can be converted into growth rates of the ice layer. The results are summarized in Table 7.6. The four derived growth rates all have the same order of magnitude of a few picometres per second. Such low thicknesses are realistic to be achieved when concentrating the water of all interior surfaces of the vacuum system on the detector. Another observation supporting the hypothesis of an ice layer forming on the detector is that the growth rates derived from the LHS/K_2SO_4 sample series, which has been measured with a detector temperature of −80 °C, is higher than the growth rate determined for the LMS/NaCl series, which has been measured at −60 °C.

With the average growth rate of the ice layer during the LMS/NaCl measurement of 5.3 pm/s and the absorption coefficient at 135 nm of $1.99 \times 10^7\,\mathrm{m}^{-1}$, the reduced sensitivity for the Cl I emission can be considered in the calibration curve. Figure 7.8 shows the raw data scaled with the time-dependent relative sensitivity expected from the linear ice layer growth. The data is now highly linear with an R^2 of 0.99. Also the RMSEC as well as LOD_2 and LOD_3 are reduced to 11.1 %, 2.54 at% and 2.17 at%, respectively, which is lower than for any other tested normalization, cf. Table 7.4.

Despite specific precautions to avoid the desorption of H_2O from the walls during the measurements, such as letting the turbomolecular pump at the spectrometer run for several days before the measurement and backfilling the system with N_2 before stand-by times, the hypothesis of water ice on the detector is consistent with all observations and therefore the most probable explanation. In order to conclusively determine that it is the correct explanation, a stable VUV continuum source, which is currently not available, could be placed behind the sample holder. Measurements of its emitted radiation throughout a day, with and without laser-ablation, would then allow to deduce a spectral profile of the losses. From the shape of the loss profile with potential maxima and gaps one might be able to identify spectral patterns that give insight into the relevant processes, which cause the observed decrease in sensitivity. If it is indeed the case

that H_2O deposits on the detector, a dedicated cold trap should be installed in the vacuum pipes to capture this residual H_2O in future measurements, not only to enhance the analytical capability of the system but also to protect the sensor from damage.

7.5 Summary

For chlorine detection, samples of NaCl mixed into LMS with Cl concentrations ranging from 1.0 to 10.0 at% have been investigated. The strong Cl I emission lines at 133.6, 134.7, 135.2 and 136.3 nm identified in the NaCl spectrum in chapter 5 are evident in all recorded spectra for concentrations $\geq$1.9 at% Cl. For the lowest concentration of 1.0 at% Cl, only 5 out of 12 spectra show all four Cl I lines, while in the remaining 7 spectra only the most intense emission line at 134.7 nm can be recognized. Since this emission line still has an SNR > 10 in all spectra, chlorine can be reliably detected at concentrations as low as 1.0 at%. Underlying Si II and Si III emission between 134 and 137 nm from the lunar simulant matrix, which is expected to have a measurable intensity according to simulations, cannot be observed for concentrations of 1.9 at% Cl and above.

Calibration curves established from the data show large discrepancies between the data and the linear regression, resulting in a calibration error of 96 % and an LOD_2 and LOD_3 in the order of 6 at% for non-normalized data. The calibration improves slightly upon normalization with the total intensity of the spectrum, but is with a calibration error of 63 % still not suitable for quantitative analyses.

Opposite to the sulfur study in chapter 6, O I normalization yields a significant improvement of the calibration data with an R^2 of 0.96 and a calibration error below 20 %. A similar improvement of the calibration is found for internal standard normalization with Si II, despite the different ionization state of the analyte and the internal standard.

The lack of linearity in the non-normalized data, which can be compensated by normalization with O I or Si II, can be explained with a general decrease of the signal intensity over time for short wavelength transitions. With the current knowledge, the most probable explanation for this behaviour is that water, which is desorbed from the walls of the vacuum chamber, deposits on the cooled detector. A thin ice layer of up to 100 nm would be enough for efficient absorption of the radiation. An exponential fit to the signal decrease of the O I and Si II emission in combination with the absorption coefficient of water ice allows to derive a growth rate of the suspected ice layer of about 5 pm/s. A correction of the Cl I emission intensity with the temporally increasing absorption due to such an ice layer results in linear calibration data with figures of merit better than for any other normalization tested for the LMS/NaCl series. To finally confirm this theory, a broadband VUV source is necessary that would permit a controlled investigation of the wavelength-dependent signal decrease over time. Alternatively, a dedicated cold trap could be placed in the vacuum chamber in order to determine whether this resolves the problem.

Chapter 8

Conclusion

The aim of this thesis was to investigate the usability of VUV-LIBS for in-situ planetary exploration on celestial bodies without an atmosphere, setting a focus on chemical elements that are challenging to detect with conventional LIBS in the UV to NIR spectral range. For this task, a new VUV-LIBS set-up, which covers the detection range 100–200 nm, was designed and built at the DLR-OS institute in Berlin.

In the first part of this thesis, the design and characterization of the VUV-LIBS set-up were reported. Two of the main results of the characterization are the estimate for the relative sensitivity and the identification of the dominant broadening mechanisms. The relative sensitivity has been estimated by comparison of simulated and measured emission intensities of the three most suitable Si II line pairs. Although the results are subject to large uncertainties due to the simplifying approximations made for the simulation, the data suggest that the sensitivity of the set-up at 126 nm is at least two orders of magnitude lower than at 180 nm. Concerning the spectral line broadening, I found a large instrumental contribution in addition to Stark broadening due to the high electron density in the plasma centre during plasma initiation. From measurements with a fibre-coupled mercury lamp, I found that the positions of the spectral lines on the detector depend on the position of the light source. For an extended light source such as the LIBS plasma, the emission lines are detected on multiple detector positions at the same time and therefore appear broadened. The instrumental broadening can be significantly reduced by installing an aperture close to the sample, which effectively creates a more defined source comparable to the fibre-coupled mercury lamp. While this would not be an option for a space instrument, I expect a similarly increased performance for an optimized optical layout. Future iterations of the set-up used in this thesis could be improved by replacing the OAP with a toroidal mirror with an appropriate coating. In general, the results confirm that the employed optics have a strong influence on the sensitivity of a VUV the set-up and should therefore be carefully selected.

In the second part, I used the VUV-LIBS set-up to identify spectral lines of 18 elements that can be detected with the present set-up in the spectral range 100–200 nm. Due to the reduced sensitivity, the shortest detected wavelength is, however, 117.6 nm for a Cl III emission line. The investigated elements were Al, C, Ca, Cl, Cu, Fe, H, K, Mg, Mn, Na, Ni, O, P, S, Si, Ti and Zn. While Ca, Mg and Na could hardly be detected in the VUV spectral range, as it is expected from wavelength tables, other rock forming elements such as Al, Fe, Si and Ti show strong emission lines and can likely be detected in many samples. The elements C, Cl and S, which are typically challenging to detect with LIBS in the conventional range above 200 nm, show the expected strong VUV emission lines and can likely be identified in various geological contexts. Emission lines of P have been identified as well but are likely too weak for a reliable detection of P in complex sample matrices. O shows a strong triplet at 130 nm, which often dominated the spectrum despite the low sensitivity of the set-up in this spectral range. The Lyman-α transition of H at 121.6 nm has been observed in some hydrated samples. Considering the strongly reduced sensitivity in this spectral range, this transition could be a reliable marker

for hydration with an improved set-up.

As the third and last part of the thesis, the quantification potential of VUV-LIBS for sulfur and chlorine in a lunar simulant matrix was investigated using the S I line at 180.7 nm and five Cl I lines around 135 nm, respectively. I observed considerable signal variations in these studies, which were attributed to a limited homogeneity of the samples. When using the mean intensity per concentration, however, a linear calibration can be retrieved for concentrations of up to 4 at% S and up to 10 at% Cl. Normalization with the total intensity of the spectrum was tested but did not yield a significant improvement of the signal scatter or the linearity of the calibration curves. Internal standard normalization with the O I triplet at 130 nm did not appear to be suitable for the S-bearing sample series but significantly improved the Cl-related data. The reason for this is an apparent decrease in sensitivity of up to a factor of eight in the spectral range below approximately 140 nm over the time of the measurement session. The most probable explanation for this decrease is the desorption of water from the walls of the vacuum chamber and the subsequent deposition on the cooled CCD chip. A calculation suggests that a layer of only 100–200 nm water or ice would be sufficient to explain this decrease in sensitivity.

Three major conclusions can be drawn from the results and observations of this thesis. Firstly, the results from the characterization of the VUV-LIBS system and from the experimental studies performed with it indicate that VUV-LIBS is promising for the application on celestial bodies without an atmosphere. The intense emission lines expected in the VUV spectral range have been observed for some of the elements that are challenging to detect with LIBS in the commonly investigated UV to NIR spectral range. Especially for S, a significantly improved detectability has been observed. Although the desired detection limit of 0.1 at% for lunar sulfur, as stated in chapter 6, is still not yet achieved, this approach should further be followed. The promising results presented in this thesis have been collected with the first iteration of a VUV-LIBS set-up, which is based on only commercial off-the-shelf components. If the set-up was further improved with customized components and optimized for the detection of S, a further increase of the detection capability can be expected and the desired detection limit would probably be achieved. Thus, detection in the VUV spectral range has the potential to improve the scientific return of LIBS measurements.

Secondly, while the VUV spectral range can greatly enhance the sensitivity for some elements, it poses its own experimental challenges. Some of those challenges, such as the evacuation of the spectrometer and the optical path, are only relevant in terrestrial laboratories and would not concern a space instrument, but the need for special VUV optics and VUV-sensitive detectors persists. Although it has been shown that such components can be produced, it needs to be investigated if they reliably work in the harsh space environment. Especially with respect to the lunar dust and the risk of contamination of the optical elements, an open front system as it has been used here should be avoided, but VUV-transparent windows are typically thin and made of fragile fluoride crystals. After going through all components and finding a space-compatible design, one will need to evaluate if the additional development and financial effort is reasonable for the added scientific return. The results of this thesis show that there are many interesting emission lines to detect in the VUV range and that analysing them would be especially beneficial for studies focusing on the non-metal elements. For future LIBS instruments, it should at least be considered if single VUV emission lines could be detected in addition to the UV-VIS-NIR spectra, which may offer the benefits of VUV-LIBS at a lower cost.

The third conclusion is that some aspects of the LIBS method need to be revised. Due to the various matrix effects, it is often emphasized that the samples used for the calibration should be similar to the samples analysed in the respective study, but the results of this thesis show that using lunar regolith simulant as the sample matrix causes strong signal fluctuations and hampers the calibration for a quantitative analysis. The reason for these fluctuations is found in properties inherent in the regolith simulant, such as the grain size and heterogeneity. Grinding the simulant to a fine powder would likely result in more stable signal levels but no longer resemble the lunar sampling conditions. In order to resolve this paradoxical situation,

more research on the fundamentals of LIBS is necessary that focuses especially on the matrix effects observed for geological samples with spatial variations in their chemical composition and physical structure. These effects are independent of the observed spectral range, but should be investigated in ambient conditions and with laser pulse energies that are equivalent to real mission scenarios. Nonetheless, one can say that LIBS is an important analytical method for space exploration. It has the unique capability of conducting remote chemical analyses over short distances of up to one metre in short times and without sample preparation. With an extended spectral range coverage including the VUV most of the chemical elements can be detected with reasonable LODs.

In the not too distant future, astronauts will return to the lunar surface from where they will proceed to Mars, and I am confident that at least some of them will carry a LIBS instrument to investigate the extraterrestrial surfaces, maybe even with detection in the VUV range.

Bibliography

[1] P. Janle: *Das Bild des Mondes*, in K. Urban, ed., *Der Mond: Von lunaren Dörfern, Schrammen und Lichtblitzen*, 3–14, Springer Berlin Heidelberg, Berlin, Heidelberg, ISBN 978-3-662-60282-9, doi: 10.1007/978-3-662-60282-9_1 (2020).

[2] J. Wörner, B. Foing and Moon Village International Support Group: *The "Moon Village" Concept and Initiative*, in *Annual Meeting of the Lunar Exploration Analysis Group*, Abstract #5084, URL `https://www.hou.usra.edu/meetings/leag2016/pdf/5084.pdf` (2016).

[3] I. A. Crawford: *Why we should build a Moon Village*, Astronomy and Geophysics, **58**, 6, 6.18, doi: 10.1093/astrogeo/atx220 (2017).

[4] International Space Exploration Coordination Group (ISECG): *The global exploration roadmap, 3rd edition*, [Online], URL `https://www.globalspaceexploration.org/wordpress/wp-content/isecg/GER_2018_small_mobile.pdf` (2018).

[5] D. A. Cremers: *Space applications of LIBS*, in S. Musazzi and U. Perini, eds., *Laser-Induced Breakdown Spectroscopy: Theory and Applications*, 257–291, Springer Berlin Heidelberg, Berlin, Heidelberg, ISBN 978-3-642-45085-3, doi: 10.1007/978-3-642-45085-3_10 (2014).

[6] J. Singh and S. Thakur, eds.: *Laser-Induced Breakdown Spectroscopy*, Elsevier Science, ISBN 978-0-444-51734-0, doi: 10.1016/B978-0-444-51734-0.X5001-7 (2007).

[7] D. A. Cremers and L. J. Radziemski, eds.: *Handbook of Laser-Induced Breakdown Spectroscopy*, John Wiley & Sons, Ltd, 2nd edition, ISBN 978-1-119-97112-2, doi: 10.1002/9781118567371 (2013).

[8] S. Maurice, S. M. Clegg, R. C. Wiens, O. Gasnault, W. Rapin, O. Forni, A. Cousin, V. Sautter, N. Mangold, L. Le Deit, M. Nachon, R. B. Anderson, N. L. Lanza, C. Fabre, V. Payré, J. Lasue, P.-Y. Meslin, R. J. Léveillé, B. L. Barraclough, P. Beck, S. C. Bender, G. Berger, J. C. Bridges, N. T. Bridges, G. Dromart, M. D. Dyar, R. Francis, J. Frydenvang, B. Gondet, B. L. Ehlmann, K. E. Herkenhoff, J. R. Johnson, Y. Langevin, M. B. Madsen, N. Melikechi, J.-L. Lacour, S. Le Mouélic, E. Lewin, H. E. Newsom, A. M. Ollila, P. Pinet, S. Schröder, J.-B. Sirven, R. L. Tokar, M. J. Toplis, C. d'Uston, D. T. Vaniman and A. R. Vasavada: *ChemCam activities and discoveries during the nominal mission of the Mars Science Laboratory in Gale crater, Mars*, Journal of Analytical Atomic Spectrometry, **31**, 4, 863, doi: 10.1039/C5JA00417A (2016).

[9] R. C. Wiens, S. Maurice, B. Barraclough, M. Saccoccio, W. C. Barkley, J. F. Bell, S. Bender, J. Bernardin, D. Blaney, J. Blank, M. Bouyé, N. Bridges, N. Bultman, P. Caïs, R. C. Clanton, B. Clark, S. Clegg, A. Cousin, D. Cremers, A. Cros, L. DeFlores, D. Delapp, R. Dingler, C. D'Uston, M. Darby Dyar, T. Elliott, D. Enemark, C. Fabre, M. Flores, O. Forni, O. Gasnault, T. Hale, C. Hays, K. Herkenhoff, E. Kan, L. Kirkland, D. Kouach, D. Landis, Y. Langevin, N. Lanza, F. LaRocca, J. Lasue, J. Latino, D. Limonadi, C. Lindensmith, C. Little, N. Mangold, G. Manhes, P. Mauchien, C. McKay, E. Miller, J. Mooney, R. V. Morris, L. Morrison, T. Nelson, H. Newsom, A. Ollila, M. Ott, L. Pares, R. Perez,

F. Poitrasson, C. Provost, J. W. Reiter, T. Roberts, F. Romero, V. Sautter, S. Salazar, J. J. Simmonds, R. Stiglich, S. Storms, N. Striebig, J.-J. Thocaven, T. Trujillo, M. Ulibarri, D. Vaniman, N. Warner, R. Waterbury, R. Whitaker, J. Witt and B. Wong-Swanson: *The ChemCam Instrument Suite on the Mars Science Laboratory (MSL) Rover: Body Unit and Combined System Tests*, Space Science Reviews, **170**, 1, 167, doi: 10.1007/s11214-012-9902-4 (2012).

[10] S. Maurice, R. C. Wiens, M. Saccoccio, B. Barraclough, O. Gasnault, O. Forni, N. Mangold, D. Baratoux, S. Bender, G. Berger, J. Bernardin, M. Berthé, N. Bridges, D. Blaney, M. Bouyé, P. Caïs, B. Clark, S. Clegg, A. Cousin, D. Cremers, A. Cros, L. DeFlores, C. Derycke, B. Dingler, G. Dromart, B. Dubois, M. Dupieux, E. Durand, L. d'Uston, C. Fabre, B. Faure, A. Gaboriaud, T. Gharsa, K. Herkenhoff, E. Kan, L. Kirkland, D. Kouach, J.-L. Lacour, Y. Langevin, J. Lasue, S. Le Mouélic, M. Lescure, E. Lewin, D. Limonadi, G. Manhès, P. Mauchien, C. McKay, P.-Y. Meslin, Y. Michel, E. Miller, H. E. Newsom, G. Orttner, A. Paillet, L. Parès, Y. Parot, R. Pérez, P. Pinet, F. Poitrasson, B. Quertier, B. Sallé, C. Sotin, V. Sautter, H. Séran, J. J. Simmonds, J.-B. Sirven, R. Stiglich, N. Striebig, J.-J. Thocaven, M. J. Toplis and D. Vaniman: *The ChemCam Instrument Suite on the Mars Science Laboratory (MSL) Rover: Science Objectives and Mast Unit Description*, Space Science Reviews, **170**, 1, 95, doi: 10.1007/s11214-012-9912-2 (2012).

[11] J. Lasue, R. C. Wiens, S. M. Clegg, D. T. Vaniman, K. H. Joy, S. Humphries, A. Mezzacappa, N. Melikechi, R. E. McInroy and S. Bender: *Remote laser-induced breakdown spectroscopy (LIBS) for lunar exploration*, Journal of Geophysical Research: Planets, **117**, E1, doi: 10.1029/2011JE003898 (2012).

[12] Z. A. Arp, D. A. Cremers, R. D. Harris, D. M. Oschwald, G. R. Parker and D. M. Wayne: *Feasibility of generating a useful laser-induced breakdown spectroscopy plasma on rocks at high pressure: preliminary study for a Venus mission*, Spectrochimica Acta Part B: Atomic Spectroscopy, **59**, 7, 987, doi: 10.1016/j.sab.2004.05.004 (2004).

[13] S. G. Pavlov, E. Jessberger, H.-W. Hübers, S. Schröder, I. Rauschenbach, S. Florek, J. Neumann, H. Henkel and S. Klinkner: *Miniaturized laser-induced plasma spectrometry for planetary in situ analysis - The case for Jupiter's moon Europa*, Advances in Space Research, **48**, 764 (2011).

[14] M. Horiuchi, K. Shibasaki, Y. Cho, S. Kameda, K. Ishibashi, K. Wada, T. Mikouchi, T. Nakamura and S. Sugita: *The discrimination experiment of meteorites using LIBS for the Martian Moons Explorer mission*, in *Japan Geoscience Union Meeting 2016*, PPS11–P16, Makuhari, Japan, URL `http://www2.jpgu.org/meeting/2016/PDF2016/P-PS11_all_e.pdf` (2016).

[15] A. Probst and R. Förstner: *Spacecraft design of a multiple asteroid orbiter with re-docking lander*, Past, Present and Future of Small Body Science and Exploration, **62**, 8, 2125, doi: 10.1016/j.asr.2017.07.041 (2018).

[16] X. Ren, T. Cai, J. Liu, H. Zhang, Q. Fu, Z. Zhang and W. Xu: *Preliminary Scientific Exploration Programs for Mars Surface Composition Detection Package of China's First Mars Exploration*, in *European Planetary Science Congress 2018*, volume 12, Abstract #759–2, URL `https://meetingorganizer.copernicus.org/EPSC2018/EPSC2018-759-2.pdf` (2018).

[17] R. C. Wiens, S. Maurice and F. Rull Perez: *The supercam remote sensing instrument suite for the mars 2020 rover mission: A preview*, Spectroscopy, **32**, 5 (2017).

[18] D. A. Cremers and L. J. Radziemski: *History and fundamentals of LIBS*, in A. W. Miziolek, V. Palleschi and I. Schechter, eds., *Laser Induced Breakdown Spectroscopy*, 1–39, Cambridge University Press, doi: 10.1017/CBO9780511541261.002 (2006).

[19] J. A. Effenberger and R. J. Scott: *Effect of Atmospheric Conditions on LIBS Spectra*, Sensors, **10**, 5, doi: 10.3390/s100504907 (2010).

[20] S. E. Wood and D. A. Paige: *Modeling the Martian seasonal CO_2 cycle*, Icarus, **99**, 1, 1, doi: 10.1016/0019-1035(92)90166-5 (1992).

[21] A. K. Knight, N. L. Scherbarth, D. A. Cremers and M. J. Ferris: *Characterization of Laser-Induced Breakdown Spectroscopy (LIBS) for Application to Space Exploration*, Applied Spectroscopy, **54**, 3, 331, doi: 10.1366/0003702001949591 (2000).

[22] G. Asimellis, A. Giannoudakos and M. Kompitsas: *New near-infrared LIBS detection technique for sulfur*, Analytical and Bioanalytical Chemistry, **385**, 2, 333, doi: 10.1007/s00216-006-0345-1 (2006).

[23] M. Hemmerlin, R. Meilland, H. Falk, P. Wintjens and L. Paulard: *Application of vacuum ultraviolet laser-induced breakdown spectrometry for steel analysis – comparison with spark-optical emission spectrometry figures of merit*, LIBS2000, 1st International Conference on Laser-Induced Plasma Spectroscopy and Applications, **56**, 6, 661, doi: 10.1016/S0584-8547(01)00217-8 (2001).

[24] M. A. Khater, J. T. Costello and E. T. Kennedy: *Optimization of the emission characteristics of laser-produced steel plasmas in the vacuum ultraviolet: Significant improvements in carbon detection limits*, Applied Spectroscopy, **56**, 8, 970, URL `http://as.osa.org/abstract.cfm?URI=as-56-8-970` (2002).

[25] C. D. Gehlen, E. Wiens, R. Noll, G. Wilsch and K. Reichling: *Chlorine detection in cement with laser-induced breakdown spectroscopy in the infrared and ultraviolet spectral range*, A Collection of Papers Presented at the Fifth International Conference on Laser Induced Breakdown Spectroscopy (LIBS 2008), **64**, 10, 1135, doi: 10.1016/j.sab.2009.07.021 (2009).

[26] M. Gaft, L. Nagli, I. Fasaki, M. Kompitsas and G. Wilsch: *Laser-induced breakdown spectroscopy for on-line sulfur analyses of minerals in ambient conditions*, A Collection of Papers Presented at the Fifth International Conference on Laser Induced Breakdown Spectroscopy (LIBS 2008), **64**, 10, 1098, doi: 10.1016/j.sab.2009.07.010 (2009).

[27] L. Radziemski, D. A. Cremers, K. Benelli, C. Khoo and R. D. Harris: *Use of the vacuum ultraviolet spectral region for laser-induced breakdown spectroscopy-based Martian geology and exploration*, Spectrochimica Acta Part B: Atomic Spectroscopy, **60**, 2, 237, doi: 10.1016/j.sab.2004.12.007 (2005).

[28] F. M. McCubbin, B. L. Jolliff, H. Nekvasil, P. K. Carpenter, R. A. Zeigler, A. Steele, S. M. Elardo and D. H. Lindsley: *Fluorine and chlorine abundances in lunar apatite: Implications for heterogeneous distributions of magmatic volatiles in the lunar interior*, Geochimica et Cosmochimica Acta, **75**, 17, 5073, doi: 10.1016/j.gca.2011.06.017 (2011).

[29] D. Vaniman, D. Pettit and G. Heiken: *Uses of Lunar sulfur*, in *The Second Conference on Lunar Bases and Space Activities of the 21st Century*, volume 2, 429–435, URL `https://ntrs.nasa.gov/search.jsp?R=19930004793` (1992).

[30] G. Kirchhoff and R. Bunsen: *Chemische Analyse durch Spectralbeobachtungen*, Justus Liebigs Annalen der Chemie, **118**, 3, 349, doi: 10.1002/jlac.18611180314 (1861).

[31] L. J. Radziemski: *From LASER to LIBS, the path of technology development*, Spectrochimica Acta Part B: Atomic Spectroscopy, **57**, 7, 1109, doi: 10.1016/S0584-8547(02)00052-6, 1st Euro-Mediterranean Symposium on Laser-Induced Breakdown Spectroscopy (2002).

[32] L. Radziemski and D. Cremers: *A brief history of laser-induced breakdown spectroscopy: From the concept of atoms to libs 2012*, Spectrochimica Acta Part B: Atomic Spectroscopy, **87**, 3, doi: 10.1016/j.sab.2013.05.013, thematic Issue: 7th International Conference on Laser Induced Breakdown Spectroscopy (LIBS 2012), Luxor, Egypt, 29 September-4 October 2012 (2013).

[33] B. Sallé, J.-L. Lacour, E. Vors, P. Fichet, S. Maurice, D. A. Cremers and R. C. Wiens: *Laser-Induced Breakdown Spectroscopy for Mars surface analysis: capabilities at stand-off distances and detection of chlorine and sulfur elements*, Spectrochimica Acta Part B: Atomic Spectroscopy, **59**, 9, 1413, doi: 10.1016/j.sab.2004.06.006 (2004).

[34] A. Botto, B. Campanella, S. Legnaioli, M. Lezzerini, G. Lorenzetti, S. Pagnotta, F. Poggialini and V. Palleschi: *Applications of laser-induced breakdown spectroscopy in cultural heritage and archaeology: a critical review*, J. Anal. At. Spectrom., **34**, 81, doi: 10.1039/C8JA00319J (2019).

[35] D. Girón, T. Delgado, J. Ruiz, L. Cabalín and J. Laserna: *In-situ monitoring and characterization of airborne solid particles in the hostile environment of a steel industry using stand-off LIBS*, Measurement, **115**, 1, doi: 10.1016/j.measurement.2017.09.046 (2018).

[36] G. S. Senesi: *Laser-induced breakdown spectroscopy (LIBS) applied to terrestrial and extraterrestrial analogue geomaterials with emphasis to minerals and rocks*, Earth-Science Reviews, **139**, 231, doi: 10.1016/j.earscirev.2014.09.008 (2014).

[37] R. E. Russo, X. Mao and S. S. Mao: *The Physics of Laser Ablation in Microchemical Analysis*, Analytical Chemistry, 70 A–77 A, doi: 10.1021/ac0219445 (2002).

[38] A. Miotello and R. Kelly: *Laser-induced phase explosion: new physical problems when a condensed phase approaches the thermodynamic critical temperature*, Applied Physics A, **69**, S67, doi: 10.1007/s003399900296 (1999).

[39] R. Russo, X. Mao, J. Yoo and J. Gonzalez: *Chapter 3 - laser ablation*, in J. P. Singh and S. N. Thakur, eds., *Laser-Induced Breakdown Spectroscopy*, 49–82, Elsevier, Amsterdam, ISBN 978-0-444-51734-0, doi: 10.1016/B978-044451734-0.50006-5 (2007).

[40] X. L. Mao, W. T. Chan, M. A. Shannon and R. E. Russo: *Plasma shielding during picosecond laser sampling of solid materials by ablation in He versus Ar atmosphere*, Journal of Applied Physics, **74**, 8, 4915, doi: 10.1063/1.354325 (1993).

[41] V. Rai and S. Thakur: *Chapter 4 - Physics of Plasma in Laser-Induced Breakdown Spectroscopy*, in J. P. Singh and S. N. Thakur, eds., *Laser-Induced Breakdown Spectroscopy*, 83–111, Elsevier, Amsterdam, ISBN 978-0-444-51734-0, doi: 10.1016/B978-044451734-0.50007-7 (2007).

[42] M. Capitelli, A. Casavola, G. Colonna and A. De Giacomo: *Laser-induced plasma expansion: theoretical and experimental aspects*, Spectrochimica Acta Part B: Atomic Spectroscopy, **59**, 3, 271, doi: 10.1016/j.sab.2003.12.017 (2004).

[43] D. Vogt, K. Rammelkamp, S. Schröder and H. Hübers: *Molecular emission in laser-induced breakdown spectroscopy: An investigation of its suitability for chlorine quantification on Mars*, Icarus, **302**, 470, doi: 10.1016/j.icarus.2017.12.006 (2018).

[44] A. Bogaerts, Z. Chen, R. Gijbels and A. Vertes: *Laser ablation for analytical sampling: what can we learn from modeling?*, Spectrochimica Acta Part B: Atomic Spectroscopy, **58**, 11, 1867, doi: 10.1016/j.sab.2003.08.004 (2003).

[45] S. Shabanov and I. Gornushkin: *Two-dimensional axisymmetric models of laser induced plasmas relevant to laser induced breakdown spectroscopy*, Spectrochimica Acta Part B: Atomic Spectroscopy, **100**, 147, doi: 10.1016/j.sab.2014.08.026 (2014).

[46] I. B. Gornushkin, S. V. Shabanov and U. Panne: *Abel inversion applied to a transient laser induced plasma: implications from plasma modeling*, J. Anal. At. Spectrom., **26**, 1457, doi: 10.1039/C1JA10044K (2011).

[47] W. T. Chan and R. E. Russo: *Study of laser-material interactions using inductively coupled plasma-atomic emission spectrometry*, Spectrochimica Acta Part B: Atomic Spectroscopy, **46**, 11, 1471, doi: 10.1016/0584-8547(91)80199-D (1991).

[48] R. W. P. McWhirter: *Spectral Intensities*, in R. H. Huddlestone and S. L. Leonard, eds., *Plasma Diagnostic Techniques*, 201–264 (1965).

[49] G. Cristoforetti, A. De Giacomo, M. Dell'Aglio, S. Legnaioli, E. Tognoni, V. Palleschi and N. Omenetto: *Local Thermodynamic Equilibrium in Laser-Induced Breakdown Spectroscopy: Beyond the McWhirter criterion*, Spectrochimica Acta Part B: Atomic Spectroscopy, **65**, 1, 86, doi: 10.1016/j.sab.2009.11.005 (2010).

[50] P. Hansen, S. Schröder, S. Kubitza, K. Rammelkamp, D. Vogt and H.-W. Hübers: *Modeling of time-resolved LIBS spectra with a stationary plasma model for the application to Martian LIBS spectra*, in preparation (2020).

[51] H. R. Griem: *High-density corrections in plasma spectroscopy*, Phys. Rev., **128**, 997, doi: 10.1103/PhysRev.128.997 (1962).

[52] A. Kramida, Yu. Ralchenko, J. Reader and NIST ASD Team: *NIST Atomic Spectra Database (ver. 5.7.1)*, [Online], URL `https://physics.nist.gov/asd` (2019).

[53] R. Kurucz and B. Bell: *Atomic Line Data, Kurucz CD-ROM No. 23*, Cambridge, Mass.: Smithsonian Astrophysical Observatory, URL `https://www.cfa.harvard.edu/amp/ampdata/kurucz23/sekur.html` (1995).

[54] T. Takahashi and B. Thornton: *Quantitative methods for compensation of matrix effects and self-absorption in Laser Induced Breakdown Spectroscopy signals of solids*, Spectrochimica Acta Part B: Atomic Spectroscopy, **138**, 31, doi: 10.1016/j.sab.2017.09.010 (2017).

[55] F. Anabitarte García, L. Rodríguez Cobo, J. M. López Higuera and A. Cobo García: *Normalization of laser-induced breakdown spectroscopy spectra using a plastic optical fiber light collector and acoustic sensor device*, Applied Optics, **51**, 8306, URL `http://hdl.handle.net/10902/2172` (2012).

[56] S. I. Gornushkin, I. B. Gornushkin, J. M. Anzano, B. W. Smith and J. D. Winefordner: *Effective normalization technique for correction of matrix effects in laser-induced breakdown spectroscopy detection of magnesium in powdered samples*, Applied Spectroscopy, **56**, 4, 433, doi: 10.1366/0003702021955088 (2002).

[57] J. Guezenoc, A. Gallet-Budynek and B. Bousquet: *Critical review and advices on spectral-based normalization methods for LIBS quantitative analysis*, Spectrochimica Acta Part B: Atomic Spectroscopy, **160**, 105688, doi: 10.1016/j.sab.2019.105688 (2019).

[58] J. P. Castro and E. R. Pereira-Filho: *Twelve different types of data normalization for the proposition of classification, univariate and multivariate regression models for the direct analyses of alloys by laser-induced breakdown spectroscopy (libs)*, J. Anal. At. Spectrom., **31**, 2005, doi: 10.1039/C6JA00224B (2016).

[59] A. dos Santos Augusto, P. L. Barsanelli, F. M. V. Pereira and E. R. Pereira-Filho: *Calibration strategies for the direct determination of Ca, K, and Mg in commercial samples of powdered milk and solid dietary supplements using laser-induced breakdown spectroscopy (LIBS)*, Food Research International, **94**, 72, doi: 10.1016/j.foodres.2017.01.027 (2017).

[60] A. Kuwako, Y. Uchida and K. Maeda: *Supersensitive detection of sodium in water with use of dual-pulse laser-induced breakdown spectroscopy*, Appl. Opt., **42**, 30, 6052, doi: 10.1364/AO.42.006052 (2003).

[61] W. Rapin, P.-Y. Meslin, S. Maurice, R. Wiens, D. Laporte, B. Chauviré, O. Gasnault, S. Schröder, P. Beck, S. Bender, O. Beyssac, A. Cousin, E. Dehouck, C. Drouet, O. Forni, M. Nachon, N. Melikechi, B. Rondeau, N. Mangold and N. Thomas: *Quantification of water content by laser induced breakdown spectroscopy on Mars*, Spectrochimica Acta Part B: Atomic Spectroscopy, **130**, 82, doi: 10.1016/j.sab.2017.02.007 (2017).

[62] S. Schröder, K. Rammelkamp, D. Vogt, O. Gasnault and H.-W. Hübers: *Contribution of a martian atmosphere to laser-induced breakdown spectroscopy (LIBS) data and testing its emission characteristics for normalization applications*, Icarus, **325**, 1, doi: 10.1016/j.icarus.2019.02.017 (2019).

[63] W. Barnett, V. Fassel and R. Kniseley: *Theoretical principles of internal standardization in analytical emission spectroscopy*, Spectrochimica Acta Part B: Atomic Spectroscopy, **23**, 10, 643, doi: 10.1016/0584-8547(68)80045-X (1968).

[64] S. A. Myers and D. H. Tracy: *Improved performance using internal standardization in inductively-coupled plasma emission spectroscopy*, Spectrochimica Acta Part B: Atomic Spectroscopy, **38**, 9, 1227, doi: 10.1016/0584-8547(83)80066-4 (1983).

[65] IUPAC, ed.: *Compendium of Chemical Terminology, 2nd ed. (the "Gold Book")*, Blackwell Scientific Publications, Oxford, 2 edition, ISBN 0-9678550-9-8, URL `https://goldbook.iupac.org/`, compiled by A. D. McNaught and A. Wilkinson (1997).

[66] D. A. Cremers and L. J. Radziemski: *LIBS Analytical Figures of Merit and Calibration*, in *Handbook of Laser-Induced Breakdown Spectroscopy*, 123–150, John Wiley & Sons, Ltd, ISBN 978-1-118-56737-1, doi: 10.1002/9781118567371.ch4 (2013).

[67] L. A. Currie: *Limits for qualitative detection and quantitative determination. Application to radiochemistry*, Analytical Chemistry, **40**, 3, 586, doi: 10.1021/ac60259a007 (1968).

[68] D. L. Massart, B. G. M. Vandeginste, L. M. C. Buydens, S. D. Jong, P. J. Lewi and J. Smeyers-Verbeke: *Chapter 13 Internal method validation*, in *Handbook of Chemometrics and Qualimetrics: Part A*, volume 20 of *Data Handling in Science and Technology*, 379–440, Elsevier, doi: 10.1016/S0922-3487(97)80043-3 (1998).

[69] W. Englisch: *Quartzglass For Space Optical Applications*, in R. R. Hale, ed., *Space Optical Materials and Space Qualification of Optics*, volume 1118, 42–49, International Society for Optics and Photonics, SPIE, doi: 10.1117/12.960946 (1989).

[70] T. Feigl, J. Heber, A. Gatto and N. Kaiser: *Optics developments in the VUV-soft X-ray spectral region*, Nuclear Instruments and Methods in Physics Research Section A: Accelerators, Spectrometers, Detectors and Associated Equipment, **483**, 1, 351, doi: 10.1016/S0168-9002(02)00342-X (2002).

[71] E. G. Loewen and M. Neviere: *Simple selection rules for VUV and XUV diffraction gratings*, Applied Optics, **17**, 7, 1087, doi: 10.1364/AO.17.001087 (1978).

[72] G. Hass: *Filmed surfaces for reflecting optics*, Journal of the Optical Society of America, **45**, 11, 945, doi: 10.1364/JOSA.45.000945 (1955).

[73] S. Wilbrandt, O. Stenzel, H. Nakamura, D. Wulff-Molder, A. Duparré and N. Kaiser: *Protected and enhanced aluminum mirrors for the VUV*, Appl. Opt., **53**, 4, A125, doi: 10.1364/AO.53.00A125 (2014).

[74] J. Hollandt, M. C. E. Huber and M. Kühne: *Hollow cathode transfer standards for the radiometric calibration of VUV telescopes of the Solar and Heliospheric Observatory (SOHO)*, Metrologia, **30**, 4, 381, doi: 10.1088/0026-1394/30/4/033 (1993).

[75] S. Sharma, A. Misra, P. Lucey, R. Wiens and S. Clegg: *Combined remote LIBS and Raman spectroscopy at* 8.6 m *of sulfur-containing minerals, and minerals coated with hematite or covered with basaltic dust*, Seventh International Conference on Raman Spectroscopy Applied to the Earth and Planetary Sciences, **68**, 4, 1036, doi: 10.1016/j.saa.2007.06.046 (2007).

[76] K. Rammelkamp, S. Schröder, S. Kubitza, D. S. Vogt, S. Frohmann, P. B. Hansen, U. Böttger, F. Hanke and H.-W. Hübers: *Low-level LIBS and Raman data fusion in the context of in situ Mars exploration*, Journal of Raman Spectroscopy, 1–20, doi: 10.1002/jrs.5615 (2019).

[77] G. Bazalgette Courrèges-Lacoste, B. Ahlers and F. R. Pérez: *Combined Raman spectrometer/laser-induced breakdown spectrometer for the next ESA mission to Mars*, Spectrochimica Acta Part A: Molecular and Biomolecular Spectroscopy, **68**, 4, 1023, doi: 10.1016/j.saa.2007.03.026, seventh International Conference on Raman Spectroscopy Applied to the Earth and Planetary Sciences (2007).

[78] M. Hoehse, D. Mory, S. Florek, F. Weritz, I. Gornushkin and U. Panne: *A combined laser-induced breakdown and Raman spectroscopy echelle system for elemental and molecular microanalysis*, Spectrochimica Acta Part B: Atomic Spectroscopy, **64**, 11, 1219, doi: 10.1016/j.sab.2009.09.004 (2009).

[79] V. N. Lednev, S. M. Pershin, P. A. Sdvizhenskii, M. Y. Grishin, A. N. Fedorov, V. V. Bukin, V. B. Oshurko and A. N. Shchegolikhin: *Combining Raman and laser induced breakdown spectroscopy by double pulse lasing*, Analytical and Bioanalytical Chemistry, **410**, 1, 277, doi: 10.1007/s00216-017-0719-6 (2018).

[80] A. Smekal: *Zur Quantentheorie der Dispersion*, Naturwissenschaften, **11**, 43, 873, doi: 10.1007/BF01576902 (1923).

[81] C. Raman: *A new radiation*, Indian Journal of Physics, **2**, 387 (1928).

[82] G. Landsberg: *Eine neue Erscheinung bei der Lichtzerstreuung in Krystallen*, Naturwissenschaften, **16**, 558 (1928).

[83] S. Kubitza: *Optical Investigation Into Individual Nanowires Using a Tunable Laser*, Master's thesis, Technische Universität Berlin/Lunds Universitet, Berlin, Germany/Lund, Sweden (2016).

[84] S. Kubitza, D. Vogt, K. Rammelkamp, U. Böttger, S. Frohmann, P. Hansen, S. Schröder and H.-W. Hübers: *A miniaturized Raman/LIBS instrument for in-situ investigation of celestial bodies in pioneering missions*, in *European Planetary Science Congress 2018*, Abstract #789, Europlanet Society, Berlin, Germany, URL `https://meetingorganizer.copernicus.org/EPSC2018/EPSC2018-789.pdf` (2018).

[85] S. Kubitza, S. Schröder, K. Rammelkamp, T. Hagelschuer, U. Böttger, P. Hansen, D. Vogt and H.-W. Hübers: *Evaluation of close-up remote cw-Raman spectroscopy for in-situ planetary exploration*, in *50th Lunar and Planetary Science Conference*, Abstract #2421, Lunar and Planetary Institute, Houston, USA, URL `https://www.hou.usra.edu/meetings/lpsc2019/pdf/2421.pdf` (2019).

[86] S. R. Taylor: *Chapter 12 - The Moon*, in L.-A. McFadden, P. R. Weissman and T. V. Johnson, eds., *Encyclopedia of the Solar System (Second Edition)*, 227–250, Academic Press, San Diego, ISBN 978-0-12-088589-3, doi: 10.1016/B978-012088589-3/50016-5 (2007).

[87] D. Britt and K. M. Cannon: *The CLASS Exolith Lab*, in *NASA Exploration Science Forum 2019*, volume NESF2019, 082, URL `https://nesf2019.arc.nasa.gov/abstract/nesf2019-082` (2019).

[88] K. Ben Mabrouk, T. H. Kauffmann, H. Aroui and M. D. Fontana: *Raman study of cation effect on sulfate vibration modes in solid state and in aqueous solutions*, Journal of Raman Spectroscopy, **44**, 11, 1603, doi: 10.1002/jrs.4374 (2013).

[89] A. T. Ward: *Raman spectroscopy of sulfur, sulfur-selenium, and sulfur-arsenic mixtures*, The Journal of Physical Chemistry, **72**, 12, 4133, doi: 10.1021/j100858a031 (1968).

[90] J. Alsemgeest, S. Schröder, U. Böttger, S. G. Pavlov, I. Weber, A. Greshake, H.-R. Knöfler, U. Altenberger and H.-W. Hübers: *Combined Raman-LIBS studies on iron sulfides to investigate the effect of the LIBS plasma on the mineral composition*, in *79th Annual Meeting of the Meteoritical Society*, volume 79, 6353 (2016).

[91] S. Schröder, K. Rammelkamp, F. Hanke, I. Weber, D. S. Vogt, S. Frohmann, S. Kubitza, U. Böttger and H.-W. Hübers: *Effects of pulsed laser and plasma interaction on Fe, Ni, Ti, and their oxides for LIBS Raman analysis in extraterrestrial environments*, Journal of Raman Spectroscopy, 1–15, doi: 10.1002/jrs.5650 (2019).

[92] T. Namioka: *Theory of the concave grating. I*, Journal of the Optical Society of America, **49**, 5, 446, doi: 10.1364/JOSA.49.000446 (1959).

[93] K. Watanabe, E. C. Y. Inn and M. Zelikoff: *Absorption coefficients of gases in the vacuum ultraviolet*, The Journal of Chemical Physics, **20**, 12, 1969, doi: 10.1063/1.1700353 (1952).

[94] S. S. Mao, X. Zeng, X. Mao and R. E. Russo: *Laser-induced breakdown spectroscopy: flat surface vs. cavity structures*, J. Anal. At. Spectrom., **19**, 495, doi: 10.1039/B315725C (2004).

[95] R. Radhakrishnan, J. Xu, S. Lucatero, S. Snyder, T. D. Hall, B. Skinn, M. Inman and E. J. Taylor: *Atmospheric, non-contact and high speed electro chemical machining processes for x-ray optics*, ECS Transactions, **77**, 11, 1255, doi: 10.1149/07711.1255ecst (2017).

[96] C. B. Dreyer, G. S. Mungas, P. Thanh and J. G. Radziszewski: *Study of sub-mJ-excited laser-induced plasma combined with Raman spectroscopy under Mars atmosphere-simulated conditions*, Spectrochimica Acta Part B: Atomic Spectroscopy, **62**, 12, 1448, doi: 10.1016/j.sab.2007.10.016 (2007).

[97] Ş. Yalçin, Y. Y. Tsui and R. Fedosejevs: *Pressure dependence of emission intensity in femtosecond laser-induced breakdown spectroscopy*, J. Anal. At. Spectrom., **19**, 1295, doi: 10.1039/B404132A (2004).

[98] W. Rapin, B. Bousquet, J. Lasue, P.-Y. Meslin, J.-L. Lacour, C. Fabre, R. Wiens, J. Frydenvang, E. Dehouck, S. Maurice, O. Gasnault, O. Forni and A. Cousin: *Roughness effects on the hydrogen signal in laser-induced breakdown spectroscopy*, Spectrochimica Acta Part B: Atomic Spectroscopy, **137**, 13, doi: 10.1016/j.sab.2017.09.003 (2017).

[99] M. Tani, H. Kurniawan, H. Ueda, K. Mizukami, K. Kawai and K. Kagawa: *Reflection and diffraction of laser plasma induced by bombardment of TEA CO_2 laser at low pressures*, Japanese Journal of Applied Physics, **32**, Part 1, No. 9A, 3838, doi: 10.1143/jjap.32.3838 (1993).

[100] Z. Q. Hao, L. Liu, M. Shen, X. Y. Yang, K. Li, L. B. Guo, X. Y. Li, Y. F. Lu and X. Y. Zeng: *Investigation on self-absorption at reduced air pressure in quantitative analysis using laser-induced breakdown spectroscopy*, Opt. Express, **24**, 23, 26521, doi: 10.1364/OE.24.026521 (2016).

[101] P. Loiseleur, T. N. Hansen, J. Larour and J. G. Lunney: *Time-resolved EUV spectroscopy in the early stage of laser ablation of carbon*, Applied Surface Science, **197-198**, 164, doi: 10.1016/S0169-4332(02)00319-7 (2002).

[102] C. Aragón and J. Aguilera: *Characterization of laser induced plasmas by optical emission spectroscopy: A review of experiments and methods*, Spectrochimica Acta Part B: Atomic Spectroscopy, **63**, 9, 893, doi: 10.1016/j.sab.2008.05.010 (2008).

[103] J. D. Hunter: *Matplotlib: A 2D graphics environment*, Computing in Science & Engineering, **9**, 3, 90, doi: 10.1109/MCSE.2007.55 (2007).

[104] P. Virtanen, R. Gommers, T. E. Oliphant, M. Haberland, T. Reddy, D. Cournapeau, E. Burovski, P. Peterson, W. Weckesser, J. Bright, S. J. van der Walt, M. Brett, J. Wilson, K. Jarrod Millman, N. Mayorov, A. R. J. Nelson, E. Jones, R. Kern, E. Larson, C. Carey, İ. Polat, Y. Feng, E. W. Moore, J. Vand erPlas, D. Laxalde, J. Perktold, R. Cimrman, I. Henriksen, E. A. Quintero, C. R. Harris, A. M. Archibald, A. H. Ribeiro, F. Pedregosa, P. van Mulbregt and SciPy 1. 0 Contributors: *SciPy 1.0: Fundamental algorithms for scientific computing in Python*, Nature Methods, **17**, 261, doi: 10.1038/s41592-019-0686-2 (2020).

[105] J. Jasik, J. Heitz, J. D. Pedarnig and P. Veis: *Vacuum ultraviolet laser-induced breakdown spectroscopy analysis of polymers*, A Collection of Papers Presented at the Fifth International Conference on Laser Induced Breakdown Spectroscopy (LIBS 2008), **64**, 10, 1128, doi: 10.1016/j.sab.2009.07.013 (2009).

[106] J. Bengoechea and E. T. Kennedy: *Time-integrated, spatially resolved plasma characterization of steel samples in the VUV*, Journal of Analytical Atomic Spectrometry, **19**, 4, 468, doi: 10.1039/B315653B (2004).

[107] V. Sturm, L. Peter and R. Noll: *Steel analysis with laser-induced breakdown spectrometry in the vacuum ultraviolet*, Applied Spectroscopy, **54**, 9, 1275, doi: 10.1366/0003702001951183 (2000).

[108] A. Segnini, A. Xavier, O. Junior, E. Ferreira, A. Watanabe, M. A. Sperança, G. Nicolodelli, P. Villas Boas, A. Oliveira, P. Villas-Boas, P. Oliveira and D. Milori: *Physical and chemical matrix effects in soil carbon quantification using laser-induced breakdown spectroscopy*, American Journal of Analytical Chemistry, **5**, 722, doi: 10.4236/ajac.2014.511080 (2014).

[109] J. Grotzinger and T. Jordan: *System Erde*, 3–22, Springer Berlin Heidelberg, Berlin, Heidelberg, ISBN 978-3-662-48342-8, doi: 10.1007/978-3-662-48342-8_1 (2017).

[110] J. Papike, L. Taylor and S. Simon: *Lunar minerals*, in G. H. Heiken, D. T. Vaniman and B. M. French, eds., *Lunar Sourcebook: A User's Guide to the Moon*, Cambridge University Press, URL `https://www.lpi.usra.edu/lunar_sourcebook/` (1991).

[111] H. Y. McSween, G. J. Taylor and M. B. Wyatt: *Elemental composition of the Martian crust*, Science, **324**, 5928, 736, doi: 10.1126/science.1165871 (2009).

[112] S. Y. Chan and N. H. Cheung: *Analysis of solids by laser ablation and resonance-enhanced laser-induced plasma spectroscopy*, Analytical Chemistry, **72**, 9, 2087, doi: 10.1021/ac991242o (2000).

[113] R. Knopp, F. J. Scherbaum and J. I. Kim: *Laser induced breakdown spectroscopy (LIBS) as an analytical tool for the detection of metal ions in aqueous solutions*, Fresenius' Journal of Analytical Chemistry, **355**, 1, 16, doi: 10.1007/s0021663550016 (1996).

[114] Ş. Yalçin, D. Crosley, G. Smith and G. Faris: *Influence of ambient conditions on the laser air spark*, Applied Physics B: Lasers and Optics, **68**, 1, 121, doi: 10.1007/s003400050596 (1999).

[115] D. Vogt, S. Schröder, K. Rammelkamp, P. Hansen, S. Kubitza and H.-W. Hübers: *CaCl and CaF emission in LIBS under simulated Martian conditions*, Icarus, **335**, 113393, doi: 10.1016/j.icarus.2019.113393 (2020).

[116] S. S. Harilal, B. E. Brumfield and M. C. Phillips: *Lifecycle of laser-produced air sparks*, Physics of Plasmas, **22**, 6, 063301, doi: 10.1063/1.4922076 (2015).

[117] K. Rammelkamp: *Investigation of LIBS and Raman data analysis methods in the context of in-situ planetary exploration*, Ph.D. thesis, Humboldt-Universität zu Berlin, Mathematisch-Naturwissenschaftliche Fakultät, doi: 10.18452/20703 (2019).

[118] K. Niemax: *Laser ablation - reflections on a very complex technique for solid sampling*, Fresenius' Journal of Analytical Chemistry, **370**, 4, 332, doi: 10.1007/s002160100796 (2001).

[119] K. Righter, K. Pando and L. R. Danielson: *Experimental evidence for sulfur-rich Martian magmas: Implications for volcanism and surficial sulfur sources*, Earth and Planetary Science Letters, **288**, 1, 235, doi: 10.1016/j.epsl.2009.09.027 (2009).

[120] P. J. Wallace: *Volcanic SO_2 emissions and the abundance and distribution of exsolved gas in magma bodies*, Journal of Volcanology and Geothermal Research, **108**, 1, 85, doi: 10.1016/S0377-0273(00)00279-1 (2001).

[121] J. Carpenter, R. Fisackerly and B. Houdou: *Establishing lunar resource viability*, Space Policy, **37**, 52, doi: 10.1016/j.spacepol.2016.07.002 (2016).

[122] M. Anand, I. Crawford, M. Balat-Pichelin, S. Abanades, W. van Westrenen, G. Péraudeau, R. Jaumann and W. Seboldt: *A brief review of chemical and mineralogical resources on the Moon and likely initial in situ resource utilization (ISRU) applications*, Planetary and Space Science, **74**, 1, 42, doi: 10.1016/j.pss.2012.08.012 (2012).

[123] J. E. Kleinhenz and A. Paz: *An ISRU propellant production system for a fully fueled Mars Ascent Vehicle*, in *10th Symposium on Space Resource Utilization*, AIAA SciTech Forum, American Institute of Aeronautics and Astronautics, doi: 10.2514/6.2017-0423 (2017).

[124] D. Kornuta, A. Abbud-Madrid, J. Atkinson, J. Barr, G. Barnhard, D. Bienhoff, B. Blair, V. Clark, J. Cyrus, B. DeWitt, C. Dreyer, B. Finger, J. Goff, K. Ho, L. Kelsey, J. Keravala, B. Kutter, P. Metzger, L. Montgomery, P. Morrison, C. Neal, E. Otto, G. Roesler, J. Schier, B. Seifert, G. Sowers, P. Spudis, M. Sundahl, K. Zacny and G. Zhu: *Commercial lunar propellant architecture: A collaborative study of lunar propellant production*, REACH, **13**, 100026, doi: 10.1016/j.reach.2019.100026 (2019).

[125] B. Kading and J. Straub: *Utilizing in-situ resources and 3D printing structures for a manned Mars mission*, Acta Astronautica, **107**, 317, doi: 10.1016/j.actaastro.2014.11.036 (2015).

[126] B. Khoshnevis, M. Bodiford, K. Burks, E. Ethridge, D. Tucker, W. Kim, H. Toutanji and M. Fiske: *Lunar contour crafting - a novel technique for ISRU-based habitat development*, in *43rd AIAA Aerospace Sciences Meeting and Exhibit*, Aerospace Sciences Meetings, American Institute of Aeronautics and Astronautics, doi: 10.2514/6.2005-538 (2005).

[127] L. Haskin and P. Warren: *Lunar chemistry*, in G. H. Heiken, D. T. Vaniman and B. M. French, eds., *Lunar Sourcebook: A User's Guide to the Moon*, Cambridge University Press, URL `https://www.lpi.usra.edu/lunar_sourcebook/` (1991).

[128] I. Radivojevic, C. Haisch, R. Niessner, S. Florek, H. Becker-Ross and U. Panne: *Microanalysis by laser-induced plasma spectroscopy in the vacuum ultraviolet*, Analytical Chemistry, **76**, 6, 1648, doi: 10.1021/ac0351365 (2004).

[129] F. Trichard, S. Moncayo, D. Devismes, F. Pelascini, J. Maurelli, A. Feugier, C. Sasseville, F. Surma and V. Motto-Ros: *Evaluation of a compact VUV spectrometer for elemental imaging by laser-induced breakdown spectroscopy: application to mine core characterization*, Journal of Analytical Atomic Spectrometry, **32**, 8, 1527, doi: 10.1039/C7JA00185A (2017).

[130] S. Kubitza, S. Schröder, E. Dietz, S. Frohmann, P. B. Hansen, K. Rammelkamp, D. S. Vogt, M. Gensch and H.-W. Hübers: *Detecting sulfur on the Moon: The potential of vacuum ultraviolet laser-induced breakdown spectroscopy*, Spectrochimica Acta B, **174**, 105990 (2020).

[131] J. Hermann, C. Boulmer-Leborgne and D. Hong: *Diagnostics of the early phase of an ultraviolet laser induced plasma by spectral line analysis considering self-absorption*, Journal of Applied Physics, **83**, 2, 691, doi: 10.1063/1.366639 (1998).

[132] Y. Zhang, J. R. G. Evans and S. Yang: *Corrected values for boiling points and enthalpies of vaporization of elements in handbooks*, Journal of Chemical & Engineering Data, **56**, 2, 328, doi: 10.1021/je1011086 (2011).

[133] R. Green, R. Perry, D. Green and Knovel (Firm): *Perry's Chemical Engineers' Handbook, Eighth Edition*, number Bd. 8 in Chemical Engineers Handbook, McGraw-Hill Education, ISBN 9780071422949 (2008).

[134] X. Mao, W.-T. Chan, M. Caetano, M. A. Shannon and R. E. Russo: *Preferential vaporization and plasma shielding during nano-second laser ablation*, Applied Surface Science, **96-98**, 126, doi: 10.1016/0169-4332(95)00420-3 (1996).

[135] D. A. Cremers and L. J. Radziemski: *Basics of the LIBS plasma*, in *Handbook of Laser-Induced Breakdown Spectroscopy*, 29–68, John Wiley & Sons, Ltd, ISBN 978-1-118-56737-1, doi: 10.1002/9781118567371.ch2 (2013).

[136] I. A. Crawford: *Lunar resources: A review*, Progress in Physical Geography: Earth and Environment, **39**, 2, 137, doi: 10.1177/0309133314567585 (2015).

[137] D. Vogt, S. Schröder, H.-W. Hübers, L. Richter, M. Glier, G. Artan, P. Wessels and J. Neumann: *LIBS for volatile detection in the lunar polar region*, in *51st Lunar and Planetary Science Conference (2020)*, Abstract #1385, Lunar and Planetary Institute, URL `https://www.hou.usra.edu/meetings/lpsc2020/pdf/1385.pdf` (2020).

[138] A. Cousin, P. Meslin, R. Wiens, W. Rapin, N. Mangold, C. Fabre, O. Gasnault, O. Forni, R. Tokar, A. Ollila, S. Schröder, J. Lasue, S. Maurice, V. Sautter, H. Newsom, D. Vaniman, S. Le Mouélic, D. Dyar, G. Berger, D. Blaney, M. Nachon, G. Dromart, N. Lanza, B. Clark, S. Clegg, W. Goetz, J. Berger, B. Barraclough and D. Delapp: *Compositions of coarse and fine particles in Martian soils at gale: A window into the production of soils*, Icarus, **249**, 22, doi: 10.1016/j.icarus.2014.04.052, special Issue: First Year of MSL (2015).

[139] P. Kadkhoda, A. Müller and D. Ristau: *Total scatter losses of optical components in the DUV/VUV spectral range*, in G. J. Exarhos, A. H. Guenther, M. R. Kozlowski, K. L. Lewis and M. J. Soileau, eds., *Laser-Induced Damage in Optical Materials: 1999*, volume 3902, 118–127, International Society for Optics and Photonics, SPIE, doi: 10.1117/12.379308 (2000).

[140] K. Watanabe and M. Zelikoff: *Absorption coefficients of water vapor in the vacuum ultraviolet*, Journal of the Optical Society of America, **43**, 9, 753, doi: 10.1364/JOSA.43.000753 (1953).

[141] S. G. Warren: *Optical constants of ice from the ultraviolet to the microwave*, Applied Optics, **23**, 8, 1206, doi: 10.1364/AO.23.001206 (1984).

List of Figures

List of Tables

List of Publications

Peer-reviewed publications (first author)

- S. Kubitza, S. Schröder, E. Dietz, S. Frohmann, P. B. Hansen, K. Rammelkamp, D. S. Vogt, M. Gensch and H.-W. Hübers: *Detecting sulfur on the Moon: The potential of vacuum ultraviolet laser-induced breakdown spectroscopy*, Spectrochimica Acta B, **174**, 105990, doi: 10.1016/j.sab.2020.105990 (2020)

Peer-reviewed publications (co-author)

- K. Rammelkamp, S. Schröder, S. Kubitza, D. S. Vogt, S. Frohmann, P. B. Hansen, U. Böttger, F. Hanke and H.-W. Hübers: *Low-level LIBS and Raman data fusion in the context of in-situ Mars exploration*, Journal of Raman Spectroscopy, 1–20, doi: 10.1002/jrs.5615 (2019)
- S. Schröder, K. Rammelkamp, F. Hanke, I. Weber, D. S. Vogt, S. Frohmann, S. Kubitza, U. Böttger and H.-W. Hübers: *Effects of pulsed laser and plasma interaction on Fe, Ni, Ti, and their oxides for LIBS Raman analysis in extraterrestrial environments*, Journal of Raman Spectroscopy, 1–15, doi: 10.1002/jrs.5650 (2019)
- D. Vogt, S. Schröder, K. Rammelkamp, P. Hansen, S. Kubitza and H.-W. Hübers: *CaCl and CaF emission in LIBS under simulated Martian conditions*, Icarus, **335**, 113393, doi: 10.1016/j.icarus.2019.113393 (2020)

Oral presentations at conferences

- S. Kubitza, D. Vogt, K. Rammelkamp, U. Böttger, S. Frohmann, P. Hansen, S. Schröder and H.-W. Hübers: *A miniaturized Raman/LIBS instrument for in-situ investigation of celestial bodies in pioneering missions*, in *European Planetary Science Congress 2018*, Abstract #789, Europlanet Society, Berlin, Germany (2018)
- S. Kubitza, S. Schröder, S. Frohmann, E. Dietz, P. B. Hansen, K. Rammelkamp, D. Vogt and H.-W. Hübers: *VUV-LIBS for volatile detection in space exploration*, in *EPSC-DPS Joint Meeting 2019*, Abstract #586–1, Europlanet Society, Genève, Switzerland (2019)

Poster presentations at conferences

- S. Kubitza, K. Rammelkamp, D. Vogt, S. Frohmann, P. B. Hansen, S. Schröder, H.-W. Hübers: *Miniaturized low power LIBS system for in-situ exploration of Solar System bodies without atmosphere*, in *SciX 2018*, Federation of Analytical Chemistry and Spectroscopy Societies, Atlanta, USA (2018)
- S. Kubitza, S. Schröder, K. Rammelkamp, T. Hagelschuer, U. Böttger, P. Hansen, D. Vogt and H.-W. Hübers: *Evaluation of close-up remote cw-Raman spectroscopy for in-situ planetary exploration*, in *50th Lunar and Planetary Science Conference*, Abstract #2421, Lunar and Planetary Institute, Houston, USA (2019)
- S. Kubitza, S. Schröder, E. Dietz, S. Frohmann, P. B. Hansen, K. Rammelkamp, D. Vogt, M. Gensch and H.-W. Hübers: *Sulfur and chlorine detection in a lunar context using VUV-LIBS*, in *European Planetary Science Congress 2020*, Abstract #806, Europlanet Society, Online (2020)

Danksagung

Die vergangenen drei Jahre waren eine spannende Zeit in einer tollen Forschungsgruppe und haben mir neue Erkenntnisse in vielerlei Hinsicht geliefert, wissenschaftlich und persönlich. Es war aber auch eine herausfordernde Zeit, in der ich von vielen Menschen in meinem Umfeld unterstützt wurde, wofür ich mich hier bedanken möchte.

Für die Begleitung des Projekts mit thematischer Expertise und für die wissenschaftliche Führung gilt mein Dank meiner fachlichen Betreuerin Susanne Schröder und meinem Doktorvater Heinz-Wilhelm Hübers, die insbesondere auf der Zielgeraden viel Zeit investierten, um mich dabei zu unterstützen dieses Projekt zum Abschluss zu führen. Von ebenfalls unschätzbarem Wert waren die vielen Diskussionen mit den früheren Doktoranden David Vogt und Kristin Rammelkamp sowie meinem fast zeitgleich promovierenden Kollegen Peder Hansen, die mich anfangs in die LIBS-Thematik eingeführt und bis zuletzt mit den richtigen Fragen zu einer schlüssigen Interpretation meiner Daten gebracht haben. Von ihren jeweiligen Stärken habe ich gelernt meine Erkenntnisse klar darzulegen und zu formulieren, meine Daten und Ergebnisse optimistischer zu betrachten und mir für jeden Auswerteschritt ein Skript anzulegen – „Vielleicht braucht man es ja nochmal." Einen ebenfalls wichtigen Beitrag zur Umsetzung des Projekts haben Sven Frohmann, Enrico Dietz und Michael Greiner-Bär mit ihrer Erfahrung in den Bereichen Vakuumtechnik und technische Konstruktion geleistet. Darüber hinaus möchte ich mich auch bei den anderen Kollegen der Abteilung und des Instituts für zahlreiche inspirierende und ablenkende Mittagspausen, Kaffeepausen, Skat- und Doppelkopfabende und Weihnachtsmarktbesuche bedanken. Ich hatte eine schöne Zeit am DLR in Berlin-Adlershof.

Für den nötigen Ausgleich zum Promotionsstress bin ich meiner Familie für einen immer vorhandenen sicheren Hafen sowie meinen Freunden, die mich auf die Promotionsstelle hingewiesen, mich während des gesamten Projekts unterstützt und auch meine teils unerträgliche Natur im Endspurt geduldet haben, zu Dank verpflichtet. Danke für die vielen Radtouren, Wanderungen, Ausflüge, Reisen, Barbesuche und die gemeinsamen Abende zu Hause. Besonders im letzten Jahr hat auch der Akademische Segler-Verein mir sehr geholfen mich hin und wieder zu entspannen. Mit dem Betreten des Vereinsgeländes sind alle Sorgen und aller Stress für kurze Zeit vergessen und so sind auch körperlich anstrengende Arbeiten am Schiffspark für Kopf und Geist wie ein Urlaub am (auf dem) Meer.

Zuletzt möchte ich mich bei Virginia bedanken. Sie begleitet mich nun seit fast einem Jahr, hat mir wohlwollend viele Aufgaben des täglichen Lebens abgenommen und mir so die notwendige Zeit gegeben dieses Buch zu schreiben. Trotz der aktuellen Einschränkungen und des mit der Arbeit verbundenen Stresses war es ein schönes Jahr und ich hoffe, dass es noch viele weitere Jahre geben wird.

Berlin, im November 2020

Selbständigkeitserklärung

Ich erkläre, dass ich die Dissertation selbständig und nur unter Verwendung der von mir gemäß § 7 Abs. 3 der Promotionsordnung der Mathematisch-Naturwissenschaftlichen Fakultät, veröffentlicht im Amtlichen Mitteilungsblatt der Humboldt-Universität zu Berlin Nr. 42/2018 am 11.07.2018 angegebenen Hilfsmittel angefertigt habe.

Berlin, 6. November, 2020

Simon Kubitza